UVA-induced metabolic changes in non-malignant skin cells and *ex vivo* cultured murine skin

DISSERTATION ZUR ERLANGUNG DES
DOKTORGRADES DER NATURWISSENSCHAFTEN (DR. RER. NAT.)
DER FAKULTÄT FÜR BIOLOGIE UND VORKLINISCHE MEDIZIN
DER UNIVERSITÄT REGENSBURG

vorgelegt von
Irina Emilova Ivanova

aus
Sofia, Bulgarien

im Jahr
2021

Das Promotionsgesuch wurde eingereicht am:
17/11/2021

Die Arbeit wurde angeleitet von:
Prof. Marina Kreutz

Unterschrift:

(Irina Ivanova)

Table of content

List of Abbreviations I

1D	One-dimensional
2D	Two-dimensional
2d	Two days
4d	Four days
8-OHdG	8-hydroxydeoxyguanosine
AO/PI	Acridine orange/Propidium iodide
ATP	Adenosine triphosphate
BCC	Basal cell carcinoma
CPMG	Carr-Purcell-Meiboom-Gill pulse sequence
DCFDA	2′, 7′-Dichlorofluorescin diacetate
DMEM	Dulbecco's Modified Eagle Medium
DMSO	Dimethyl sulfoxide
ECM	Extracellular matrix
exp1, exp2	Experiment 1, experiment 2 (referring to murine skin experiments)
FCS	Fetal calf serum
FID	Free induction decay
GSH	Glutathione
GSSG	Glutathione disulfide (oxidized GSH)
HEKa	Human epidermal keratinocytes adult
HEMa	Human epidermal melanocytes adult
HSQC	Heteronuclear single quantum coherence
Hz	Hertz
IR	Infrared radiation
KEGG	Kyoto Encyclopedia of Genes and Genomes
LC	Labelling coefficient
mg	milligram
mKera	Mouse keratinocytes
ml	Millilitre
µl	Microliter
MMP	Matrix metalloproteinase
mRNA	Messenger RNA

List of Abbreviations II

MT	Membrane type
NADH	Nicotinamide adenine dinucleotide (reduced)
NADPH	Nicotinamide adenine dinucleotide phosphate (reduced)
NBTC	Nitroblue tetrazolium chloride
NMR	Nuclear magnetic resonance
PEP	Phosphoenolpyruvate
PLP	Phospholipid peroxidation
ppm	Parts per million
PV	Peak volume
pyr	Pyruvate
rf	Radio frequency
RNA	Ribonucleic acid
ROS	Reactive oxygen species
SCC	Squamous cell carcinoma
SR	Solar radiation
ST	Supplementary table
TIMP1	Tissue inhibitor of metalloproteinase 1
TSP	Trimethylsilylpropanoic acid
UV	Ultraviolet
UVR	Ultraviolet radiation
VR	Visible radiation
xCT	cystine/glutamate antiporter xCT

1. Introduction

1.1. The skin – the largest organ in the human body

The skin is the largest organ in the human body, representing 16 % of the total body weight. It is a complex structure with a diverse array of functions. The skin is the main barrier between the body and the outside world and protects it from environmental influences such as friction, bacterial infections, and UV-radiation. It also plays a role as an osmotic barrier, providing protection from water loss. Furthermore, the skin serves as a major sensory organ with receptors for touch, heat, and pain. It also participates in the synthesis of vitamin D. Another important function of the skin is temperature regulation through regulation of the blood flow, sweat production, and secretion (1-3). As a structure, the skin can be divided in three main layers: epidermis, dermis, and hypodermis (4, 5) as shown in Fig. 1. Each of these layers has not only a specific function but also highly specialized subsets of cells.

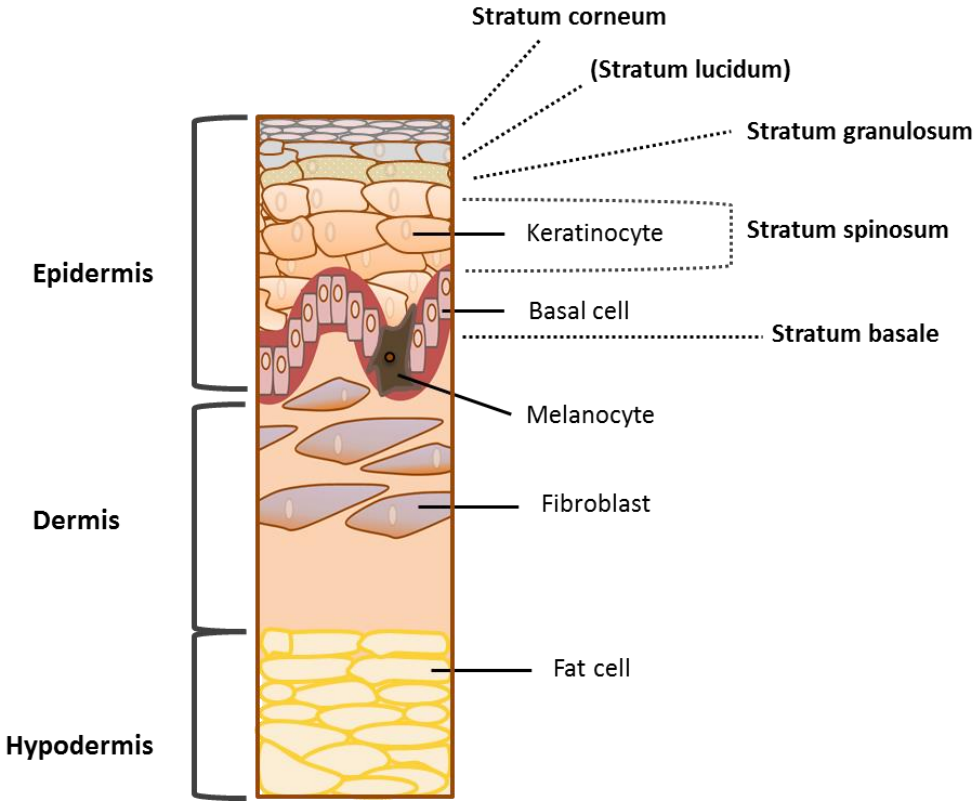

Fig. 1: The three layers of the skin – epidermis, dermis, and hypodermis– with the most prominent skin cells for each layer. The stratum lucidum is present only in areas with a very thick skin such as soles and palms (2, 4-6).

1.1.1. The Epidermis – keratinocytes on the rise

The uppermost layer, the epidermis, is mainly populated by keratinocytes. It is derived from the ectoderm during embryonal development. In addition to the keratinocytes epidermal dendritic cells (Langerhans cells) are also present in this skin layer. From top to bottom the epidermis is composed of the sub-layers stratum corneum, stratum lucidum, stratum granulosum, stratum spinosum, and stratum basale, albeit stratum lucidum being present only in areas with a very thick skin such as soles and palms (2, 3, 6).

The first two sub-layers (stratum corneum and stratum lucidum) consist of multiple layers of flattened dead keratinocytes. These cells are terminally differentiated and keratinized, without a nucleus or organelles. The cells of the stratum corneum are embedded in a lipid matrix, produced by keratinocytes inhabiting the lower sub-layer – stratum granulosum. This cell-lipid layer presents the main protection from friction, chemical absorption, and water loss (3, 6).

The stratum granulosum, build by three to five layers of mature keratinocytes, is the precursor of the two upper-most sub-layers. The cells in the stratum granulosum possess keratohyalin granules containing keratin precursors that are needed for the formation of the interfibrillar matrix. These keratinocytes also secrete lipids that are required for sustaining the epidermal water barrier (3, 4). During their maturation and differentiation process, known as keratinization, their cytoplasmic content increases, including the amount of tonofilaments, keratohyalin granules, and lamellar granules. As the keratinization progresses, the tonofilaments intercalate with the keratohyalin to form a meshwork. Slowly the nuclei and the rest of the organelles disintegrate. The content of the lamellar granules is released, coating the cells. The final stage of this transformation results in the development of the stratum lucidum and corneum, the main function of which is to protect the skin from water loss (3, 7).

The fourth sub-layer from top to bottom is the stratum spinosum. Similar to the stratum granulosum it consists of living keratinocytes. The cells in the stratum spinosum are tightly packed and connected by desmosomes and tonofibrils. This complex three-dimensional structure ensures the mechanical stability of the epidermis (3, 8).

The stratum basale consists of a single layer of cells. These cells are connected to the basal membrane via hemidesmosomes, while desmosomes are responsible for the cell-cell connections. The cells in the stratum basale undergo mitosis and the resulting 'daughter cells' migrate upwards to the stratum spinosum, constantly replenishing the epidermis (3).

As in all previous epidermis sub-layers, the main cell population in the basal layer are keratinocytes. However, there is also another important cell group residing there – the melanocytes. Mature melanocytes are small, dendrite sprouting cells, stemming from the neuronal crest. They possess specialized membrane-bound organelles, melanosomes, which are responsible for melanin production and containment. The ratio between melanocytes and keratinocytes in the stratum basale is usually 1:10. Together the two cell types form the so-called "epidermal melanin units" and thus taking a joined role in the synthesis, transfer, transport, and degradation of the melanosomes. Produced by the melanocytes, the pigment-containing melanosomes are transported via the dendritic protrusions to the keratinocytes, where they accumulate above the cell's nucleus, facilitating its photoprotection against ultraviolet radiation by acting as an endogenous sunscreen (3, 7, 9-11).

Below the stratum basale lays the basement membrane. It is a complex sheet-like structure build by laminin and type IV collagen networks. The basement membrane is the junction between the epidermis and the underlying dermis. It plays important role in regulating the exchange of growth factors and nutrients between the dermis and epidermis, influencing cell proliferation, differentiation, and wound healing (3, 12).

1.1.2. The Dermis – fibroblasts at their finest

The second main skin layer is the dermis. It is responsible for the mechanical properties of the skin. Stemming from the mesodermal layer during embryonal development, its thickness varies in the different regions of the body. The dermis is composed of fibroblasts, embedded in a densely packed network of collagen, reticular and elastic fibres. This elastic matrix provides physical support for nerves and blood vessels. In addition to fibroblasts, macrophages fulfil the important role of immune-surveillance in this skin layer. The substantial network of capillaries that spans throughout the dermis results in the skin being one of the most highly perfused organs in the body, resulting in not only enhanced nutrient and antioxidant transport, but also

allowing for easy access of the immune cells. Additionally, sweat and sebaceous glands, hair follicles and muscles are anchored in the dermis, making it a very complex tissue with diverse functions (3).

As mentioned, the major type of cells, populating the dermis, are fibroblasts. Their main function is to produce and secrete proteins and polysaccharides to the extracellular space to form the extra-cellular matrix (ECM)(13). In general, ECM is responsible not only for the physical properties of connective tissue but also plays an important role in tissue morphogenesis, differentiation and homeostasis by participating in crucial signalling cascades (14). In addition to their involvement in the ECM formation, fibroblasts also participate in wound healing and modulation of immune and inflammatory responses. Especially the cross-talk between the immune system and the fibroblasts is essential for the maintenance of tissue homeostasis (13).

Understanding the crucial role that fibroblasts play in ECM-formation has been an important issue in dermatological research. It is currently well documented that fibroblasts produce and secrete two distinct groups of structural proteins – collagens and elastin. The collagen family can be divided into three big sub-populations: fibrillary, fibril-associated, and network-forming collagens. In the skin, the most prominently secreted collagens are the fibrillary collagens I and III. However, the influence of fibroblasts on the ECM is not limited to protein synthesis. They can also re-model matrices through organizing, shaping, or degrading structural proteins. For example, they can exert mechanical force and re-arrange collagen into fibres or flat sheets depending on the tissue properties and requirements. Another way to modulate the ECM is by secreting matrix-digesting enzymes called matrix metalloproteinases (MMPs) (13). MMPs form a large family of structure-remodeling proteins from which several have been extensively studied in connection to cancer development and progression and skin photoaging. MMPs are subdivided into five categories: collagenases, gelatinases, stromelysins, matrilysins and membrane-type (MT) MMPs (15). From them, the collagenases MMP1 and MMP13, the gelatinases MMP2 and MMP9, the stromelysin MMP3 and the MT-MMP15 are of particular interest in this study. All of them, except MMP13 and MMP15, have been shown to play a role in both photocarcinogenesis and photoaging. MMP1 is specialized in collagen type I and III degradation, promotes tumor growth in basal cell carcinoma (BCC) and squamous cell carcinoma (SCC), and aids invasion in melanoma (15). MMP13 facilitates the

metastatic phase in melanoma, BCC, and SCC and plays a role in neo-angiogenesis. MMP2 and MMP9 degrade collagen IV and similarly to MMP13 support growth, invasion, and neovascularization in skin cancer. MMP3 is not only capable of degrading collagen I but also activates other MMPs such as MMP1 and MMP9. Last but not least, MMP15 also aids the melanoma invasion (15).

It is evident that dysregulation and degradation of the collagen matrix can lead to disturbance of skin morphology and cancer progression. However, collagen is not singularly responsible for matrix properties and stability. The elastic fibres, secreted by the fibroblasts, provide flexibility and resiliency to the skin. These fibres consist of tropoelastin, associated with microfibrillar proteins such as fibrillins, microfibril-associated glycoprotein, and associated microfibril protein (13, 16). Particularly fibrillin is a major component of the elastic fibres and contributes to the elastic deformation capability of the tissue. In the presence of UV-radiation, the fibrillin-content of the skin is reduced, leading to increased wrinkling (17, 18).

In addition to these structural proteins, fibroblasts also produce and secrete glycosamino- and proteoglycans. These secreted components attract water and ions, resulting in the formation of a hydrated gel. Besides that, some proteoglycans bind to cytokines and growth factors, thus influencing cell proliferation and immune response (13).

The last type of fibres, synthesized by the fibroblasts, are the reticular fibres. In contrast to collagen fibres (composed of collagen type I), they consist of collagen III in association with collagen type V, glycoproteins, and glycosaminoglycans. They build a delicate network of thin fibrils, firmly attached to the basal lamina (16).

Besides the matrix-related structural proteins, fibroblasts also secrete adhesion molecules such as fibronectin. It has been shown that the production and deposition of fibronectin in the ECM influence skin cell migration, which is an important factor during wound healing and carcinogenesis (19).

1.1.3. The Hypodermis

The hypodermis lies under the dermis and builds the third and last skin layer. Albeit fibroblasts still being present, the most prominent cell type in this layer is the

adipocytes (fat cells). The function of the hypodermis is to connect the skin with the underlying muscle and bone, provide thermoregulation, insulation, and cushioning(20).

1.2. The Sun and its light – the good, the bad, and the ugly

The Sun –the closest star to our planet. Its constant thermonuclear reactions are a source of life, heat, and imminent danger to every living being on Earth. Where does this danger come from? Is it due to the frequent solar flares that bombard the planet's atmosphere with harmful electromagnetic and corpuscular radiation? The answer is much simpler and often overlooked. The sunlight that gives us warmth and catalyses many biochemical reactions crucial to animal and plant survival is also potentially dangerous to our health (21-23).

The Sun's optical radiation, solar radiation (SR), or simply sunlight, can be subdivided in the following spectra: ultraviolet radiation (UVR) with a wavelength from 100 nm to 400 nm, visible radiation (VR) with a wavelength from 400 nm to 780 nm and infrared radiation over 780 nm. In particular, UVR can be further differentiated in UVC (100-280 nm), UVB (280-315 nm), and UVA (315-400 nm). Additionally, UVA can be differentiated into short wave UVA2 (315–340 nm) and longwave UVA1 (340–400 nm), with UVA1 making up 75 % of the total UVA irradiation relevant for human health (23). It must be noted that the solar spectrum reaching the planet's surface is different than the one originally emitted by the sun. Thanks to the Earth's atmosphere, and especially the ozone layer, the sunlight is filtered considerably. Only irradiation over 290 nm can freely penetrate this protective barrier, which means that UVC and parts of UVB radiation get blocked by the ozone layer. With this, the majority of the surface solar radiation consists of VR and IR (95 %) and the rest is UVR. Even in the small portion of UVR, UVA has the biggest prevalence, being 95 % of the total surface UV spectrum. Still, the UVR reaching the earth is actually the main cause of health issues in humans (22, 23). Besides the short-term damage in the form of erythema and sunburn, there are also long-lasting biochemical and structural consequences of sun exposure.

1.2.1. The benefits of sunlight

There are two major ways of interaction between solar radiation and living organisms – thermal and photochemical, with the latter being most prevalent in UVR.

It should be acknowledged that SR yields benefits to the organisms living on Earth. It plays crucial role in generating plant biomass via photosynthesis (24) and in vitamin D synthesis in animals (25). Furthermore, it provides warmth in the form of IR and last, but not least, it gives us light. It has even been suggested that the emergence and evolution of life on our planet would have been impossible without the solar energy (26). Despite all that, the adverse effects of UVR on human health cannot be neglected.

1.2.2. Ultraviolet radiation and its implications cellular and tissue damage

Since the major component of surface UVR consist of UVA, this makes it also one of the major contributors to cellular damage. Furthermore, compared to UVB, UVA has a higher penetration depth, reaching up to the dermis, resulting in a higher amount of damage (27). Unlike UVB, UVA is not blocked by the most types of window glass, resulting in higher daily exposure to this type of radiation in particular (28, 29). As shown in Fig. 2, UVA has a plethora of effects in the cell. It can damage DNA directly by inducing cyclobutane pyrimidine dimers (CPDs), especially in thymine-thymine dipyrimidine sites (30-32). DNA can be also indirectly damaged via UVA-induced reactive oxygen species (ROS), such as singlet oxygen, hydrogen peroxide (H_2O_2), hydroxyl radical (●OH), and superoxide anion ($O_2^{\bullet -}$) (33, 34). Amongst them, hydrogen peroxide can be transported across cellular membranes (35). The presence of radicals in the cell can lead to modifications of guanine, resulting in the formation of 8-hydroxydeoxyguanosine (8-OHdG). This can cause G to T transversions, leading to miscoding DNA lesions (34). Furthermore, despite the energy of UVA photons being too weak to cause direct DNA-breaks, it has been shown that UVA-induced ROS mediate double-strand breaks (36). Interaction between ROS and cellular components can additionally lead to protein oxidation (37) and phospholipid peroxidation (38, 39). This may lead to protein degradation or dysfunctional proteins, as well as changes in the structure, assembly and dynamics of lipid membranes, resulting in dysfunctional cells or apoptosis (40).

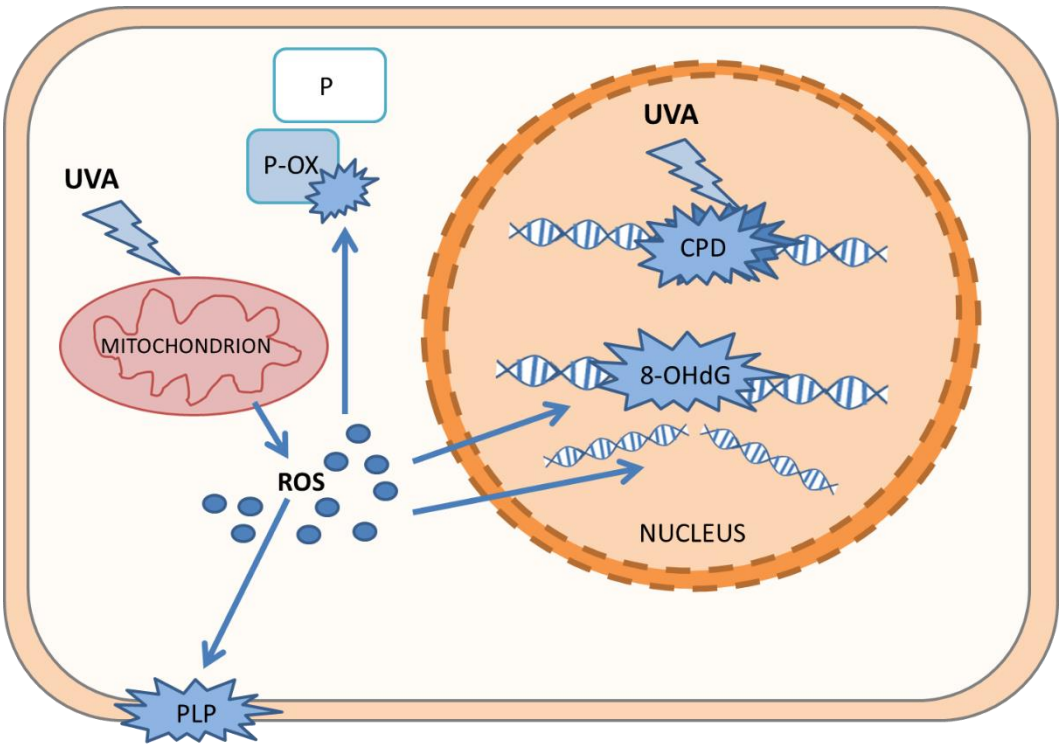

Fig. 2: UVA-induced cellular damage in a mammalian cell. Direct DNA-damage is caused by the formation of CPDs, indirect damage – via 8-OHdG and ROS-mediated double-strand breaks. UVA-generated ROS further lead to the oxidation of proteins (P), as well as phospholipid peroxidation (PLP).

The abovementioned molecular changes have a large-scale influence on the skin structure and integrity (see Fig. 3). Prolonged UVR exposure can result in decreased fibronectin expression and fragmentation of interstitial collagen, accompanied by reduction of fibroblast contractile activity. The least-concerning effect of this matrix weakening and degradation is the so-called solar elastosis, resulting in skin thickening and wrinkle formation (41-44). Supporting this, it has been shown in hairless mice that UVA irradiation decreases the total collagen content in the skin, while the ratio of collagen type III to total collagen increases, accompanied by fibronectin increase (45). More severe consequences result in UVA-mediated DNA damage. It can result at best in enhanced cell death, at worst – in cancer initiation. Mismatches due to base modifications (such as but not limited to 8-OHdG) can lead to fixed genomic mutations, often referred to as UVA-fingerprint mutation. Cases of such genomic UVA-fingerprints have been shown in SCC carcinoma, especially in *p53.* What is more, these mutations have been detected in deeper layers of the skin, which further emphasise the higher penetration capability of UVA compared to UVB (46, 47).

As mentioned above in the case of tumor suppressor *p53*, there has been a direct correlation between sun exposure and cancer-initiating mutations. As for UVA, its role as a skin-cancer-inducing mutagen has achieved more prominence in recent years (48-52).

Besides tumor initiation, UVA also influences tumor progression and migration. As already mentioned, it influences the composition and elasticity of ECM. Major players in this remodelling are the MMPs. The expression of MMPs increases when the cells are irradiated with UVR. This results in increased cell motility and metastasis by removing the physical barriers to invasion and modulating cell adhesion (15, 53, 54).

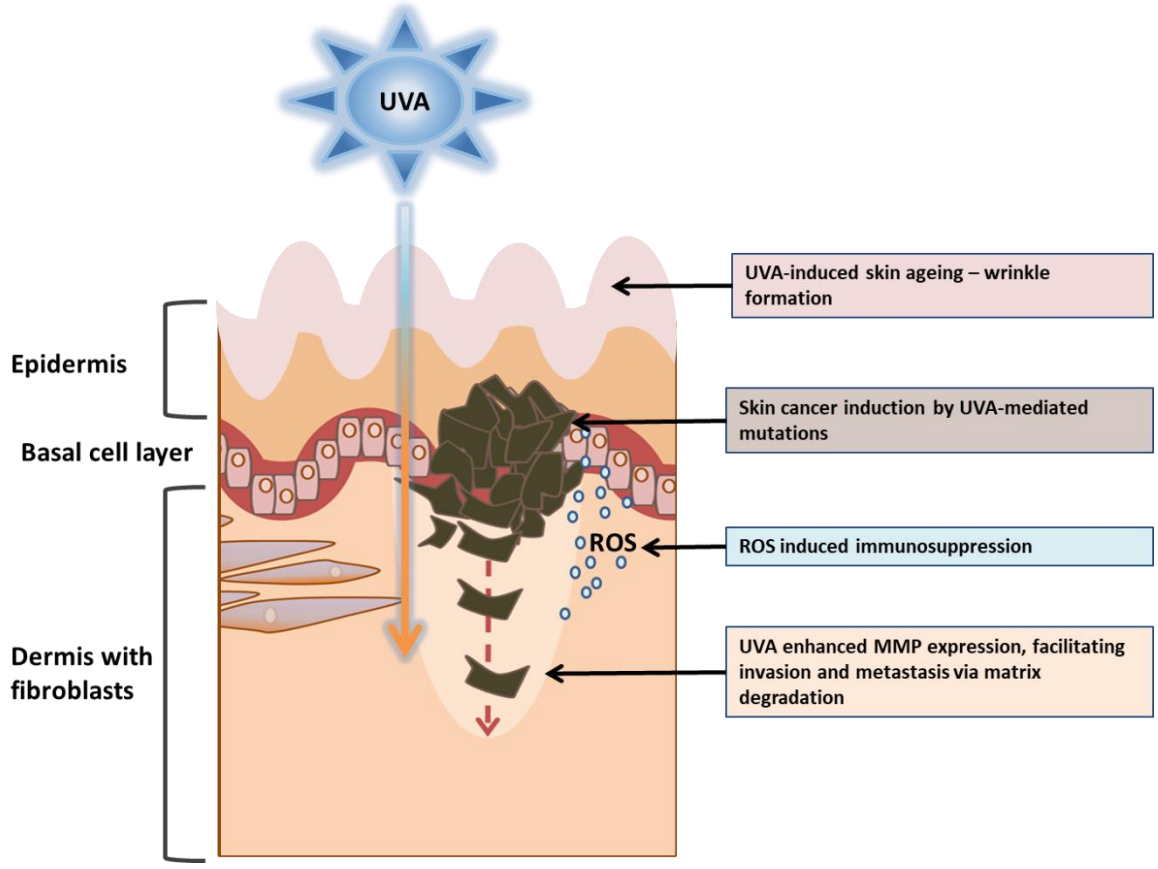

Fig. 3: Adverse effects of UVA on skin structure and integrity – wrinkle formation, tumor initiation, immunosuppression, and tumor invasion in surrounding tissue (55).

Even before the carcinogenic effects occur, UVR has the ability to suppress immune cell responses (56). In general, it is considered that DNA damage, isomerisation of urocanic acid, and cell membrane changes are primarily responsible for the UVR-mediated immunosuppression. They influence the number of Langerhans

cells in the skin, modulate the cytokine expression and affect the T cell populations infiltrating the skin. In turn, this results in both local and systemic immunosuppression (57). In the case of UVA, it has been reported that it attenuates the antigen-presenting capability of dermal fibroblasts in a dose-dependent manner even at doses as low as 5 J/cm^2. This effect seems to be at least to some extent ROS-mediated (58).

As shown above, UVA irradiation and the resulting ROS production have a plethora of effects on a variety of skin cells and cellular structures. They can modify healthy skin cells, leading to malignancies. However, the adverse effects of UVA do not end with tumor initiation, immune suppression, and ECM remodelling. It has been reported that UVA can also influence metabolic processes in tumor cells (53).

1.2.3. UVA induces and enhances metabolic changes in skin and skin cancer

Ever since the beginning of the 20th century, cellular metabolism has been under extensive investigation. As discussed above, UV-radiation is an environmental risk factor that promotes the generation of reactive oxygen species and can harm the cells and tissues on a structural level by disrupting cell membranes (59) and degrading the extracellular matrix (15, 60). In addition to that, studies have shown that UV-radiation is also responsible for a variety of metabolic changes occurring in the skin cells.

The most well-known metabolic change caused by UV-light is the induction of melanin production in melanocytes (61, 62). Unlike UVB, which causes delayed skin pigmentation via transcriptional activation of melanin-producing enzymes, UVA-irradiation results in immediate pigment darkening (63, 64). This UVA-promoted pigmentation is facilitated by Ca^{2+} and retinal signalling and results in melanin synthesis 1-4h after irradiation (62). The speed of this reaction reflects the need for rapid mitigation of UV-damage to the skin, in which melanin plays a crucial role by acting as a natural sunscreen and absorbing 50-75% of UVR (11).

Melanocytes are not the only cell type to react to irradiation. UV-induced metabolic changes have been observed also in keratinocytes. Keratinocytes are the skin cells that most exposed to UVR, being the major component of the first vital skin layer – the epidermis. UVR exposure results in disruption of the lipid balance in these cells, especially influencing the metabolism of phospholipids and ceramides (65).

Another important UV-mediated metabolic change can be observed in the biosynthesis of dehydroretinol. Retinol (also known as Vitamin A1) and its metabolites play a crucial role in epithelial differentiation, cell proliferation, or cell cycle arrest (66). A desaturation product of retinol at C3-4, dehydroretinol (Vitamin A2) has been observed to play a role in protecting the retina of some gecko species from UV radiation (67). In humans, dehydroretinol is produced by keratinocytes and are abundantly present in the upper layers of the epidermis (2- and 9-fold higher in the stratum granulosum and stratum corneum, respectively, than the amounts in the basal cell layer) (68, 69). The correlation between UVR and retinol production has been established by the work of Tafrova et al., who managed to show that irradiation with both UVA and UVB promote dehydroretinol biosynthesis. Furthermore, they also showed that this metabolite successfully reduces UVA/B-induced apoptosis (69). This, together with the proposed role of dehydroretinol as potential anti-cancer metabolite (70), supports its role in UV-induced skin cancer protection.

Even fibroblasts in the deeper layers of the dermis are not spared the influences of UV-radiation. Both UVA and UVB can modulate phospholipid metabolism in these cells (71).

In addition to influencing the metabolism of healthy skin cells, UVR has also further negative effects on skin malignancies. Tumor cells have long been known to be metabolically dysregulated, switching their glucose metabolism from oxidative phosphorylation to glycolysis with enhanced lactic acid production even in the presence of oxygen (also known as Warburg Effect) (72). In this process, most of the glucose taken in by the cell is not utilised in the Krebs cycle and oxidative phosphorylation for the production of energy (in form of ATP). Instead, the intermediary product of glycolysis, pyruvate, is metabolized to lactate. Although still yielding ATP to the cell, this process of obtaining energy is inefficient compared to mitochondrial respiration, resulting in less ATP per molecule glucose (2 mol ATP from glycolysis, compared to 30-34 mol from oxidative phosphorylation) (73-75). Still, this metabolic deviation from the standard energy production has its benefits for the tumor cells. First, the large amounts of glucose consumed are used as a carbon source to facilitate proliferation-associated anabolic processes like DNA, protein, and lipid synthesis. In addition, the aerobic fermentation of glucose is 10-100 times faster than its complete oxidation in the mitochondria, resulting in similar energy levels to normal respiration,

albeit at the cost of increased glucose consumption (76, 77). Another positive result of the Warburg effect is the production of lactate. Due to the acidic environment it generates, lactic acid has been known to have a strong influence on tumor microenvironment. It increases hyaluronan production in fibroblasts, followed by elevated expression of CD44, resulting in an environment that promotes growth and motility of cancer cells (76, 77). Increased lactate concentrations in the tumor stroma can also lead to attenuation of immune responses (76, 78, 79).

In addition to the already present Warburg effect in tumors, UVA has been shown to increase its prevalence in irradiated cancer cells (53). *Kamenisch et al.* report that UVA-irradiation of melanoma cells can lead to increased glucose consumption and lactate production. Furthermore, key MMPs such as MMP2 and MMP 9 were upregulated in both UVA irradiated and lactic acid-treated samples, supporting the connection between the UVA-induced metabolic changes and tumor migration. These metabolic changes were also, at least partially, due to ROS production.

There have been indications of UVA-mediated metabolic changes in normal skin cells, showing up-regulation of glucose metabolism-related genes in keratinocytes (80) but the research in this field is still incomplete and warrants further investigations.

1.2.4. Cellular anti-oxidative strategies against UVA-generated ROS

Since UVA is capable of generating ROS which are harmful to a variety of cellular structures, it is logical to assume that the cells have developed means to counter and detoxify such toxic compounds (53). Such endogenous antioxidants are of great interest both in the field of clinical applications and cosmetics. Using substances that the body itself can synthesize in topical or oral formulations can increase product safety and patient tolerability. Especially in the field of skin care, substances that can reduce the adverse effects of sun exposure are of high demand.

Indeed, several metabolic products, including the ones derived from the aerobic fermentation of glucose, have been reported to fulfil the role of endogenous antioxidants.

One of the most well-studied and described cellular antioxidants is glutathione (GSH), due to it being ubiquitous throughout the body. The enzyme glutathione peroxidase detoxifies lipid peroxides into alcohols with GSH as a cofactor. The oxidized

form of GSH, glutathione disulphide (GSSG), can be “regenerated” back to its original form by the enzyme glutathione reductase and by NADPH. This makes GSH readily available in large quantities when ROS detoxification is needed (81).

Lactate, the main product of aerobic glycolysis, albeit not as well studied as GSH, has also shown antioxidant potential. Groussard et al. have shown that adding lactate to hepatocyte culture leads to a decrease of superoxide anion and hydroxyl radical levels in a dose-dependent manner (82). It has also been shown that sodium lactate can serve as an antioxidant and food preservative (83) and has been officially allowed as such by the European Union under the number E325 (84).

In addition to lactate, the intermediary product of glycolysis, pyruvate, has also been considered a potent antioxidant (85). In the presence of ROS, pyruvate can be non-enzymatically decarboxylated to acetate exerting its protective function in the cells (86-88). A more recent study has shown that pyruvate successfully scavenges hydrogen peroxide from the cell culture medium and exerts protective functions in oxidant-treated fibroblasts and embryonic stem cells (89). The connection between pyruvate’s scavenger properties and UVR-induced ROS has been established by Gupta et al. with emphasis on UVB (90). This study shows that oral and topical application of pyruvate significantly reduced and delays UVB-induced erythema in guinea pigs and deems it suitable as a novel sunscreen agent.

Although both lactate and pyruvate seem to have antioxidant properties, there have been studies raising concerns about the ability of both compounds to induce ROS. Bassenge et al. have shown that increased lactate levels in guinea pig hearts lead to increased ROS levels (91). Tauffenberger and associates also show linear correlation between increasing ROS levels and increasing lactate concentrations but also detects increased ROS production in pyruvate treated samples (92). However, considering that lactate helps skin tumors to escape immune-surveillance (78), using lactate as an antioxidant for clinical and cosmetic applications seems to be the less viable option compared to pyruvate. In addition to that, there are studies showing that lactate can promote the expression of MMPs (93, 94), which could further increase the effects of photo aging. Therefore, it was decided that the investigation of the potential antioxidant properties of pyruvate is of greater interest for possible clinical applications. Elaborating on the influences that high pyruvate levels have on cell metabolism would be helpful in order to determine pyruvate’s potential implementation as an antioxidant

in topical skin care. There have been studies showing that topical application of pyruvate in guinea pigs can reduce UVB-induced erythema (90), thus indicating the applicability of pyruvate in UV-protection. Therefore, it is important to study in more detail how exactly pyruvate would interact with UVA in regard to influencing human cells and skin.

1.3. Aim of the thesis

As shown above, UVR plays an important role in our everyday lives. It modifies cellular metabolism and can have adverse health effects, ranging from photoaging to cancer development. A better understanding of the metabolic changes, occurring in the cells and tissues is the first step in providing adequate prevention and treatment of UVR-induced damage.

This work concentrates on the metabolic changes occurring in non-malignant skin cells – keratinocytes, melanocytes, and fibroblasts, with emphasise on UVA. UVA is the most abundant type of UVR on the Earth's surface and is also the one penetrating deepest into the skin. The aim of this thesis is to answer the question what are the influences of UVA on the metabolism of non-malignant cells of human and murine origin. It will also investigate the role of pyruvate as an antioxidant during UV-irradiation and elaborate on its functions in modulating the metabolism of cells and skin explants, as well as its role on the expression of MMPs.

2. Materials and methods

2.1. Materials

Table 1 a: Chemicals and Reagents

Chemical/Reagent	Distributor	Product number	Used for
Primer Random $p(dN)_6$	Roche	11034731001	Reverse transcription of cDNA
Nuclease P-1 from Penicillium citrinum	Sigma-Aldrich	N8630	8-OHdG Elisa
D-(+)-Glucose solution, 100 g/L in H_2O	Sigma-Aldrich	G8644	Medium preparation for cell culture
2-Deoxy-D-glucose	Sigma-Aldrich	D8375	Glycolysis inhibition
Oxythiamine chloride hydrochloride	Sigma-Aldrich	O4000	Pentose phosphate pathway inhibition
2′,7′-Dichlorofluorescin diacetate	Sigma-Aldrich	D6883	ROS detection
α-Nicotinamide adenine dinucleotide (NADH)	Sigma-Aldrich	N6879	NBTC vitality test
Nitrotetrazolium Blue chloride (NBTC)	Sigma-Aldrich	N6876	NBTC vitality test
Ringer solution	B.Braun Melsungen AG	9517170	NBTC vitality test
Penicillin-Streptomycin	Sigma-Aldrich	P0781	Cell culture
L-Glutamine	Sigma-Aldrich	G7513	Cell culture
Trypsin-EDTA solution	Sigma-Aldrich	T4174	Cell culture
dNTP	New England BioLabs	N0446S	Reverse transcription
Sodium Pyruvate 100 mM	Thermo Fisher	11360070	ROS quencher in cell culture experiments
DPBS, no calcium, no magnesium	Thermo Fisher	14190094	Cell culture

Table 1 b: Chemicals and Reagents

Chemical/Reagent	Distributor	Product number	Used for
Lactate Standard 40 mg/dl	Trinity Biotech	826-10	Colorimetric lactate detection in cell supernatant (product discontinued)
Ethanol absolute for analysis	Labochem international	LC-4045.1	DNA/RNA extraction
Sulfuric acid	Merck	112080	Colorimetric glucose detection
Zinc chloride	Roth	3533.1	8-OHdG detection
Sodium chloride	Roth	3957	8-OHdG detection
Sodium acetate anhydrous	Merck	106236	8-OHdG detection
Trizma base	Sigma-Aldrich	T1503-500G	8-OHdG detection
Magnesium chloride	Roth	2186	8-OHdG detection
Sodium pyruvate-13C3, 99 atom % 13C	Sigma Aldrich	490717	Pyruvate labelling experiments
GLUCOSE-D U-13C6 99%13C	Eurisotop	CLM-1396-1	Glucose labelling experiments
Amphotericin B from Streptomyces	Sigma Aldrich	A2942	Mouse skin *ex vivo* cultivation
Trypsin 10x concentrated	Sigma Aldrich		Cell culture (cell detachment)
Tissue-Tek	Sacura	4583	Embedding of tissue for cryotome cutting
Braunol	B.Braun Melsungen AG	3864154	Isolation of mouse keratinocytes
Aquatex mounting agent	Merck	108562	Mounting of tissue sections
Ciprofloxacin	Fresenius Kabi	PZN: 3506088	Cell culture, isolation of fibroblasts from patient samples

Table 1 c: Chemicals and Reagents

Chemical/Reagent	Distributor	Product number	Used for
Formic acid 98 %-100 %	Merck	533002	NMR, metabolite quantification in 1D CPMG
Deuterium oxide	Sigma-Aldrich	293040	NMR, metabolite quantification of filtered samples in 1D CPMG and 2D HSQC
di-Potassium hydrogen phosphate trihydrate	Merck	105099	NMR buffer
Potassium dihydrogen phosphate	Merck	104873	NMR buffer
2-Mercaptoethanol	Sigma Aldrich	M3148	RNA extraction

Table 2: Assay Kits

Kit	*Distributor*	*Product number*	*Used for*
Glucose (GO) Assay Kit	Sigma-Aldrich/Merck	GAGO20	Colorimetric glucose detection in cell supernatant
Lactate kit reagent	Trinity Biotech	735-10	Colorimetric lactate detection in cell supernatant (product discontinued)
Lactate Assay Kit	Sigma-Aldrich/Merck	MAK064	Colorimetric lactate detection in cell supernatant
OxiSelect™ Oxidative DNA Damage ELISA Kit	Cell Biolabs, Inc.	STA-320	8-OHdG Quantitation
QIAmp DNA Mini Kit	QIAGEN	51306	DNA extraction from cells and tissues
NucleoSpin RNA	Macherey-Nagel	740955.250	RNA Extraction from cells
FastStart Essential DNA Green Master	Roche	06924204001	qPCR analysis
SuperScriptII Reverse transcriptase	Invitrogen/Thermo Fisher	18064-014	Reverse transcription of cDNA
EnzyChrom™ Pyruvate Assay Kit	BioAssay Systems	EPYR-100	Pyruvate detection in cell supernatant
AO/PI Cell Viability Kit for Luna FL	Biozym/BioCat	87045/F23001-LG	Cell counting, Cell viability determination

Table 3 a: Other consumables

Consumable	*Distributor*	*Product number*	*Used for*
Cellstar 50 ml tubes	Greiner Bio-One	227261	Cell culture
Cellstar 15 ml tubes	Greiner Bio-One	188271	Cell culture
Corning® 500 mL Vacuum Filter/Storage Bottle System	Corning	431097	Filtering of cell culture medium
Serologic Pipet 10 ml	SARSTEDT	86.1254.001	Cell culture
Serologic Pipet 5 ml	Greiner Bio-One	606180	Cell culture
Serologic Pipet 25 ml	Greiner Bio-One	760180	Cell culture
Cell Counting Slides for Luna, 1000 Counts	Biozym/BioCat	872011/L12004-LG	Cell counting
Costar® 6-well Clear TC-treated Multiple Well Plates	Corning	3516	
20 cm petri dish Nuclon Delta	Thermo Scientific	168381	Cell culture, 8-OHdG experiments
Corning® 96-well Flat Clear Bottom Black Polystyrene TC-treated Microplates	Corning	3904	DCFDA-ROS detection
Corning® 96-well Clear Flat Bottom Polystyrene TC-treated Microplates	Corning	3598	Glucose/Lactate measurment
Costar 24-well Cell Culture Plateslates	Corning	3524	Tissue culture
Falcon 10 cm tissue culture dish	Corning	353003	Cell culture, inhibitor experimente
Primaria Easy Grip Cell Culture Dishes	Corning	353801	Cell culture, isolation of fibroblasts from patient samples

Table 3 b: Other consumables

Consumable	*Distributor*	*Product number*	*Used for*
Falcon® 25cm² Rectangular Canted Neck Cell Culture Flask (T25)	Corning	353108	Cell culture, isolation of fibroblasts from patient samples
Falcon® 75cm² Rectangular Canted Neck Cell Culture Flask (T75)	Corning	353136	Cell culture
Falcon® 150cm² Rectangular Canted Neck Cell Culture Flask (T150)	Corning	355001	Cell culture
Steriflip-GP	Merck Millipore	SCGP00525	Sterile filtering of FCS and other medium supplements
EASYstrainer 70 µm	Greiner Bio-One	542070	Isolation of mouse keratinocytes
Leica 818 High profile Microtome Blades	Leica Biosystems	14035838926	Cryotome sectioning
ProbeOn Olus Microscope slides	Fisher Biotech	15-188-52	Cryotome sectioning
LightCycler 480 multiwell plate 96, white	Roche	04729692001	qPCR

Table 3 c: Other consumables

Consumable	*Distributor*	*Product number*	*Used for*
Amicon® Ultra-4 Centrifugal Filter Unit	Merck Millipore	UFC801024	Sample centrifugation/protein removal from NMR samples
NMR glass tubes	Bruker		NMR measurements

Table 4: Cell culture medium and supplements

Cell culture medium/supplements	*Distributor*	*Product number*	*Used for*
CM-1Freeze medium	CLS	800125	Freezing cells for liquid nitrogen storage
DMEM Gibco	Thermo Fisher	11880036	Fibroblasts
DMEM 1g/L Glucose	PAN Biotech	P04-01159	Fibroblasts
DMEM wo Glucose, wo Pyruvate	PAN Biotech	P04-01548	Fibroblast and Mouse skin experiments
Dermal Cell Basal Medium	ATCC	PCS-200-030	Mouse keratinocytes and human melanocytes
Keratinocyte Growth Kit	ATCC	PCS-200-040	Culturing of murine keratinocytes
Adult Melanocyte Growth Kit	ATCC	PCS-200-042	Culturing of human melanocytes
Epi Life Keratinocyte medium	Thermo Fisher	MEPI500CA	Human Keratinocytes
Human Keratinocyte Growth Supplement	Thermo Fisher	S0015	Human Keratinocytes
Fetal+ High Performance Serum	anprotec	AC-SM-0161	Cell culture

Table 5: Cells

Cells	*Distributor*	*Product number*
Human Epidermal Keratinocytes, adult (HEKa)	Thermo Fisher	C0055C
Murine Keratinocytes	Self-isolated from donor mice (129 SV/EV)	-
Human Epidermal Melanocytes, adult (HEMa)	ATCC	PCS-200-013
NIH 3T3	Provided by Stefan Reich, AG Medenbach, University Regensburg	-
Re5 Fibroblasts	Self-isolated from patient at University Hospital Regensburg	-
WT01 Fibroblasts	Provided by Dr. Kamenisch, Self-isolated from patient at University Hospital Tuebingen	-

Table 6 a: Devices

Devices	*Distributor*	*Used for*
Sellamed 1200 Lamp	Sellas Medizinische Geräte GmbH	UVA irradiation
Luna FL Automated Cell Counter	Logos Biosystems, Inc.	Cell counting, Cell viability, cell size determination
NanoDrop 2000/2000C	Thermo Scientific	Determining DNA/RNA concentration in lysates (cells and skin)
Varioskan Flash	Thermo Scientific	Colorimetric and fluorimetric measurements of glucose, lactate, pyruvate and ROS
Heraeus Multifuge 3SR	Kendro Laboratory Products	Centrifugation of cells for cell culture experiments
PCV-2400 Combined Centrifuge/Vortex Mixer	Grant-bio	Centrifugation of Eppendorf cups.
miniSpin Centrifuge	eppendorf	Centrifugation of Eppendorf cups.
Centrifuge 5415R	eppendorf	Centrifugation of Eppendorf cups.
Vortexer	VWR International	Mixing of samples
Thermo Mixer Compact	eppendorf	DNA extraction
LightCycler 96	Roche	qPCR
Gel chamber	Bio-Rad	Electrophoresis of qPCR product
Power Pac 3000	Bio-Rad	Electrophoresis of qPCR product
Mini Shaker	VWR	Mixing of 96-well plates
Water bad VWB 12	VWR	Cell culture
CO_2 incubator CB 220 (E6)	Binder	Culturing of cells

Table 6 b: Devices

Devices	*Distributor*	*Used for*
CO_2 incubator Hera Cell	Thermo Scientific	Culturing of mouse skin explants
Cell culture bench Herasafe KS	Thermo Scientific	Sterile handling of cells
Microscope Labovert FS	Leitz	Microscopic imaging of cells
Camera Leica MC 170 HD	Leica	Microscopic imaging of cells
MJ Research PTC-200 Gradient Thermal Cycler	MJ Research	Reverse transcription
Axiostar Plus Microscope	Zeiss	Microscopic imaging of tissue sections
AxioCam ICc 1 Camera	Zeiss	Microscopic imaging of tissue sections
1556 Akku Electric Razor	Moser	Shaving of mouse skin
NMR-Spectrometer	Bruker	NMR measurements

Table 7: Programs

Programs	*Distributor*	*Used for*
GraphPad Prism 8.3.1	GraphPad	Statistical analysis
LightCycler 96 SW 1.1	Roche	qPCR analysis
NanoDrop 2000/2000C	Thermo Scientific	Determining DNA/RNA concentration in lysates (cells and skin)
Excel	Microsoft	Data calculation
Power Point	Microsoft	Picture design
SkanIt RE for Varioskan Flash 2.4.5	Thermo Scientific	Colorimetric and fluorimetric measurements of glucose, lactate, 8-OHdG and ROS
LAS V4.13	Leica	Cell culture imaging
Axiovision	Zeiss	Microscopic imaging of tissue sections
Chenomx Processor	Chenomx Inc.	Processing of NMR data
Chenomx Profiler	Chenomx Inc.	Evaluation of NMR data
TopSpin	Bruker	Processing of NMR data
AMIX	Bruker	Evaluation of NMR data
Cytoscape 3.7.2	Cytoscape Consortium	Mapping of metabolic network

Table 8: Special buffers

Buffer	*Composition*	*Used for*
P1-Buffer	20mM Sodium acetate 5mM Zinc chloride 50mM Sodium chloride pH 5.2	8-OHdG ELISA
PhosA-Bufer	10mM Tris HCl, pH 8 5mM Magnesium chloride 5mM Zinc chloride	8-OHdG ELISA
NMR-Buffer (pH 7.4; 0.1 M)	8.02 ml 1 M K_2HPO_4 1.98 ml 1M KH_2PO_4 Fill up to 100 ml with H_2O dest. 30 mg Borat 25 ml D_2O containing TSP	NMR

2.2. NMR-Spectroscopy – background and applications

2.2.1. Principles of NMR-spectroscopy

In the complex structure of a molecule, every atom consists of a nucleus and an electron cloud. The nucleus contains positively charged protons and neutrons that possess no charge. The behaviour of the charged nucleus in an externally applied magnetic field is the foundation upon which the nuclear magnetic resonance (NMR) spectroscopy is performed. NMR is a non-invasive technique that does not require sample separation or derivatization and yields results even with small sample concentrations down to the low micromolar range, making it the perfect tool for a high-throughput metabolic analysis of biological samples (95).

2.2.1.1. Characterisation of the atomic nucleus

If one assumes that an atomic nucleus is spherical and rotates around its axis, then it should possess a nuclear angular momentum **P** (96). However, the nucleus is not a homogeneous entity but, as mentioned above, consists of protons and neutrons who also possess their own spin. The nuclear spin angular momentum is a vector quantity with magnitude given by equation (i) in which ***I*** (*I* = 0, ½, 1, 3/2 and up to 7) is the angular momentum quantum number and **h** the Plank's constant. For each nucleus, *I* is, in turn, a vector combination of the proton and neutron spins. When a nucleus possesses even numbers of both protons and neutrons, their spins are "paired", resulting in *I* = 0 and subsequently a nuclear spin angular moment that also equals zero. Only nuclei with a nuclear spin angular momentum unequal to zero (i.e. *I* ≠0) are NMR active (96, 97).

(i)

$$\vec{P} = \frac{h}{2\pi}\sqrt{I(I+1)} = \hbar\sqrt{I(I+1)}$$

Since the magnetic moment is connected to the spin angular momentum, namely it is proportional to the angular momentum **P** and the gyromagnetic ratio **γ**, it can be described as follows:

(ii)

$$\vec{\mu} = \vec{P}.\gamma$$

Normally in a three-dimensional space (described by x-, y- and z-axes), the protons of the nucleus have no specific orientation. However, if a strong magnetic field **B_0** is applied to the particle along one of the axes (for example z), this leads to the re-orientation of the magnetic fields of the particles along the applied field.

Another important attribute of the proton should be also taken into consideration, namely the directional quantum number **m_I**. Under non-magnetized conditions, the nuclei have no specific orientation. In an applied magnetic field **B_0**, the directional quantum number can assume values **m_I** = I, I-1,…, -I. Especially ^{1}H and ^{13}C nuclei with I = ½, **m_I** has only two possible values (+1/2 and -1/2), meaning the nuclei can be either parallel or anti-parallel to the magnetic field. Each of these orientations has its own energy levels, with the anti-parallel one possessing a higher energy state than the parallel one (see Fig. 4).

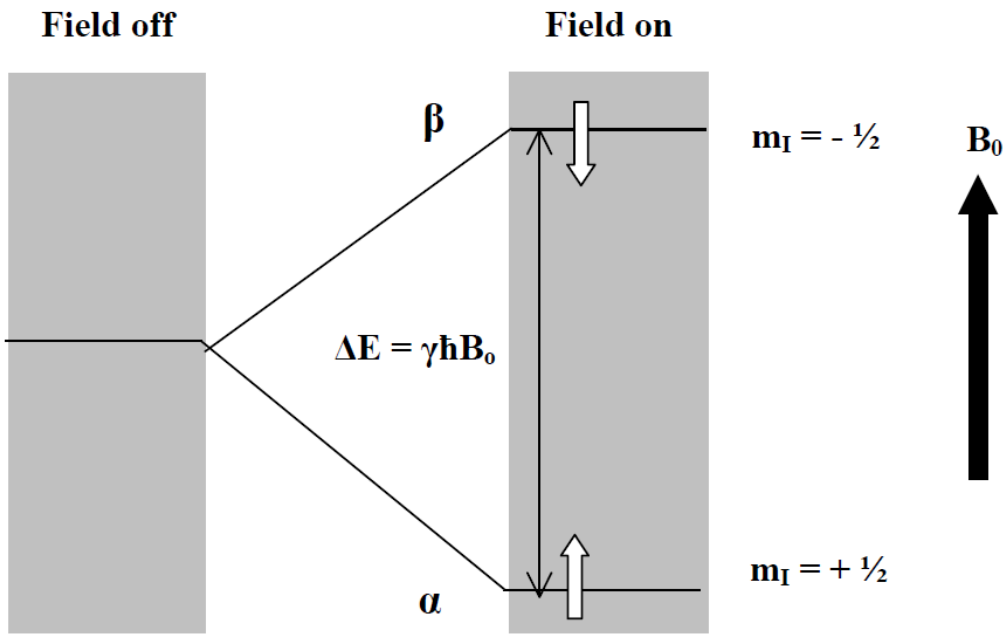

Fig. 4: Energy levels of a ½-spin nucleus in an applied magnetic field B_0. (Graph from Gerothanassis et al. 2002 (96).)

This difference in energy is described by the magnetic and angular momentum of the particle in the applied magnetic field by combining equation (i) with the values for the nuclear quantum number m (m = +/- ½ for ^{1}H protons):

(iii)

$$\overrightarrow{P_z} = \hbar m$$

(iv)

$$E_m = -\gamma P_z B_o$$

The difference between the two energy states for orientations parallel and anti-parallel to the field can be thus expressed as:

(v)

$$\Delta E = \gamma \hbar B_o$$

As evident from equation (v) $\Delta \boldsymbol{E}$ is proportional to the strength of the applied magnetic field, with stronger magnets resulting in higher energy difference between the states. The higher $\Delta \boldsymbol{E}$ the larger the population difference between parallel and antiparallel orientation of the nuclei. This population difference will then be exploited in the respective NMR experiment to induce an electric signal in the receiver coil. The stronger the detected signal, the more exact the measurement. A stronger signal can also be achieved by choosing nuclei with a higher gyromagnetic ratio and high natural abundance, making ^{1}H a highly popular NMR target.

In addition to the differences in alignment and energy between the particles, the applied magnetic field results in a gyroscopic movement of the magnetic field of the nucleus known as Larmor precession. The precession frequency $\boldsymbol{\nu_0}$ is described by the following equation:

(vi)

$$\nu_0 = |\gamma| B_0 / 2\pi$$

However, since the nucleus is shielded from the external magnetic field $\mathbf{B_0}$ by the electron cloud enveloping it, the magnetic field that it experiences differs from the one actually applied. Therefore, the precession frequency should be corrected for the electron shielding σ (98):

(vii)

$$\nu_0 = |\gamma| \frac{B_0}{2\pi}(1-\sigma)$$

The nuclear precession results in an angle **θ** between the nuclear magnetic moment **μ** and the applied magnetic field $\mathbf{B_0}$ (see Fig. 5 A). If in addition to $\mathbf{B_0}$ a second weaker magnetic field $\mathbf{B_1}$, perpendicular to the $\mathbf{B_0}$-**μ** plane is applied, usually supplied by radio frequency (rf) magnetic waves, a torque is exerted on the magnetic moment **μ**, followed by an increase in **θ** (Fig. 5 B). When the frequency of the secondary field $\mathbf{B_1}$ is equal to the Larmor precession frequency of the nucleus, it results in the transition of the proton from one energy level to another. This condition is described as resonance.

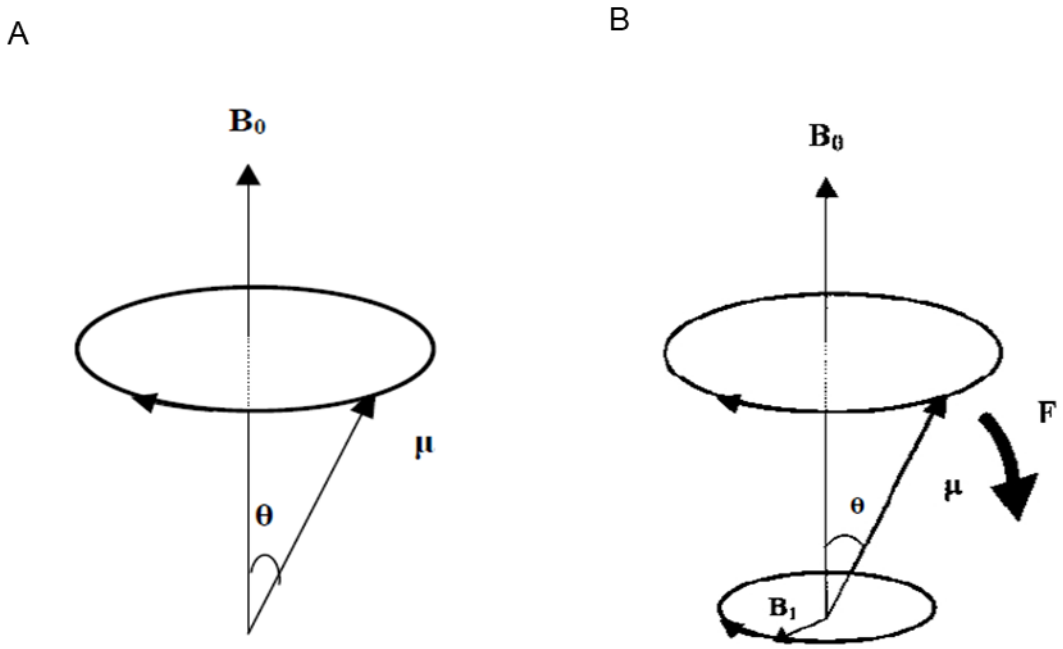

Fig. 5: (A) Precession of the magnetic moment μ in an applied external magnetic field B_0. (B) Influence of a rotating weak magnetic field B_1 (perpendicular to the B_0-μ plane) on the precession of the magnetic moment μ. The generated force F results in increasing θ, the angle between μ and B_0. (Graphs modified from Gerothanassis et al. 2002 (96).)

To be able to use this resonance for NMR spectroscopy, the secondary rf-field is applied until the proton, initially rotating around the z-axis along the primary magnetic field $\mathbf{B_0}$, tilts by 90° and starts rotating in the x-y-plane. Consequently, in a receiver coil mounted in the x,y-plane an electric signal called free induction decay (FID) will be induced. With no additional rf-field applied, the particles tend to return to their initial

orientation in a process known as relaxation. There are two different components in nuclear relaxation – longitudinal (spin-lattice) relaxation and transversal (spin-spin) relaxation, both occurring during distinct time periods. The longitudinal relaxation represents the energy exchange between the spin states and the surrounding medium. It is described by the time T_1 needed by the protons to reach equilibrium magnetization, returning to their initial orientation before the application of the rf-field. In summary, the spin-lattice relaxation influences the lifetime of the spin energy populations. The spin-spin relaxation, or transverse relaxation, on the other hand, represents the energy exchange between the different nuclear spins themselves. Described by time T_2 it determines the duration of the FID signal. During the spin-spin relaxation, a process called 'fanning' occurs, diminishing the strength of the received signal, despite the magnetic moments of the population still being aligned with the x-y-plane. The strength of the detected signal is proportional to the total magnetic moment of the sample, which is, in turn, linear to the total number of nuclei re-oriented by the rf-pulse (99). This can also be used for metabolite quantification since stronger signals correlate to a higher abundance of the corresponding compound in the sample.

The interactions between the different atoms in a molecule can influence the relaxation times, providing more information about the molecular structure and chemical interactions. There are two effects that are mainly used to identify different compounds in a complex solution – chemical shift and spin-spin coupling.

2.2.1.2. The chemical shift

As mentioned above, due to the shielding of the electron cloud, the effective magnetic field influencing the nucleus differs from the applied one The precession frequency of the proton depends on the electron shielding, which implies that the resonance frequency required to achieve it also depends on the shielding, as illustrated in equation (vii). Not only the electrons directly surrounding the nucleus of interest (for example ^1H) but also the surrounding atoms in a chemical group exert influence on the shielding of the proton. Therefore, ^1H protons in OH- and CH_3-groups for example have different electron shielding and precession frequencies, resulting in different resonance frequencies. These differences in resonance, compared to the expected values for an unshielded proton, are known as chemical shifts **δ** (100). Chemical shifts are presented in parts per million (ppm) and are described by the equation:

(viii)

$$\delta_x = \frac{\omega_x - \omega_{TMS}}{\omega_0} \cdot 10^6 = \frac{1-\sigma_x - (1-\sigma_{TMS})}{1-\sigma_0} \cdot 10^6$$

Where ω_{TMS} stands for the precession frequency of a reference compound (Trimethylsilylpropanoic acid (TSP)) which gives a single signal at a position where usually no other signals are expected, ω_x is the precession frequency of the substance of interest, ω_0 is the precession frequency of the rotating frame, and σ is the corresponding shielding. It is considered that the position of the reference signal has **δ** = 0 (96, 100).

2.2.1.3. Spin-spin coupling

Another important aspect to take into account when characterizing a measured compound is the spin-spin coupling. It arises due to interactions between neighbouring nuclei in a molecule. The magnetic field created by each nucleus influences the overall magnetic field experienced by the rest of the nuclei and thus modifies their resonance frequencies. There are two major coupling effects that can influence the NMR-readout – the scalar and the dipole coupling.

The interactions between nuclei facilitated by the bonding electrons are represented by the scalar or J-coupling constant $^{n}\mathbf{J_{ax}}$, where n indicates the number of covalent bonds separating two nuclei a and x. Since the scalar coupling is independent of the applied magnetic field, it is expressed in hertz (Hz) and not in ppm. The magnetic field from the nucleus influences the surrounding electron cloud, which in turn influences the electron cloud around the neighbouring proton, thus further relaying the influence of the first nucleus. The strength of the scalar coupling is dependent on the number of bonds separating two interacting nuclei but not on the molecule's orientation (96, 100).

A molecule experiencing scalar coupling shows a distinct pattern in its NMR spectrum. This pattern depends on the chemical shift between the nuclei and the number of interacting spins. Nuclei, possessing the same magnetic environment, as in the case of the ^{1}H nuclei of a CH_3Cl molecule, are called equivalent and yield a single signal in an NMR spectrum. The number of signals depends on the number of non-

equivalent groups in a molecule. For example, in ethanol (CH_3CH_2OH) there are three distinct groups – methyl, methylene, and hydroxyl, resulting in three separate signal groups. The number of multiplets in a group, on the other hand, depends on the number of the neighbouring nuclei (n), leading to splitting the signal into n+1 peaks. This means that the methyl group of ethanol will have a triplet signal due to the neighbouring methylene group (i.e. nuclei in methylene being n=2).

2.2.1.4. Fourier transformation

As discussed in 2.1.3. every nucleus and functional group in a molecule have specific characteristics allowing them to be identified in an NMR spectrum. However, the initial read-out from am NMR spectrometer (i.e. the measured FID) is a sinusoid function of time where there is no clear distinction between the different functional groups of a compound. Since the FID signal cannot be directly used for identification or quantitation of the measured sample, the readout is mathematically transformed using the so-called Fourier transformation (100). As mentioned, the FID acquired by the spectrometer is a function of time, with the intensity being measured at discrete time intervals. The Fourier transformation processes the FID into a frequency magnetic resonance function as shown in Fig. 6 (100-102).

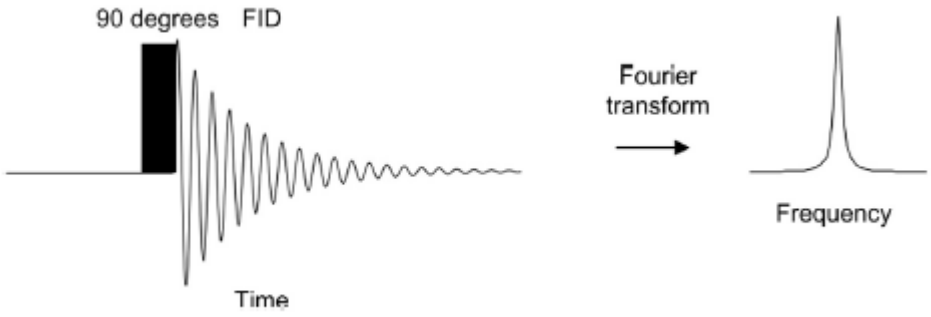

Fig. 6: Fourier transformation of FID into a resonance function spectrum. (Graph adapted from Trindade and Lourol 2020 (102).)

2.2.2. 1D and 2D NMR

Using the NMR technique, it is possible not only to identify different compounds in a complex mixture such as cell lysate or supernatant but also to quantify them using the area under the spectral curve. Since the majority of organic compounds are rich in hydrogen, using ^{1}H-NMR is an appropriate choice for performing sample analysis.

There are two major approaches to acquire an NMR spectrum – performing a one-dimensional (1D) or multi-dimensional screening (95, 99, 103).

In the ^{1}H-1D-NMR, as described above, the hydrogen nuclei are excited by a radiofrequency pulse, the resulting signal is measured and Fourier transformation is performed thereafter. This results in a spectrum with a single frequency-axis, i.e. 1D-spectrum. A multi-dimensional NMR relies on additional frequencies generating multiple 1D-spectra that are later used to create a multi-dimensional 'map' of the screened compounds. In this work, a two-dimensional (2D) NMR was performed on selected samples.

Both 1D and 2D-NMR have their advantages and disadvantages. Using a single radio frequency-domain makes the 1D-NMR very fast and suitable for high-throughput measurements. However, conventional 1D-NMR has its limitations. Many biological samples, such as milk, blood, urine, or even some cell culture media, contain a high amount of protein. Such macromolecules need to be removed from the sample by ultrafiltration to achieve narrow and well-defined peaks. Broad NMR-peaks hinder peak discrimination and hide the signals of smaller molecules, leading to a low resolution of the spectrum. To resolve this, the typically fast transverse relaxation of proteins is used in combination with a Carr-Purcell-Meiboom-Gill sequence (CPMG), yielding a 'clean' 1D spectrum(104). Another problem of 1D-NMR is signal overlap. Since a single frequency-axis is used to excite the nuclei, molecules with similar resonance frequencies end up with signals stacking over each other. This makes the identification of certain metabolites difficult in a simple 1D-NMR(105).

In order to overcome signal overlap, a multi-dimensional NMR is a good alternative to 1D measurements. The principle used in these multiple acquisitions lies for example in the polarization transfer between J-coupled nuclei. In this case, the polarization from the more "sensitive" ^{1}H-nuclei is transferred to the "less sensitive" ^{13}C nuclei and is then re-transferred back to ^{1}H. In the case of 2D-NMR, series of FIDs are acquired and combined to a "data matrix" and two orthogonal Fourier-transforms are performed on this data matrix resulting in a spectrum with two frequency axes. The first axis, also called "direct dimension", usually represents the ^{1}H chemical shift. The second axis, or "indirect dimension", can be comprised of either ^{1}H shifts or of heteronuclear shifts (i.e. ^{13}C), depending on the experiment (95, 106). In this work, a heteronuclear single quantum coherence spectroscopy (HSQC) was used on a subset

of samples. The HSQC method uses the chemical shift of the ^{13}C nuclei for the “indirect dimension”. Since the natural abundance of ^{13}C atoms is low, only 1/100 of the molecules give a response, which makes 2D-HSQC-NMR perfect for labelling experiments. The downside of this method is time. Since multiple 1D-spectra have to be acquired in order to obtain a good 2D-matrix, the measurement duration per sample increases (95).

2.3. Methods

2.3.1. Culturing of human and murine skin cells

All cells were cultured at 37 °C and 5% CO_2. Human WT01 (107) and Re5, and murine (NIH 3T3) fibroblasts were cultured in DMEM medium containing 10 % FCS, 1g/L (5.5 mM) glucose, 1 mM pyruvate, and 2 mM L-glutamine. For adult human keratinocytes HEKa special keratinocyte medium from GIBCO was used containing 1g/L (5.5 mM) glucose. Mouse keratinocytes were kept in an ATCC keratinocyte medium containing 1 g/L Glucose, 0.52 mM pyruvate, 6mM L-glutamine. For the adult human melanocytes HEMa special ATCC melanocyte medium with 1g/L (5.5 mM) Glucose, 0.52 mM pyruvate, 6mM L-glutamine was used.

2.3.2. Isolation of human fibroblasts

Skin biopsy sample was obtained from the University Hospital Regensburg (Ethic vote number 14101 0001) and given the designation Re5. Due to the small sample size, it was not possible to use a standard isolation protocol (see 2.3.3). Therefore, the skin biopsy was put whole on a Primaria cell culture dish, containing a single drop of DMEM-Cipro (1 g/L glucose (5.5 mM), 10% FCS, 1% Penicillin/streptomycin, 1% Ciprofloxacin) and incubated for 30 min at 37 °C to ensure that the skin sample sticks on the dish surface. Afterward, 3 ml DMEM-Cipro was added to the skin sample. It was cultivated at 37 °, 5% CO_2 until cell-outgrowth was enough for a transfer to a T25 cell culture flask. Subsequently, the cells were transferred to a T75 flask, cultured in DMEM without Ciprofloxacin, and used for further experiments.

2.3.3. Isolation of mouse keratinocytes

Keratinocytes were isolated from 129 Sv/Ev WT mouse tails. After sacrificing the mice the tails were put for 1-2 min in Braunol solution for disinfection and were subsequently washed with PBS. Afterward, the tails were dipped for ca. 1 min in 70% ethanol and washed again with PBS. The skin was then separated from the tail using a scalpel and tweezers and cut into small pieces. The pieces were placed in a 6-well-plate and incubated in trypsin/PBS solution (dilution 1:2) overnight at 4 °C. The next day the dermis and epidermis were separated and keratinocytes were isolated from the epidermis.

The epidermis was cut into even smaller pieces with a scalpel so that they could pass through a 10 ml pipette. The pieces were re-suspended in DMEM, transferred to a falcon tube, and centrifuged for 5 min at 1200 rpm. The supernatant was discarded; the pellet was reconstituted in ATCC keratinocyte medium and pipetted over a 70 µm cell strainer into a new falcon tube. The cell strainer was washed 1x with ATCC keratinocyte medium. The flow-through was centrifuged for 5 min at 1200 rpm. The supernatant was discarded and the cell pellet was re-suspended in ATCC keratinocyte medium and plated on a 6-well plate. A single skin cell sample was distributed equally between 3 wells. Cells were cultured for 5 days at 37 °C with 5% CO_2. Afterward, the irradiation protocol was started as described below (see 3.2.6.).

2.3.4. Isolation and culturing of murine skin ex vivo

129 Sv/Ev WT mice were sacrificed and their backs shaved. The back skin was cut out and stretched evenly. 8 mm in diameter skin punches were taken and immediately transferred on a 24-well plate containing 2ml standard DMEM containing 10 % FCS, 1 g/L glucose, 1 mM/100 µM pyruvate, 2 mM L-glutamine, and 1% Amphotericin B (2,5 µg/ml end concentration). In the first experimental setup, the skin was irradiated directly after isolation. In the second experimental setup, the punches were pre-incubated for one day. Afterward, the punches were transferred to a fresh 24-well plate, containing 2 ml standard DMEM. Afterward, the irradiation was started as described in 2.3.5.

2.3.5. Irradiation protocols for skin cells and explants

2.3.5.1. Irradiation of cells

The irradiation of skin cells was performed as follows. For human Re5 and murine fibroblasts, as well as human keratinocytes, $5x10^4$ cells per well were seeded on a 6-well plate and left to grow overnight. Human fibroblasts WT01 were seeded at density $2x10^4$ cells/well, due to differences in growth speed, compared to Re5. Mouse keratinocytes were cultured as described in 2.3.3 before irradiation. Human melanocytes were seeded at a density of $2x10^4$ cells per well on a 6-well-plate. The cells were left to grow for 3d before the irradiation was started.

The standard irradiation protocol is shown schematically in Fig. 7.

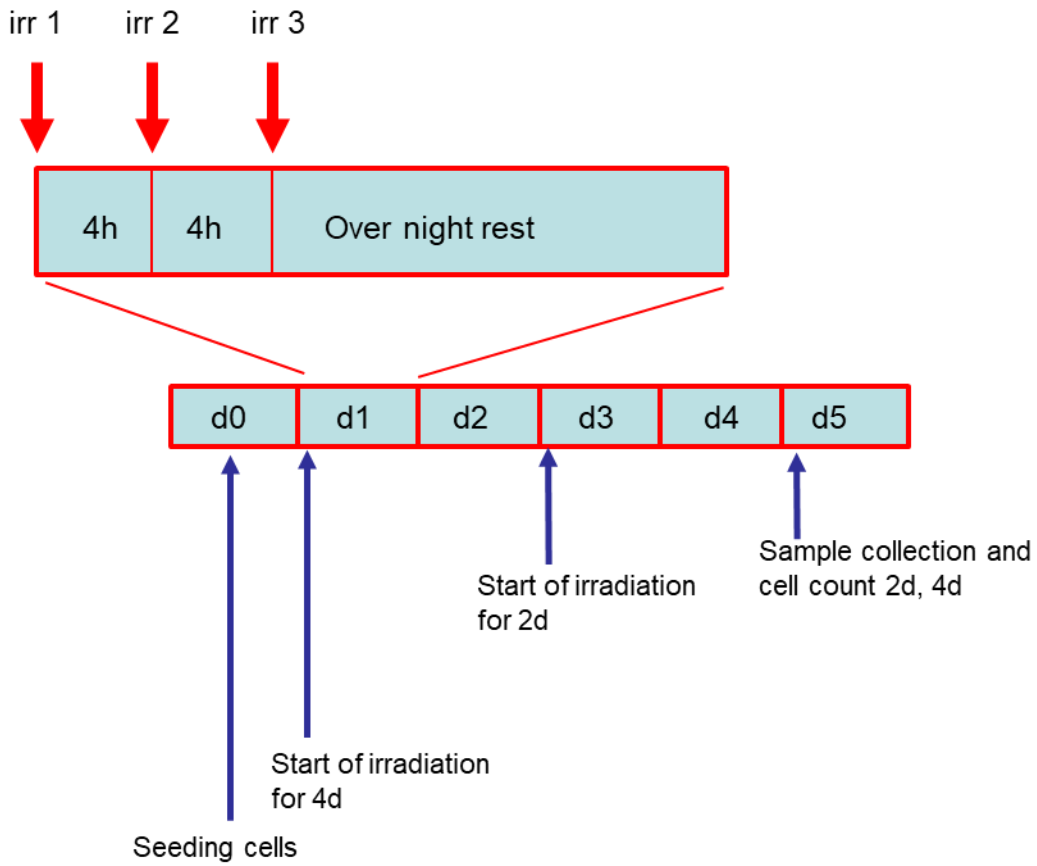

Fig. 7: Graphic representation of the standard irradiation protocol performed on skin cells.

At the beginning of irradiation, the medium was aspirated from each well. Cells were irradiated in 1ml PBS. The amount of UVA per single irradiation was set at 6 J/cm^2 and provided by a Sellamed-Lamp (emission spectrum 340-420 nm, see Fig. 8). This particular dose was chosen since it closely correlates with the solar exposure received after an hour outdoor activity in the northern hemisphere (Potsdam, Hohenpeissenberg) (108). The cumulative daily irradiation dose of 18 J/cm^2 also lies below the pathologic minimal erythema dose for UVA which is around 37 J/cm^2 (109). The PBS was then aspired and 5 ml fresh medium was added to each well after the first irradiation. Before all subsequent irradiations, the medium was aspirated and collected in separate falcons and returned to the corresponding wells afterward. Three irradiations per day were performed. There was a 4h resting period between single irradiations with ON rest after the last daily irradiation. The duration of total irradiation was 4 days. Before the first irradiation of day 3, 1 ml fresh medium was added to each well to compensate for any medium loss. Early on day 5, the supernatant was collected for further analysis and the cells were counted.

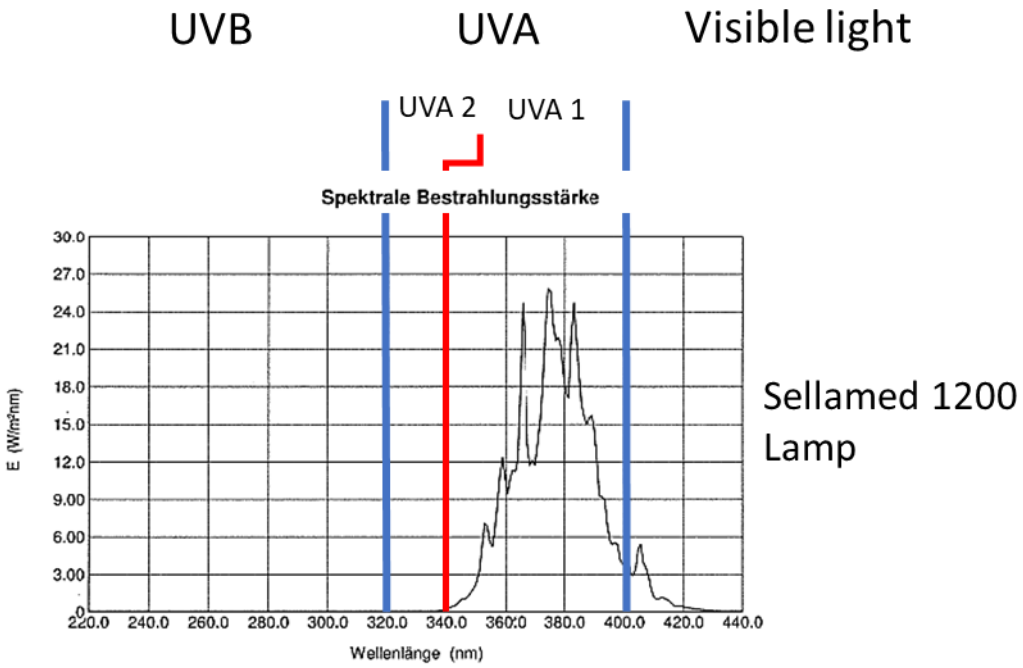

Fig. 8: Spectral profile of Sellamed 1200 lamp used in all irradiation experiments. (Graph modified from Sellamed manual).

2.3.5.2. Irradiation of mouse skin

The irradiation for the skin explants was shorter than the one for cells with only 2 days of irradiation (see Fig. 9). This was necessary in order to prevent necrosis from culturing the skin biopsy for too long *ex vivo*. For the initial stages of the *ex vivo* experiment skin punches (8mm diameter) from 129 Sv/Ev WT mice were taken and cultured in standard DMEM (1g/L glucose, 1mM pyruvate, 2mM L-glutamine) with additional Amphotericin to prevent fungal contamination. Irradiation was performed immediately after the skin isolation for 2 days 3-times per day with 6J/cm^2 UVA per single irradiation, provided by Sellamed-Lamp. The culture medium was irradiated together with the skin biopsy contrary to the standard cell-irradiation protocol. This was necessary due to technical difficulties and increased danger of contamination in case the biopsy was transferred to PBS before each irradiation cycle.

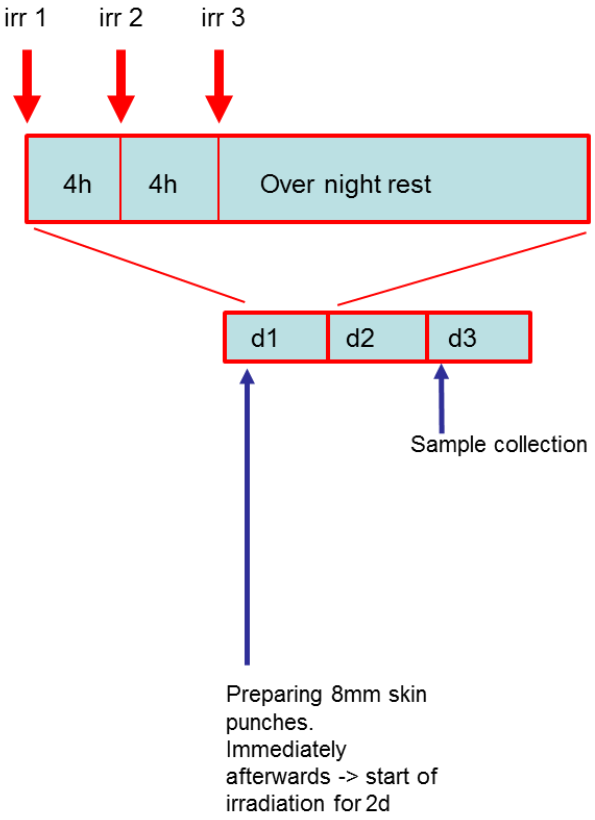

Fig. 9: Irradiation protocol for mouse skin ex vivo.

In the second experimental setup, an additional pre-incubation step overnight was added before the beginning of irradiation. At the end of both experiments, the supernatant was collected for further use. The metabolic changes were detected via CPMG-NMR analysis. Since the skin punches were of equal size and no significant medium loss was detected, no normalization to volume or weight was performed during the data evaluation.

2.3.6. Colorimetric detection of glucose

To determine the glucose consumption an enzymatic assay was performed using Glucose Assay Kit from Sigma (GAGO20). The principle of the detection is described in Fig. 10.

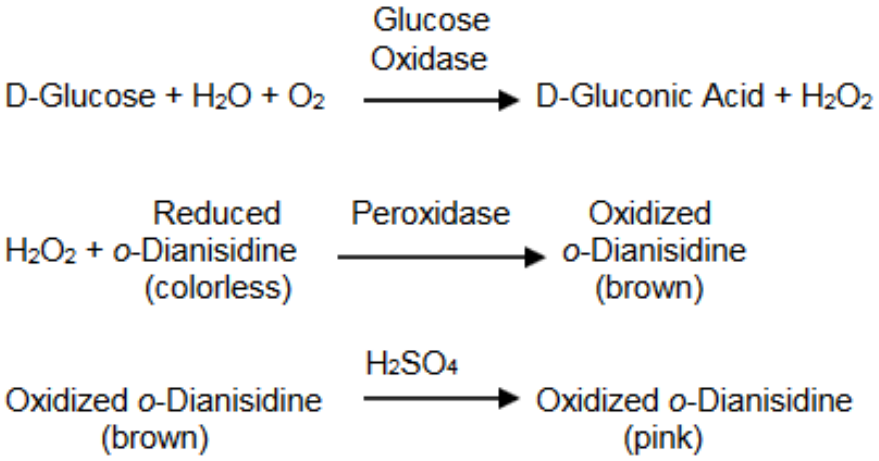

Fig. 10: Colorimetric detection of glucose using a Glucose Oxidase/Peroxidase reaction as shown in the Sigma-Aldrich manual for GAGO20 kit.

The supernatant samples were diluted 1:20 in water. As a reference, fresh medium (without cells) was diluted 1:50 in water. A single point standard was prepared by diluting 5 µl stock glucose solution (provided in the kit) in 95 µl water to a final concentration of 50 µg/ml. Afterward, all supernatant samples, medium samples, standard, and blank (water) were pipetted in duplicates on a clear flat-bottom 96-well plate (25 µl sample per well). To each well 50 µl assay solution was added and the plate was incubated for 30 min at 37°C in the dark. Subsequently, 50 µl sulfuric acid was added to each well to stop the reaction and the plate was measured at 540 nm with Varioscan Flash.

To calculate the glucose concentration Formula (ix) was used.

(ix)

$$mg/ml = \left(\frac{(A_{540}\ Sample - A_{540}\ Blank) * 0{,}05}{A_{540}\ Standard - A_{540}\ Blank}\right) * dilution$$

A_{540} is the mean of the absorption measured for each duplicate sample, standard or blank.

The concentration of glucose at the beginning of the experiment (mg/ml_{start}) was calculated from the values for fresh medium (without cells). To calculate the total amount of glucose the concentration per milliliter was multiplied with the volume of supernatant determined at the end of the experiment (V_{end}). Since there was medium loss during the experiment due to the frequent medium transfer before and after

irradiation, the volume at the beginning of the experiment was set as a mean of the end volumes of all samples (MV_{end}). The milligrams of consumed glucose (mg_{cons}) were calculated by subtracting the amount of glucose at the end of the experiment from the amount of glucose at the beginning, as shown in Formula (x).

(x)

$$mg_{cons} = \left(\left(\left({}^{mg}/_{ml}\right)_{start} * MV_{end}\ [ml]\right) - \left(\left({}^{mg}/_{ml}\right)_{end} * V_{end}\ [ml]\right)\right)$$

In the end, the amount of glucose was normalized to the number of cells in million (N) and re-calculated in mmol, yielding a final amount of consumed glucose in mmol/10^6 cells (see Formula (xi)).

(xi)

$${}^{mmol}/_{10^6\ cells} = \left(\left(\frac{mg_{cons}}{N}\right)/180\right)$$

The final results were plotted using GraphPad Prism 7.02.

2.3.7. Colorimetric detection of lactate

The detection of lactate in the supernatant was performed with two different colorimetric kits. The initial one was provided by Trinity Biotech. The product was discontinued during the experimental phase, which led to the implementation of an alternative kit from Sigma-Aldrich. Control tests showed that both kits yielded almost identical results when used on the same sample. Therefore, there was no discrimination between samples measured with Trinity Biotech and Sigma-Aldrich during the evaluation.

Protocol for Lactate kit (Trinity Biotech)

The samples for lactate measurement were not diluted. A single point standard was used during the measurements. 2 µl from each supernatant sample, medium sample, standard (40 mg/dl stock from Trinity Biotech), and blank (water) were pipetted in duplicates on a clear flat-bottom 96-well plate. To each well, 200 µl lactate reagent

was added and the plate was incubated for 10 min at 37 °C in the dark. Thereafter, the absorption was measured at 540 nm with Varioscan Flash.

The lactate concentration was calculated using Formula (xii).

(xii)

$$mg/_{ml} = \left(\left(\frac{(A_{540}\ Sample - A_{540}\ Blank)}{A_{540}\ Standard - A_{540}\ Blank}\right) * 40\right)/100$$

A_{540} is the mean of the absorption measured for each duplicate sample, standard or blank.

Similar to the calculation for glucose consumption shown in 2.3.6 the calculation of lactate production was first normalized to sample volume. V_{end} is the supernatant volume at the end of the experiment, MV_{end} is the mean of the end volumes of all samples, used to compensate for medium loss during irradiation, and mg/ml_{start} is the concentration of lactate in the fresh medium (without cells). The lactate (mg_{prod}) was calculated by subtracting the amount of lactate at the beginning of the experiment from the amount of lactate at the end, as shown in Formula (xiii).

(xiii)

$$mg_{prod} = \left(\left(\left(mg/_{ml}\right)_{start} * MV_{end}\ [ml]\right) - \left(\left(mg/_{ml}\right)_{end} * V_{end}\ [ml]\right)\right)$$

The total amount of lactate production was normalized to the number of cells in million (N) and re-calculated in mmol, yielding a final amount of produced lactate in mmol/10^6 cells (see Formula (xiv)).

(xiv)

$$mmol/_{10^6\ cells} = \left(\left(\frac{mg_{prod}}{N}\right)/90\right)$$

The final results were plotted using GraphPad Prism 8.3.1.

Protocol for Lactate kit (Sigma-Aldrich)

The supernatant samples were diluted 1:40 in water, the fresh medium was measured undiluted. A standard curve was used to determine the sample concentration. The standard solution was prepared to a working concentration of 1 nmol/µl as stated in the kit-manual and 0/1/2/3/4/5 µl were pipetted in duplicates on a clear flat-bottom 96-well plate, yielding 0/1/2/3/4/5 nmol/well standard. The final volume per well was filled up to 25 µl.

For the detection reagent, a master mix was prepared for each sample, containing 23 µl Assay Buffer, 1 µl Enzyme Mix, and 1 µl Probe. Each supernatant sample and medium sample were pipetted in duplicates (25 µl per well). To each well, 25 µl from the master mix were added and the plate was incubated for 30 min at room temperature protected from light. The absorbance was measured at 570 nm with Varioscan Flash. To calculate the nmol in the unknown sample (Sa) the plotted standard curve was used (see Formula (xv)).

(xv)

$$Sa = (A * MS) + B$$

In Formula (xv) MS is the mean absorbance of a sample duplicate, ***A*** is the slope of the standard curve, and ***B*** is the intercept with the y-axis. From this, using Formula (xvi) the concentration in mg/ml was calculated.

(xvi)

$$^{mg}/_{ml} = \left(((Sa/25) * 90)/1000\right) * dilution$$

To calculate the total amount of lactate production in mmol/10^6 cells Formula (xii) and (xiv) were used. In the end, the results were plotted using GraphPad Prism 8.3.1.

2.3.8. NMR sample preparation and analysis

After the UVA treatment, the supernatant from the cell samples as well as control media without cells was preserved at -80 °C before further preparation. For the NMR analysis, the samples were separated into two main categories – 1. Unfiltered samples for CPMG-measurement (1D-NMR); 2. Filtered samples for 2D-NMR (HSQC).

The preparation of the unfiltered samples was performed as follows. After thawing and thoroughly vortexing the samples for 30 s each, the samples from the ^{13}C-labelling experiments were filtered through a 10 kD Amicon filter for 1 hour at 4 °C and 4000 G to remove proteins (the Amicon filters were pre-washed with water for 30 min at 4000 G prior to use). The rest of the measured samples were not filtered. Instead, formic acid was spiked into each sample to a final concentration of 2.05 mM. Following that, 400 µl from each sample and 250 µl NMR-Buffer (for composition see Table 8: Special buffers) containing 6.025 mM TSP, and pipetted in glass NMR-vials.

Unfiltered samples were used for 1D-CPMG-NMR and formic acid was used as a reference for quantitation.

Filtered samples were used for 1D-CPMG- and 2D-HSQC-NMR. In both cases, TSP was used as a reference for quantitation.

The data acquired from the NMR-spectrometer were then processed with TopSpin 3.1 to adjust the baseline, phase and reference and then imported in Chenomx 8.6 for final quantitation of the metabolites. The concentration of metabolites in the cell supernatants ($\mathbf{c_S}$) and in the fresh medium ($\mathbf{c_{med}}$) were used together with the sample volume ($\mathbf{vol_S}$) and the end number of cells to calculate metabolism per million cells. For that equation (xvii) was used.

(xvii)

$$mmol \Big/ 10^6\ cells = \frac{(C_{med} * AVERAGE\ vol_S[L]) - (C_S * vol_S[L])}{10^6\ cells}$$

A modification of equation (xvii) was used for calculating the amount of labelled metabolites in a sample in section 2.3.9).

2.3.9. Treating cells with pyruvate and glucose (labelled/unlabelled)

Pyruvate labelling:

The cells were plated on 6-well plates at density 5x10^4 cells per well in 2 ml standard DMEM medium(1 mM) and incubated overnight at 37 °C. The following day a complete medium exchange was performed with DMEM containing 1 mM of ^{13}C-

Pyruvate (Sigma Aldrich; 490717). Standard 4-day irradiation was performed as described in 2.3.5.

Glucose labelling:

The cells were plated on 6-well plates at density $5x10^4$ cells per well in 2 ml standard DMEM with and without Pyruvate (0 mM/1 mM) and incubated overnight at 37 °C. The following day a complete medium exchange was performed with DMEM containing 1 g/L (5.5 mM) C_{13}-Glucose (Eurisotop; CLM-1396-1) and unlabelled Pyruvate (0 mM/1 mM). Standard 4-day irradiation was performed as described in 2.3.5.

Labelling detection and calculation:

For calculating the amount of labelled compounds, the ratio of labelled to unlabelled sample was used. In particular, metabolites, with the exception of lactate and glucose, were measured using 2D-HSQC NMR. After performing base line and phase correction, the resulting peaks were imported in the AMIX software where an automatic peak-picking was performed. The spectra of the labelled and unlabelled samples were overlayed and metabolites with increased signals after labelling were noted. The peak volume (PV) of the labelled metabolites and the corresponding ones from the unlabelled samples were calculated. Afterward, the ratio of the PV for the metabolites was divided by the PV of the TSP reference signal to compensate for pipetting errors of the samples. The resulting metabolite/TSP-ratios of the labelled samples were then divided by the corresponding metabolite/TSP-ratios of the unlabelled controls, resulting in the labelling coefficient **LC**(% labelling from total metabolite detected) – complete labelling would result in an LC of 100, half-labelling would result in an LC of 50 and so on. The labelling coefficient was then used to calculate the absolute values of the labelled compounds. Since the labelling itself is not supposed to influence the uptake of the labelled compound (pyruvate or glucose) by the cells, the unlabelled samples measured in Cenomx were used as an output value for the calculation (differences due to slight variations in the end volume and the number of cells between experiments were deemed negligible). The output values were multiplied with the labelling factor divided by 100 and the absolute amount of labelled substance was then calculated as described in 2.3.8. by modifying equation (xvii) as follows:

(xviii)

$$mmol/_{10^6\ cells} = \frac{((C_{med} * AVERAGE\ vol_s[L]) * (LC/_{100})) - ((C_s * vol_s[L]) * (LC/_{100}))}{10^6\ cells}$$

As for calculating the amount of labelling in glucose and lactate, an additional Chenomx database for labelled compounds was downloaded and the samples were calculated as described in equation (xvii) in section 2.3.8.

2.3.10. RNA extraction

RNA extraction from the treated cells was performed via NucleoSpin RNA-isolation kit. All buffers listed below were contained in the kit.

The UVA treated cells (for irradiation protocol see 2.3.5.) were trypsinized, counted, and re-suspended in 350 µl buffer RA1 and 3.5 µl 2-Mercaptoethanol per sample to initiate cell lysis. The mixture was vortexed and 350 µl/sample of 70% ethanol were added and homogenized by pipetting several times. The samples were thereafter loaded on RNA-binding columns and centrifuged at 13000 rpm for 1 min. 350 µl from buffer MDB were added to each column and the samples were centrifuged again at 13000 rpm for 1 min. DNase reaction mixture was then prepared by diluting the stock solution 1:10 in DNase reaction buffer. 95 µl of the working solution was added to each column and the samples were incubated for 15 min at room temperature. After the end of incubation, 200 µl from RAW2 buffer was added to each column, followed by 1 min centrifugation at 13000 rpm. For the second wash, 600 µl buffer RA3 was added to the samples and the columns were again centrifuged for 1 min at 13000 rpm. Lastly, 250 µl RA3 was added to each column, followed by 2 min centrifugation at 13000 rpm. To elute the RNA 60 µl RNase-free water was pipetted to each column and centrifuged at 13000 rpm for 1 min. The samples were stored at -20 °C until further use.

2.3.11. Reverse transcription and qPCR analysis

The concentration of RNA in the samples (for isolation see 2.3.10.) was determined via NanoDrop. For the reverse transcription, 500 ng RNA per sample was used. A master mix was prepared for the reverse transcription, containing 1 µl random primer, 4 µl 5x buffer, 1 µl dNTPs, 1 µl DTT, and 2 µl water per sample. Up to 10 µl RNA was added to the mix and the rest of the volume up to 19 µl was filled with water. The RNA was stretched for 10 min at 70 °C. Afterward, 1 µl Superscript enzyme was added to each sample at room temperature followed by 45 min incubation at 42 °C and subsequently 10 min at 70 °C. At the end of the reverse transcription, the samples were cooled and stored at 4 °C.

For the qPCR analysis following each sample contained 10 µl SybrGreen, 0.5 µl forward primer, 0.5 µl reverse primer, 8 µl water, and 1 µl cDNA. For the negative control, 1µl water was used instead of cDNA. 20 µl from each sample were pipetted in duplicates on a Roche 96-well LightCycler plate. Optimal annealing temperatures were determined for each gene of interest as shown in Table 9.

Table 9: Product size and annealing temperatures of the tested genes.

Gene of interest	***Primer sequence: forward/reverse***	***Size of product***	***Annealing temperature***
MMP1	TCACCAAGGTCTCTGAGGGTCAAGC/ GGATGCCATCAATGTCATCCTGAGC	324 bp	65°C
MMP2	CCCCAAAACGGACAAAGAG/ CTTCAGCACAAACAGGTTGC	88 bp	54°C
MMP3	CAAAACATATTTCTTTGTAGAGAGGACAA/ TTCAGCTATTTGCTTGGGGAAA	91 bp	54°C
MMP9	GAACCAATCTCACCGACAGG/ GCCACCCGAGTGTAACCATA	67 bp	57°C
MMP13	CCAGTCTCCGAGGAGAAACA/ AAAAACAGCTCCGCCGCATCAAC	85 bp	60°C
MMP15	ACGGTCGTTTTGTCTTTTCA/ GTCAGCGGCTGTGGGTAG	85 bp	57°C
TIMP1	TGGATAAACAGGGAAACACTG/ GATGGACTCTTGCACATCAT	142 bp	54°C
b-Actin	CTACGTCGCCCTGGACTTCGAGC/ GATGGAGCCGCCGATCCACACGG	385 bp	54-65°C

The LightCycler was programmed for 45 cycles of amplification. The end results were calculated with LightCycler 96 software and presented as a ratio to the housekeeper (b-actin).

2.3.12. DCFDA-ROS detection

Cells were seeded on a 10 cm dish at density of $5x10^5$ cells per dish in DMEM with or without pyruvate. The cells were cultured for 2 days at 37 °C. Afterward, the dishes were washed 1x with DMEM without FCS. From that point all remaining steps were performed in the dark. The cells were stained with 100 µM DCFDA (from a 10mM stock dissolved in DMSO), dissolved in DMEM without FCS. The staining was performed for 35 min at 37°C in the dark. Some cells were left unstained to be later used as background control. After the end of incubation, the cells were washed 2x with medium without FCS. They were thereafter trypsinized, counted, and seeded on two black clear bottom 96well plates at density $1x10^4$ cells per well in a total volume of 100µl per well. One plate was left as 0J un-irradiated control and the other wan was immediately irradiated with a single dose of 6J UVA to induce ROS. After the irradiation, both plates were incubated for 30 min at 37 °C in the dark. Fluorescence was measured via Varioscan at Ex/Em 485 nm/530 nm.

For the evaluation of the measurements, the values for the unstained cells were subtracted from the DCFDA stained cells to exclude background noise.

2.3.13. DNA extraction

In order to retrieve DNA for subsequent 8-OHdG experiments, UVA treated cells and controls (for standard irradiation protocol see 2.3.5.), cultured on 20 cm petri dishes at a seeding density of $8x10^5$, were trypsinized, centrifuged, and re-suspended in 200 µl/sample PBS. From then on, a QUIamp Mini Kit was used for the isolation (proteinase K, as well as all buffers mentioned, were included in the kit). The DNA extraction was performed as follows.

To each sample, 20 µl proteinase K were added and mixed thoroughly. Afterward, 200 µl from buffer AL were pipetted to the mixture and the samples were mixed by pulse-vortexing for 15 sec. Immediately after that the samples were incubated at 56 °C

for 10 min and briefly centrifuged to remove condensation from the lid. The samples were loaded on the spin columns and centrifuged at 8000 rpm for 1 min. The flow-through was discarded and 500 µl buffer AW1 was added to the columns, followed by centrifugation at 8000 rpm for 1 min. The flow-through was again discarded. 500 µl buffer AW2 was added to each sample and centrifugation at 13000 rpm for 3 min was performed, followed by an additional centrifugation step of 13000 rpm for 1 min to remove the excessive buffer from the column. The flow-through was discarded and the columns were placed in clean collection tubes. 60 µl buffer AE was added to each sample and the columns were incubated for 5 min at room temperature. Subsequently, the samples were centrifuged for 1 min at 8000 rpm and the eluate was stored at -20 °C for further use.

2.3.14. Detection of 8-OHdG as a sign of UVA-induced DNA damage

The method used to detect oxidative DNA damage in UVA-irradiated cells was based on the OxiSelect™ ELISA Kit. This kit is a competitive enzyme immunoassay for the detection and quantitation of 8-OHdG in DNA samples.

To prepare for the assay the stock substrate-solution was first diluted to a working concentration of 1 µg/mL in PBS (dilution 1:1000). Afterward, the provided multiwell plate was coated with 100µl working solution per well and incubated overnight at 4 °C. At the end of the incubation, the 8-OHdG coating solution was removed and washed 1x with dH2O. The plate was blotted on some paper towels to remove excess fluid and 200µl of Assay Diluent was added to each well. The plate was blocked for 1h at room temperature and subsequently transferred to 4°C until further use.

Sample preparation was conducted according to the following protocol. Sample DNA concentration was measured by NanoDrop (for DNA extraction see 2.3.13.). The concentration was then adjusted to a total of 20µg DNA in 83µl (dilution of the samples was performed with PCR-grade water). The DNA samples were incubated at 95 °C for 5 min and rapidly chilled on ice to stretch and convert the DNA into single strands. To digest the DNA into nucleosides 1.5µl/sample nuclease P1 (earlier reconstituted in P1 buffer at a stock concentration of 3.36 U/µl) and 9.5µl/sample 200mM sodium acetate were added. The samples were incubated for 2h at 37 °C. Subsequently, 1µl/sample alkaline phosphatase (earlier reconstituted in PhosA buffer at a stock concentration of 10.1805 U/µl) and 15µl from the 0.69M Tris HCl buffer (pH 7.5) and further incubated

for 1h at 37 °C. At the end of the incubation, the samples were centrifuged for 5 min at 8000 rpm and the supernatant was collected for further use.

The assay diluent was removed from the ELISA plate and 50µl per well from the 8-OHdG standard (for concentration and preparation see Table 10) and unknown samples were pipetted in duplicates.

Table 10: Pipetting plan and concentrations of 8-OHdG standard

Standard	**8-OHdG Standard (µl)**	**Assay Diluent (µl)**	**8-OHdG (ng/ml)**
1	10	990	20
2	500 of 1	500	10
3	500 of 2	500	5
4	500 of 3	500	2,5
5	500 of 4	500	1.25
6	500 of 5	500	0.625
7	500 of 6	500	0.313
8	500 of 7	500	0.156
9	500 of 8	500	0.078
10	0	500	0

The plate was incubated for 10 min at room temperature on an orbital shaker. 50 µl of the diluted anti-8-OHdG antibody (dilution 1:500) were added to each well and the plate was further incubated at room temperature for 1h on an orbital shaker. At the end of incubation, the plate was blotted on some paper towels to remove excess fluid and washed 3x with 200µl/well washing solution (dilution 1:10). 100 µl of the secondary antibody-enzyme conjugate (dilution 1:1000) were added to all wells, followed by 1h incubation on an orbital shaker. The plate was washed again 3x with 200µl/well washing solution. 100µl per well from the substrate solution was added and incubated for approximately 1 min, after which the reaction was stopped by adding 100µl stop solution into each well. The absorbance of the microwell plate was measured with a Varioscan Flash plate reader at 450 nm.

For data analysis, the values from the standard were plotted in GraphPad Prism and the unknown values for the samples were extrapolated from the resulting curve.

2.3.15. NBTC-vitality-test

Nitroblue tetrazolium chloride (NBTC) is a redox indicator. It is reduced by cell-bound NADH-diaphorase that has activity only in viable cells. This leads to the production of blue granular precipitate in living cells that can be microscopically distinguished from unstained dead cells. The NBTC staining of mouse skin explant was performed as follows.

After irradiation (for protocol see 2.3.5.), the murine skin punches were shock-frozen in liquid nitrogen. The samples were then embedded in tissue-tek and cut via cryotome 8 µm thick slices. To perform the vitality staining a master mix containing 1 ml NADH (stock 2.5 mg/ml), 2.5ml NBTC (stock 2 mg/ml), 1 ml PBS (pH 7.4) and 0.5 ml ringer solution. From the master mix, 60 µl was pipetted on each section and the sections were incubated for 15 min at room temperature. Afterward, the reaction was stopped in PBS and the samples were covered using Aquatex mounting medium. The resulting staining was evaluated microscopically via Axiostar Plus Microscope and images were taken using AxioCam camera coupled with Axiovision software.

2.3.16. Two in one cell count and viability test

To determine the number of cells, as well as their viability, a LUNA-FL Dual Fluorescence Cell Counter in combination with Acridine orange/Propidium iodide (AO/PI) staining was used. Acridine orange (AO) and propidium iodide (PI) are nucleic acid binding dyes. AO can permeate both live and dead cells and intercalates with DNA, generating green fluorescence. PI can only enter dead cells that have poor membrane integrity. It then generates red fluorescence in all dead nucleated cells. In addition, in cells containing both AO and PI the green fluorescence is quenched and the cells still fluorescent red. With this, all live nucleated cells fluoresce green and all dead nucleated cells fluoresce red, allowing for a clear distinction between viable and non-viable populations.

To perform the actual cell-count 18 µl of cell suspension were mixed with 2 µl AO/PI dye. From this mixture, 10 µl was pipetted on LUNA cell counting slides and measured in fluorescence modus with LUNA-FL.

3. Results

3.1. UVA-irradiation induces increase glucose consumption and lactate production in a variety of non-malignant skin cells

Since previously published data (53) show that UVA-irradiation changes the metabolic profile of human melanoma cells, it is important to elaborate on the metabolic changes in the cells surrounding the tumor – the tumor stroma, and more precisely keratinocytes, melanocytes, and fibroblasts.

As mentioned previously, fibroblasts and keratinocytes, as part of the tumor-surrounding tissue, play important role in immune modulation and skin-homeostasis. These cells, although not malignant themselves per se, can act together with cancer cells and produce substances promoting tumor spread and metastasis (110, 111).

To better understand what metabolic changes occur in non-malignant cells after UVA-irradiation, healthy skin cells (keratinocytes, melanocytes, and fibroblasts) from both human and murine origin were irradiated with 6J/cm^2 UVA for four days as described in 2.3.5. Changes in glucose and lactate metabolism were measured.

3.1.1. Keratinocytes

The first important cell-subset of the skin is the keratinocyte population. They, together with the melanocytes, build the upper skin layer, the epidermis, and are the first ones to receive damage from UVA-radiation.

3.1.1.1. Murine keratinocytes

Murine keratinocytes (mKera) were isolated from 129 Sv/Ev WT mouse (tail) and re-suspended in ATCC Keratinocyte medium (1g/L Glucose, 0.52mM pyruvate, 6mM L-glutamine) in accordance with 2.3.3. Standard 4d irradiation was performed after culturing the keratinocytes for five days on 6-well-plates.

Before commencing with irradiation, a test plate was trypsinized and counted to determine the number of viable cells per well in the experiment. From the three independent experiments, the number of cells per well was approximately 3.6x10^4.

Irradiation with UVA resulted in growth retardation as seen in Fig. 11. The cells showed no major morphologic changes post-irradiation. The end number of cells in the irradiated samples was half of the one in the un-irradiated counterparts (see Fig. 11 B).

The irradiated keratinocytes showed less viability than the un-irradiated samples. According to the statistical analysis performed on the samples, the 4.3 % difference in viability between the two irradiation conditions was significant. Its biological relevance, however, could be seen as disputable. The overall viability for both irradiated and un-irradiated samples did not fall below 85 %. The number of cells did not fall below the level at the beginning of the experiment.

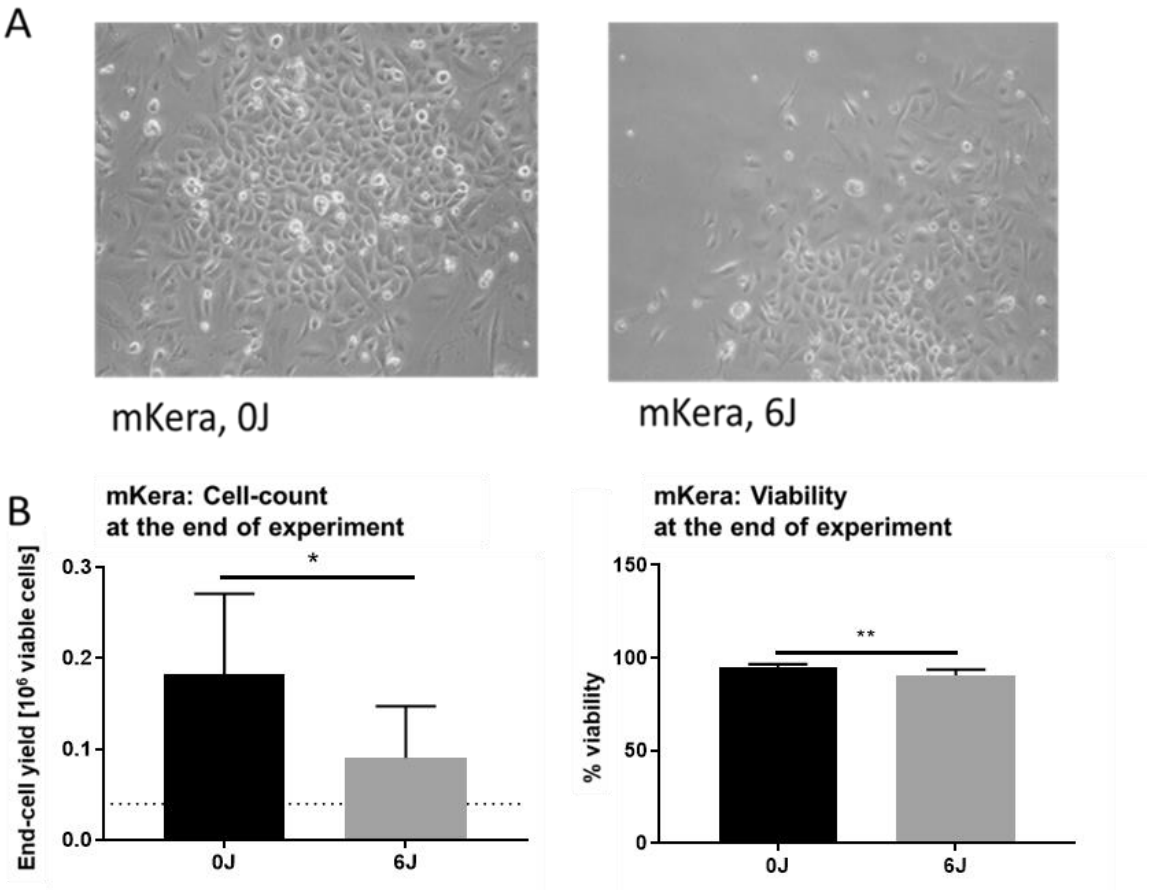

Fig. 11: (A) Cell morphology and viability of mouse keratinocytes after 4d irradiation (magnification 20x). No major morphological changes could be detected. Dotted line indicates the amount of cells seeded. (n=3, Statistical analysis Student's t-test. For significances: (ns) P > 0.05; (*) P < 0.05; (**) P < 0.005).

The results of the colorimetric measurements of glucose consumption and lactate production are shown in Fig. 12. UVA irradiation increases the consumption of glucose and the production of lactate in irradiated murine keratinocytes, compared to un-irradiated control.

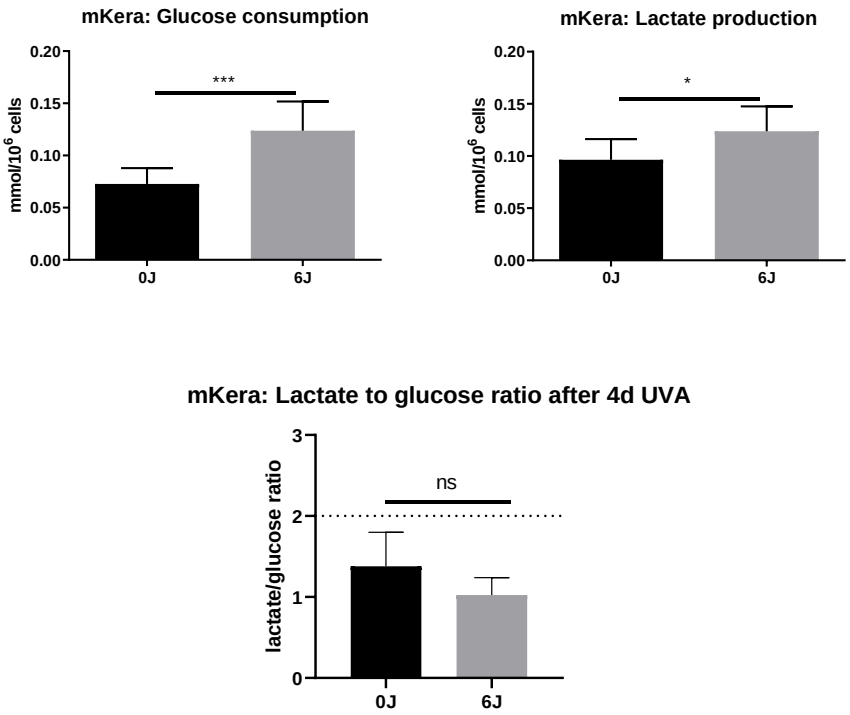

Fig. 12: Metabolic data (measured from supernatant) of mouse keratinocytes after 4d irradiation. UVA irradiation increases glucose consumption and lactate production in healthy skin cells similar to the metabolic changes detected human and murine fibroblast cells. The glucose to lactate ratio showed no significant changes between irradiated and un-irradiated cells with ratios of 1.3 for the 0J and 1 for the 6J samples. Dash-line represents an ideal glucose to lactate conversion of 2 associated with aerobic glycolysis. (n=3, Statistical analysis Student's t-test. For significances: (ns) P > 0.05; (*) P < 0.05; (**) P < 0.005; (***) P < 0.0005; (****) P < 0.0001).

In the case of un-irradiated cells, 1mol glucose is converted to approximately 1.4 mol lactate. On the other hand, although consuming more glucose, the irradiated cells converted it to lactate at a ratio of approximately 1mol glucose to 1mol lactate (Fig. 12 and Table 12). Although un-irradiated cells showed a clear tendency of higher conversion ratios of 1.4 compared to a ratio of 1 in the irradiated samples, the difference between both irradiation conditions was not statistically significant.

3.1.1.2. Human keratinocytes

Adult human keratinocytes (HEKa) were purchased from Gibco and cultured in a special Gibco Keratinocyte medium. Cells were seeded on 6-well plates and standard irradiation protocol was performed according to 2.3.5.

As shown in Fig. 13 A, the irradiation leads to slight rounding of the cells and an increase in size compared to un-irradiated controls. Growth retardation could also be observed. The number of viable cells at the end of irradiation was half of the one in the untreated control. There is also a significant decrease in cell viability after irradiation with a 5.4 % reduction in viability when compared to un-irradiated samples. Nevertheless, the cells still proliferated slowly and did not fall below the number initially seeded on the plates.

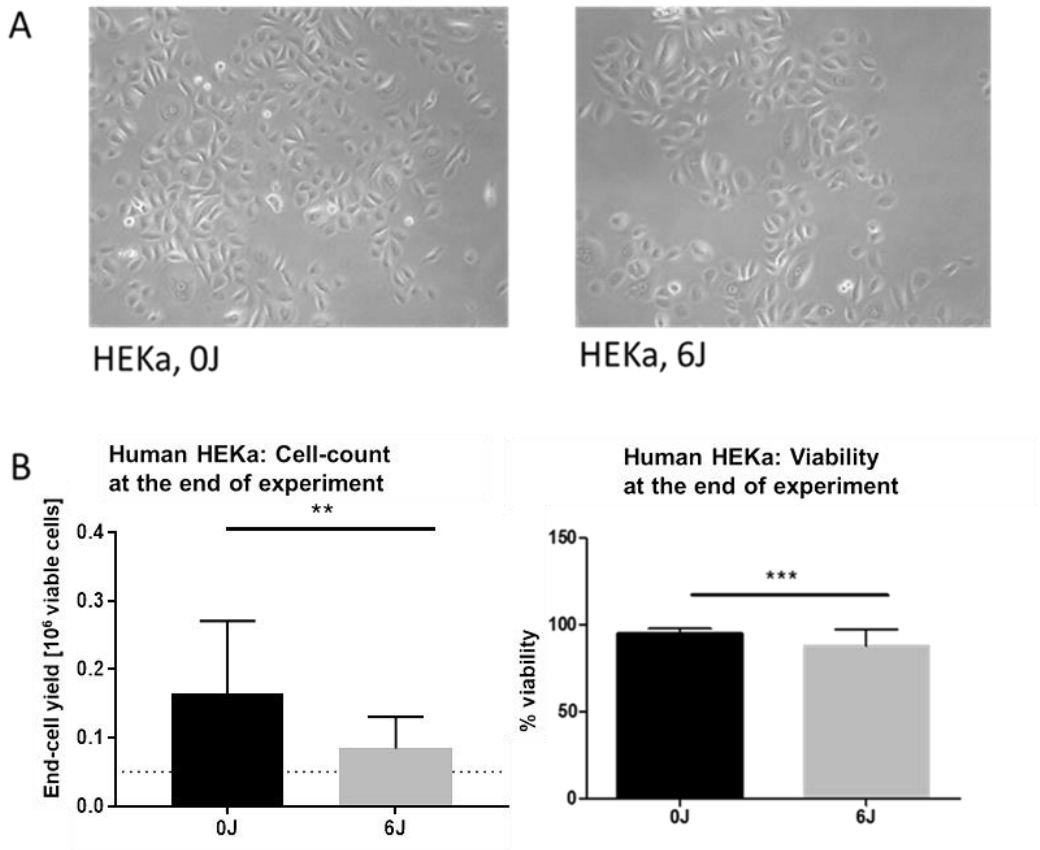

Fig. 13 (A*) Cell morphology and viability of human adult keratinocytes after 4d irradiation (magnification 20x). Cells tend to become rounder in shape after UVA application. (B) cell count and viability at the end of irradiation. There is a decrease in the number of viable cells by 50 % after UVA treatment when compared to un-irradiated controls. The overall cell viability also seems to decrease with irradiation. . Dotted line indicates the amount of cells seeded. (n=7, Statistical analysis Student's t-test. For significances: (***) P < 0.0005).*

UVA irradiation increases the consumption of glucose and the production of lactate in irradiated human keratinocytes, compared to un-irradiated Fig. 14. The conversion of glucose to lactate is close to the one observed in murine keratinocytes with a lactate-to-glucose ratio of 1.6 for un-irradiated and 1.5 for irradiated cells (see

Fig. 12). Similar to murine keratinocytes, there was no significant difference in the lactate-to-glucose ratio between irradiated and un-irradiated samples.

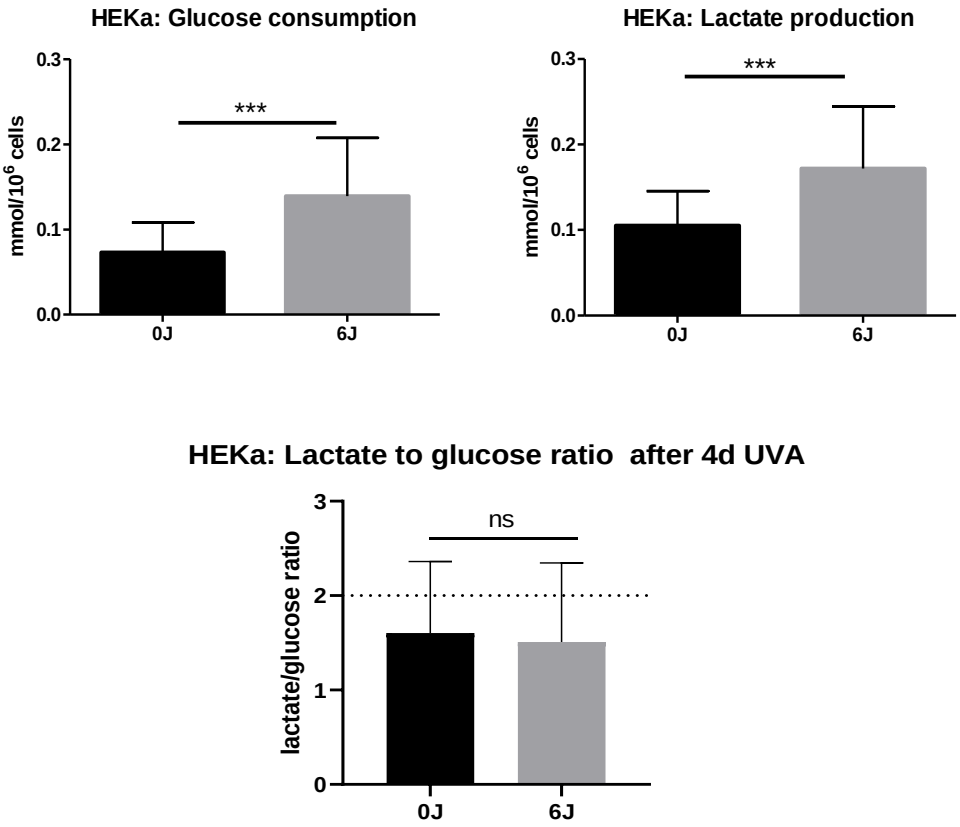

Fig. 14: Metabolic data (measured from supernatant) of human adult keratinocytes after 4d irradiation. UVA irradiation increases glucose consumption and lactate production in healthy skin cells similar to the metabolic changes detected in human and murine fibroblasts and murine keratinocytes. The lactate-to-glucose ratio showed no significant changes between irradiated and un-irradiated cells with ratios of 1.4 for both the 0J and 6J samples. Dash-line represents an ideal glucose to lactate conversion of 2 associated with aerobic glycolysis. (n=7, Statistical analysis Student's t-test. For significances: (ns) P > 0.05; (***) P < 0.0005).

3.1.2. Melanocytes

As mentioned previously, melanocytes are responsible for melanin production and protecting the skin from solar irradiation. Earlier research has established melanocytes as possible precursors of melanoma (112, 113). Besides representing a possible increase in melanin production as a defence mechanism against UVA irradiation, metabolic changes in melanocytes occurring after the UVA treatment could potentially be seen as indicators for pre-malignant reprogramming of the cell's

biomass-synthesis and energy balance. This point is important as changes in energy metabolism have been recognized as one of the hallmarks of cancer (114).

Adult human melanocytes (HEMa) were purchased from ATCC and cultured in ATCC-Melanocyte medium (1g/L Glucose, 0,52 mM pyruvate, 6mM L-glutamine). The cells were seeded at a density of approximately $2x10^4$ cells/well on a 6-well-plate. The cells were left to grow for 3d before the irradiation was started. Afterward, the irradiation was performed as described in 2.3.5.

As seen in Fig. 15 A UVA irradiation did not result in any distinguishable morphologic changes. There is also no significant difference in the end number of viable cells after irradiation, although there is a tendency of fewer cells present after UVA treatment (Fig. 15 B). There were also no significant changes in overall viability between treated and untreated samples.

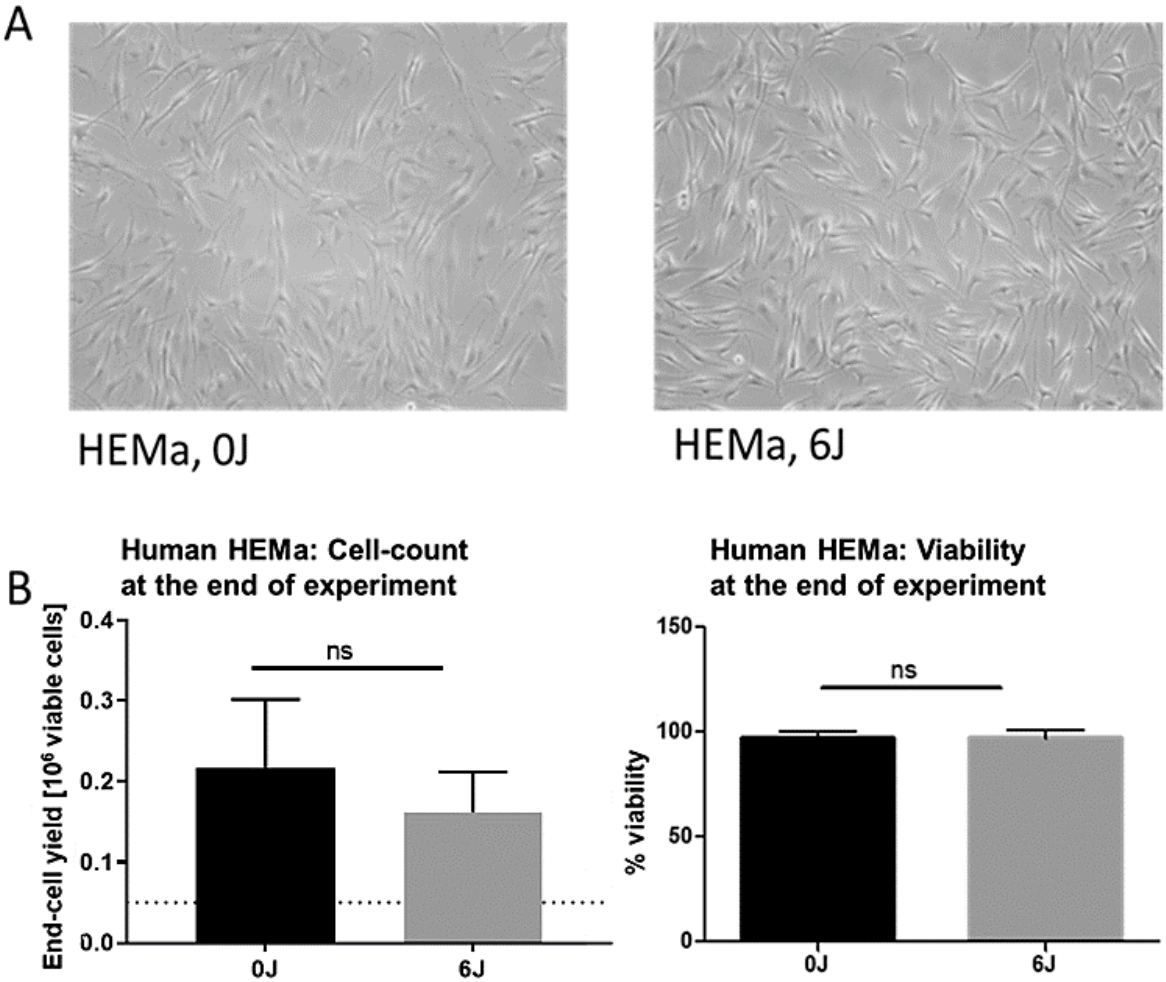

Fig. 15: *Cell morphology and viability of adult human melanocytes after 4d irradiation (magnification 20x). No morphologic changes were visible after irradiation. Dotted line indicates the amount of cells seeded. (n=3, Statistical analysis Student's t-test. For significances: (ns) P > 0.05).*

As seen in Fig. 16, UVA irradiation results in increased glucose consumption and lactate production compared to untreated controls. The conversion of glucose to lactate is not complete. The amount of consumed glucose is more than the lactate produced at the end of treatment with a lactate to glucose ratio of 0.8 for both irradiated and un-irradiated samples. Like both human and murine keratinocyte samples, human melanocytes also showed no significant difference in the lactate-to-glucose ratios between UVA-treated and untreated samples.

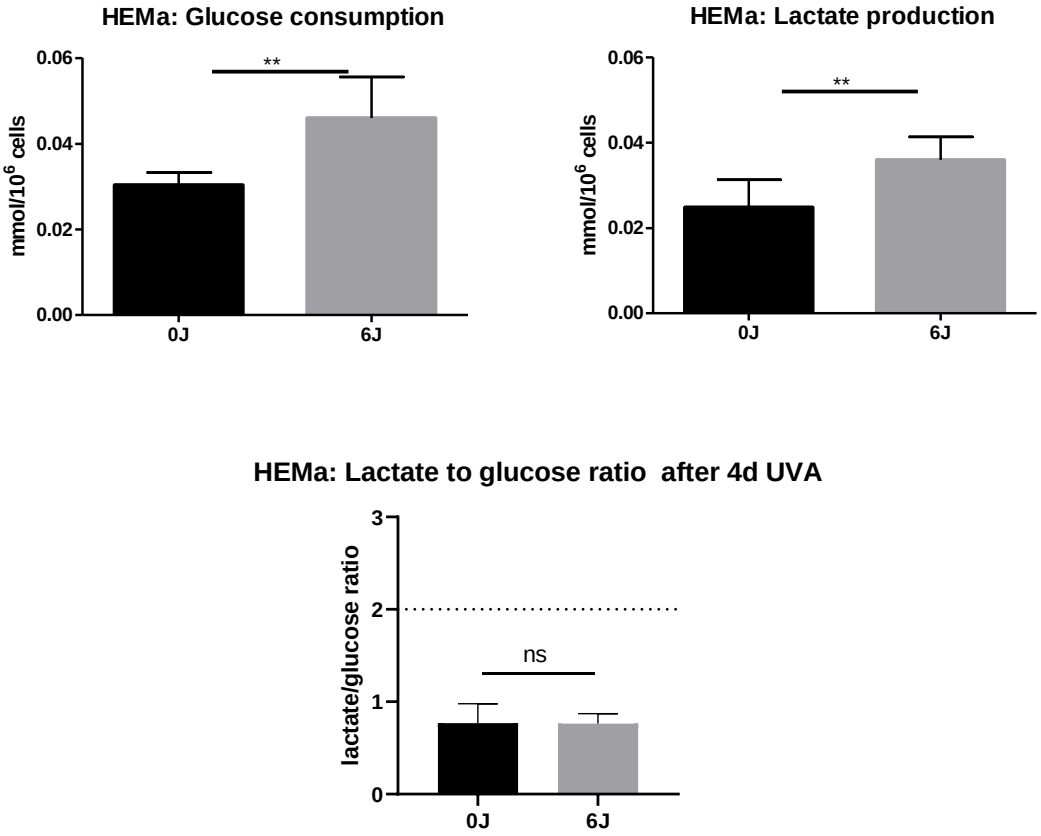

Fig. 16: *Metabolic data (measured from supernatant) of adult human melanocytes after 4d irradiation. UVA irradiation increases glucose consumption and lactate production in healthy skin cells similar to the metabolic changes in both human and murine fibroblasts and keratinocytes. The lactate-to-glucose ratio showed no significant changes between irradiated and un-irradiated cells with ratios of 0.8 for both the 0J and the 6J samples. Dash-line represents an ideal glucose to lactate conversion of 2 associated with aerobic glycolysis. (n=3, Statistical analysis Student's t-test. For significances: (ns) P > 0.05; (**) P < 0.005).*

3.1.3. Fibroblasts

Fibroblasts are the major component of the dermis and the tumor stroma. Furthermore, they are responsible for the correct function and stability of the extracellular matrix (ECM). It has been shown that UV-radiation influences the morphology of fibroblasts and their ability to produce collagen, thus influencing the integrity and elasticity of the ECM and thus the skin (115). Additionally, UV-radiation increases the production of matrix metalloproteinases in fibroblasts. This UV-induced production of matrix metalloproteinases can re-model the ECM and lead to skin photoaging or it can increase tumor cell migration and invasion.

3.1.3.1. Murine fibroblasts

After irradiating murine NIH 3T3 fibroblasts for four days with 6J/cm^2 UVA, the cells showed obvious morphologic changes. As shown in Fig. 17, UVA irradiation resulted in a decrease in cell number, due to either apoptosis or dis-regulation in cell proliferation.

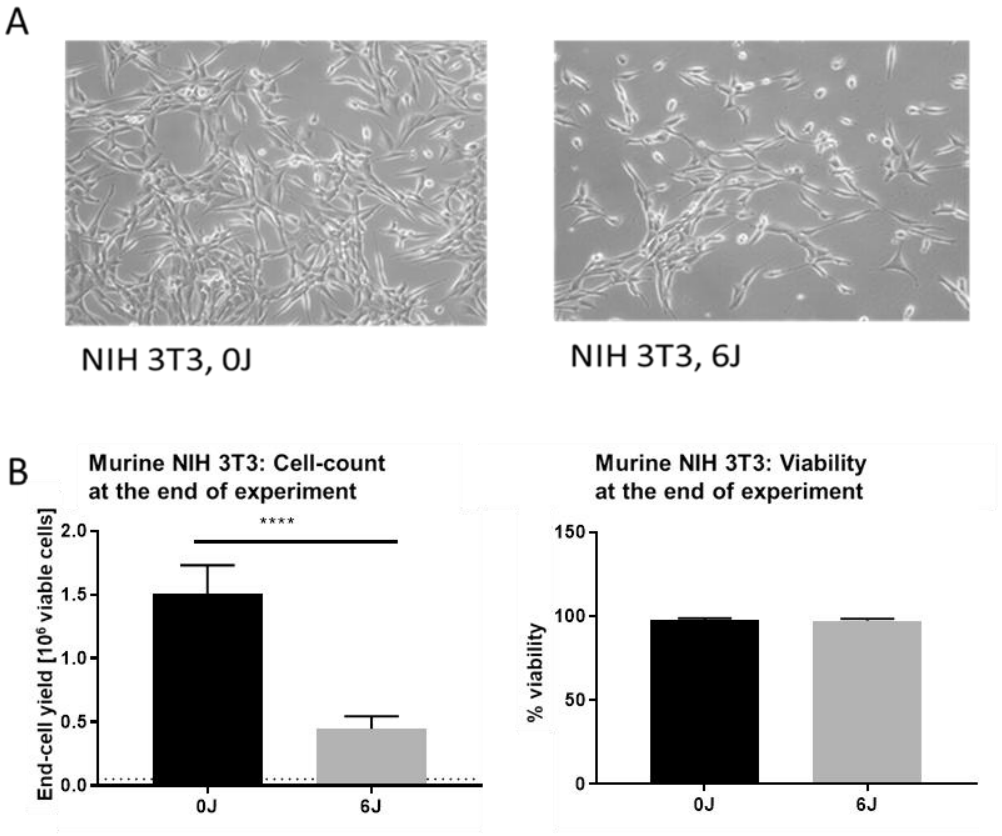

Fig. 17: (A) Cell morphology of murine fibroblasts NIH 3T3 after 4d irradiation and (B) Number of viable cells and overall cell viability at the end of irradiation. Loss of membrane-protrusions and rounding of

the cellular body occur after repeated cycles of UVA irradiation (A) (magnification 20x). The irradiated cell population is only a third of their non-irradiated counterparts but both treatments show the same levels of overall viability (B). Dotted line indicates the amount of cells seeded. (The images are representative of four independent experiments (*n=4), Statistical analysis Student's t-test. For significances: (****) P < 0.0001).*

The cell culture medium of both irradiated and non-irradiated samples was unperturbed and showed no dead and floating cells. Still, cell death could not be completely excluded, since the rounded cells visible in Fig. 17 A after irradiation could be early apoptotic cells that still had not detached. Therefore, at the end of irradiation, the cells were collected and counted using AO/PI dye in accordance with the method described in 2.3.16. As evident from the results in Fig. 17 B after four days of UVA irradiation, the total number of cells in the treated samples is only about a third of the cell amount in un-irradiated samples. Still, the cells irradiated with UVA have no significant difference in viability when compared with their untreated counterparts. In addition to this, the cells continue to proliferate since the number of cells at the end of the experiment does not fall below the number of cells initially plated ($5x10^4$ cells per well), but on the contrary increases. This signals the possibility of retardation in cell proliferation rather than apoptosis as the main reason for the difference in the end number of cells between irradiated and un-irradiated samples.

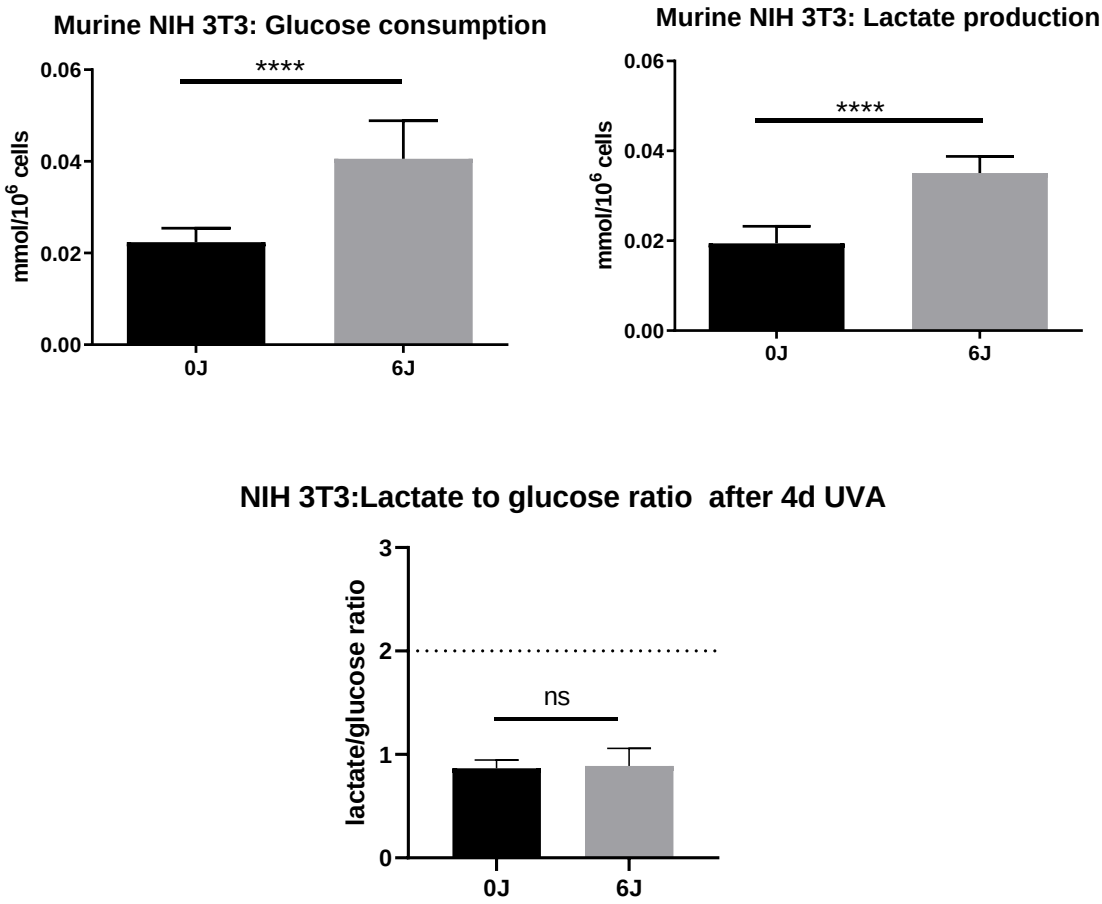

Fig. 18: Metabolic data (measured from supernatant) of murine fibroblasts NIH 3T3 after 4d irradiation.UVA irradiation increases glucose consumption and lactate production in healthy skin cells similar to the metabolic changes detected in human melanoma cells(53). The lactate-to-glucose ratio showed no significant changes between irradiated and un-irradiated cells with ratios of 0.9 for both the 0J and the 6J samples. Dash-line represents an ideal glucose to lactate conversion of 2 associated with aerobic glycolysis. (n=4, Statistical analysis Student's t-test. For significances: (ns) P > 0.05; (****) P < 0.0001).

After the irradiation, the supernatant of the cells was collected and a colorimetric determination of the glucose and lactate concentrations was performed in accordance with the protocol described in 2.3.6. and 2.3.7. The number of viable cells was used to normalize the photometrically acquired results to compensate for the already mentioned discrepancy in the end number of cells between treated and untreated samples. As seen in Fig. 18, UVA irradiation increases the consumption of glucose and the production of lactate in irradiated fibroblasts, compared to un-irradiated control. But only part of the consumed glucose is metabolized to lactate, as glycolysis should have resulted in approximately 1mol glucose yielding 2mol lactate (116). In the case of NIH 3T3, the lactate-to-glucose ratio for both irradiated and un-irradiated samples

was around 0.9. These results indicate that fibroblasts use glucose for other metabolic pathways, for example respiration, and not only glycolysis.

3.1.3.2. Human fibroblasts

Besides murine fibroblasts, human skin fibroblasts were also irradiated with UVA in accordance with the standard irradiation protocol of 6J/cm^2 UVA three times per day for the duration of four days (see 2.3.5.). The WT01 fibroblasts were foreskin-isolates provided by Kamenisch et al. (107, 117). The Re5 fibroblasts were isolated from donor skin in accordance with the protocol in 2.3.2.

Compared to the murine fibroblasts both WT01 and Re5 showed slightly more elongated morphology after irradiation, especially Re5, unlike the rounded shapes observed in murine cells (Fig. 17a). Still, similar to the murine samples, there are fewer cells after irradiation. A slight retardation in proliferation could also be observed, similar to the murine cells.

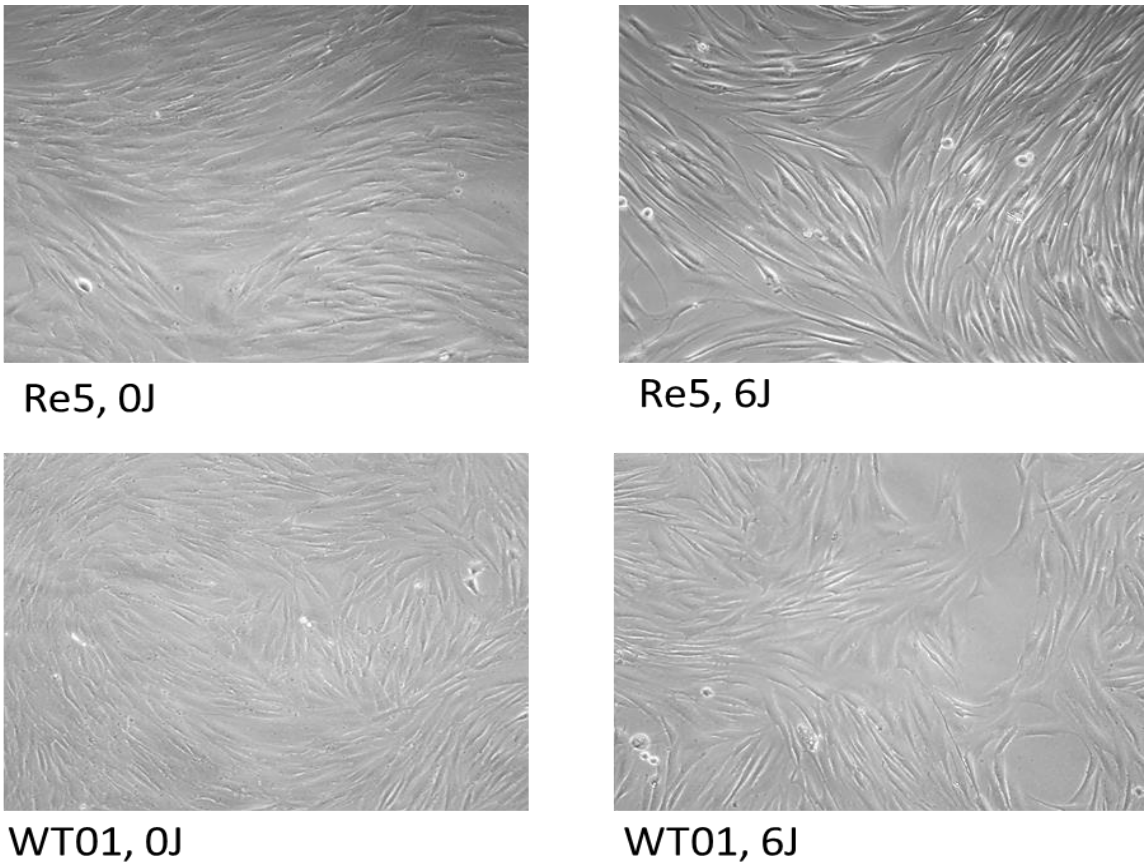

Fig. 19: Cell morphology of human fibroblast Re5 and WT01 after 4d irradiation(magnification 20x*). No differences in cell morphology in UVA irradiated cells compared to untreated cells could be detected. The images are representative of three independent experiments (n=3).*

Similar to NIH 3T3, human fibroblasts retain their viability post-irradiation (Fig. 20). In contrast to their murine counterparts, however, the effect of radiation was less pronounced in human fibroblasts but still the number of cells at the end of the experiment was 50% reduced compared to the untreated controls.

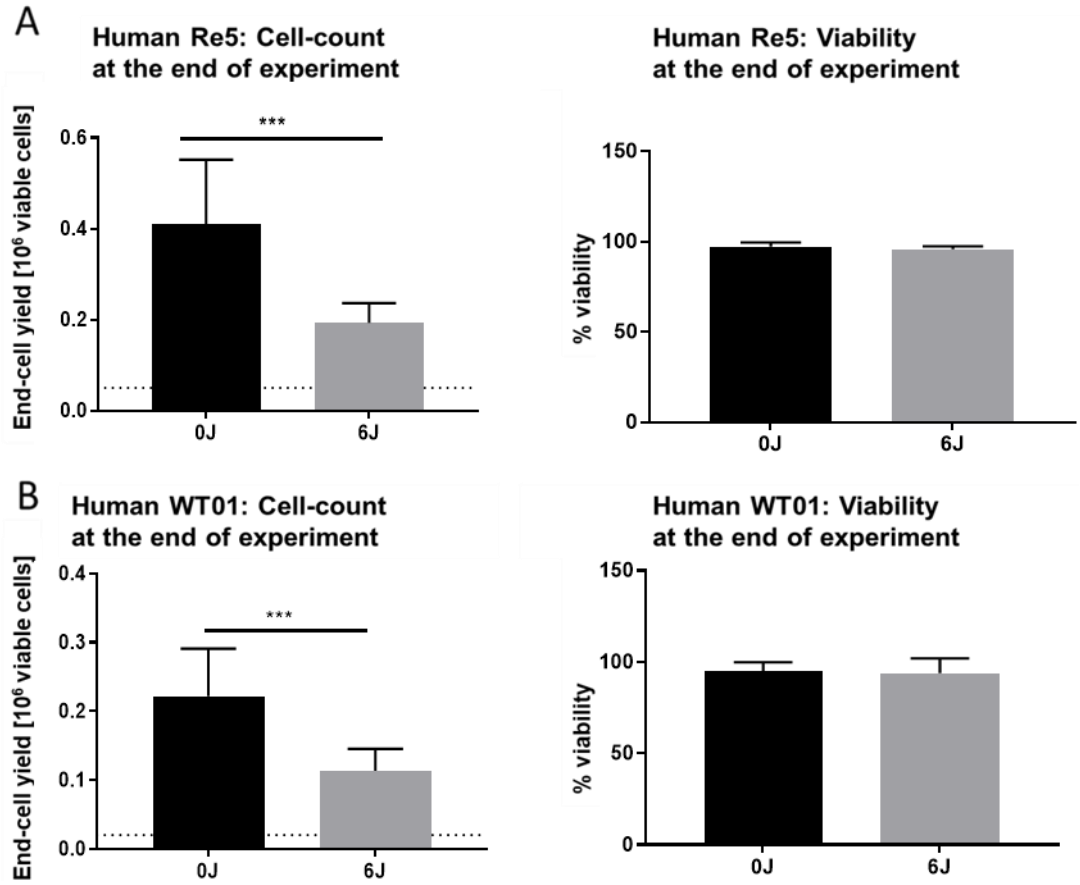

Fig. 20: Number of viable cells and overall cell viability at the end of irradiation of human fibroblasts Re5 (A) and WT01 (B). The irradiated cell population is only half of their non-irradiated counterparts but both treatments show the same levels of overall viability. Similar to Re5, the irradiated cell population is only half of the number of cells in the un-irradiated samples but both treatments show the same levels of overall viability. (n=3, Statistical analysis Student's t-test. For significances: (***) P < 0.0005; (****) P < 0.0001).

From the data, it is evident that UVA increases the consumption of glucose and the production of lactate in irradiated fibroblasts (Fig. 21), compared to un-irradiated control. However, the conversion of glucose to lactate in Re5 cells is almost complete, yielding almost 2mol lactate for 1mol glucose. This indicates glycolysis as a major metabolic pathway activated after UVA-irradiation.

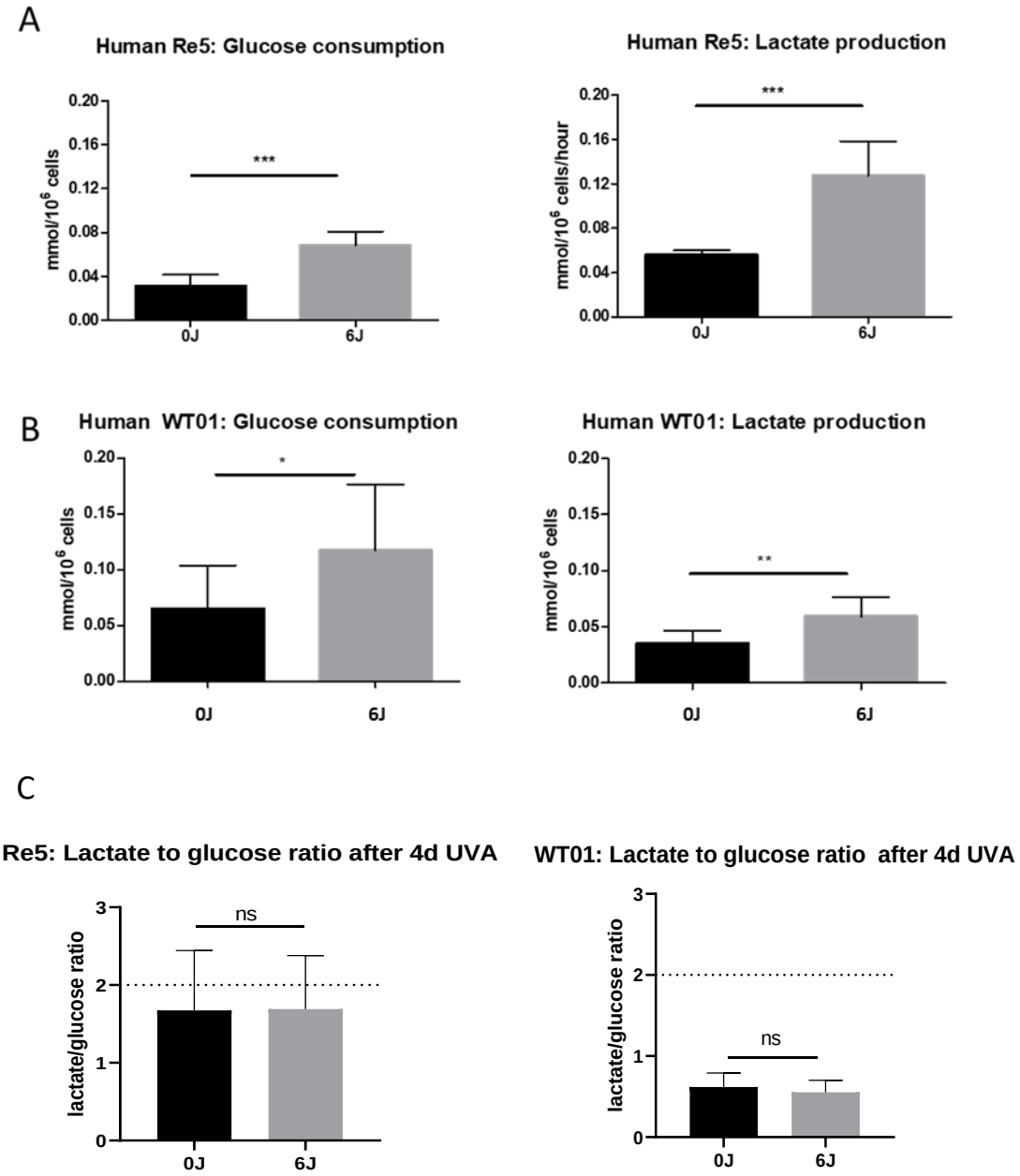

Fig. 21: (A) Metabolic data (measured from supernatant) of human fibroblast Re5 after 4d irradiation. UVA irradiation increases glucose consumption and lactate production in healthy skin cells similar to the metabolic changes previously detected in human melanoma cells (53). There is an almost complete conversion of glucose to lactate in the irradiated samples. (B) Cell metabolic data (measured from supernatant) of human fibroblast WT01 after 4d irradiation. UVA irradiation increases glucose consumption and lactate production in healthy skin cells similar to the metabolic changes detected in Re5. (C) The lactate-to-glucose ratio for both WT01 and Re5 showed no significant difference between irradiated and un-irradiated samples. The glucose conversion to lactate in WT01 was incomplete with a lactate to glucose ratio of 0.5. Re5, on the other hand, showed a conversion of glucose to lactate with a ratio of approximately 1.5. Dash-line represents an ideal glucose to lactate conversion of 2 associated with aerobic glycolysis. (n=3, Statistical analysis Student's t-test. For significances: (ns) P > 0.05; (*) P < 0.05; (**) P < 0.005; (***) P < 0.0005).

Interestingly, WT01 shows incomplete metabolization of glucose to lactate, as there is less lactate produced compared to the consumed glucose, with a conversion ratio of glucose to lactate of 0.6. In addition to that, WT01 cells seem to have a higher consumption of glucose in their un-irradiated state compared to Re5. At the same time, despite their higher consumption levels of glucose (double than what was observed in Re5), the lactate-to-glucose ratio of WT01 is less than the ratio in Re5. Re5 had a lactate-to-glucose ratio of 1.7 for both irradiated and un-irradiated samples. Despite these distinctly different metabolic profiles, both human fibroblast lines showed no significant differences in the lactate-to-glucose ratios between irradiated and un-irradiated samples.

The differences in proliferation speed for all irradiated human and murine cells are summarized in Table 11. In general, all irradiated calls showed proliferation retardation to some degree when compared to un-irradiated controls. HEMa and WT01 cells showed the least reaction to irradiation from all cells, with a proliferation-retardation ratio of 1.3. The murine NIH 3T3 showed the fastest proliferation rate of all cells. Re5 was the cell line that was influenced by UVA irradiation the most, having its doubling time increased by a factor of 2 compared to the untreated controls.

Table 11: Doubling times (in hours) and doubling time ratios of irradiated and un-irradiated cells.

Cells	**Doubling time [h] 0J**	**Doubling time [h] 6J**	**6J/0J ratio**
mKera	45, +/- 11	118, +/- 27	1.9
HEKa	45, +/-10	77, +/- 26	1.7
HEMa	61, +/- 12	77, +/-17	1.3
NIH 3T3	21, +/- 1	33, +/- 4	1.6
WT01	42, +/- 10	59, +/- 20	1.3
Re5	50, +/- 4	102, +/- 14	2

A summary of the metabolic changes for all tasted skin cells is depicted in Table 12. The correlation between glucose consumption and lactate production before and after irradiation is represented by the lactate-to-glucose ratio. A ratio over 1 indicates higher lactate production than glucose consumption. Ratios below 1 show that cells consume more glucose than what is invested in lactate production. A ratio of 2 would theoretically depict a perfect glucose to lactate conversion since stoichiometrically 1mol glucose could yield a maximum of 2mol lactate.

From all tested cells, HEKa, mKera, and Re5 showed a lactate-to-glucose ratio over 1. In the case of mKera und HEKa, UVA irradiation resulted in decreasing the

ratio compared to the untreated samples, indicating a reduction in lactate release after UVA treatment. However, this decrease was not statistically significant.

HEMa, NIH 3T3, and WT01 had lactate-to-glucose ratios under 1. There were no major changes in the ratios between the irradiated and un-irradiated samples for all tested cells.

Table 12: Lactate to glucose ratio in non-malignant skin cells before and after UVA treatment

Cells	**Lactate/Glucose 0J**	**Lactate/Glucose 6J**
mKera	1.4	1.0
HEKa	1.6	1.5
HEMa	0.8	0.8
NIH 3T3	0.9	0.9
WT01	0.6	0.6
Re5	1.7	1.7

Since Re5 cells showed the greatest proliferation retardation after irradiation, were easy to cultivate and showed very high lactate to glucose ratios before and after irradiation, they were chosen as the cell type for all subsequent experiments.

3.2. Medium pyruvate and its influence on fibroblast morphology and proliferation

As seen in 3.1, UVA induces changes in the glucose metabolism of non-malignant cells. However, it must be noted that cell culture conditions can hardly be compared to the physiological environment of the cells in human tissues. This is not limited only to the monolayer growth conditions on culturing plates but also encompasses the additives supplemented to the medium to facilitate cell proliferation.

One such additive is pyruvate. Being present at concentrations of 50-120 µM in human blood (118), pyruvate is supplemented to cell culture mediums, including DMEM, in concentrations several times higher than the physiological level. Since pyruvate can act as an additional source of carbon for the cells besides glucose (119), its presence in the culture medium might influence and falsify the acquired metabolic data presented in this work before and after irradiation. Furthermore, there have been

indications that pyruvate has antioxidant properties (85), which could also influence the reaction of the tested cells towards ROS-inducing UVA-irradiation.

In order to keep the cells in an environment as close as possible to their milieu, human fibroblasts Re5 were cultured in medium without pyruvate. Their viability, morphology, and proliferation speed were tested to ensure that the subtraction of pyruvate has no major detrimental effects on the cells.

As shown in Fig. 22, the morphology of the cells remained unchanged by the lack of pyruvate compared to control cells cultured in complete DMEM containing 1mM pyruvate. Only the treatment with UVA radiation had influence on cell morphology, leading to slightly more elongated shapes compared to un-irradiated cells, but the elongation was not influenced by the presence or absence of pyruvate in the medium.

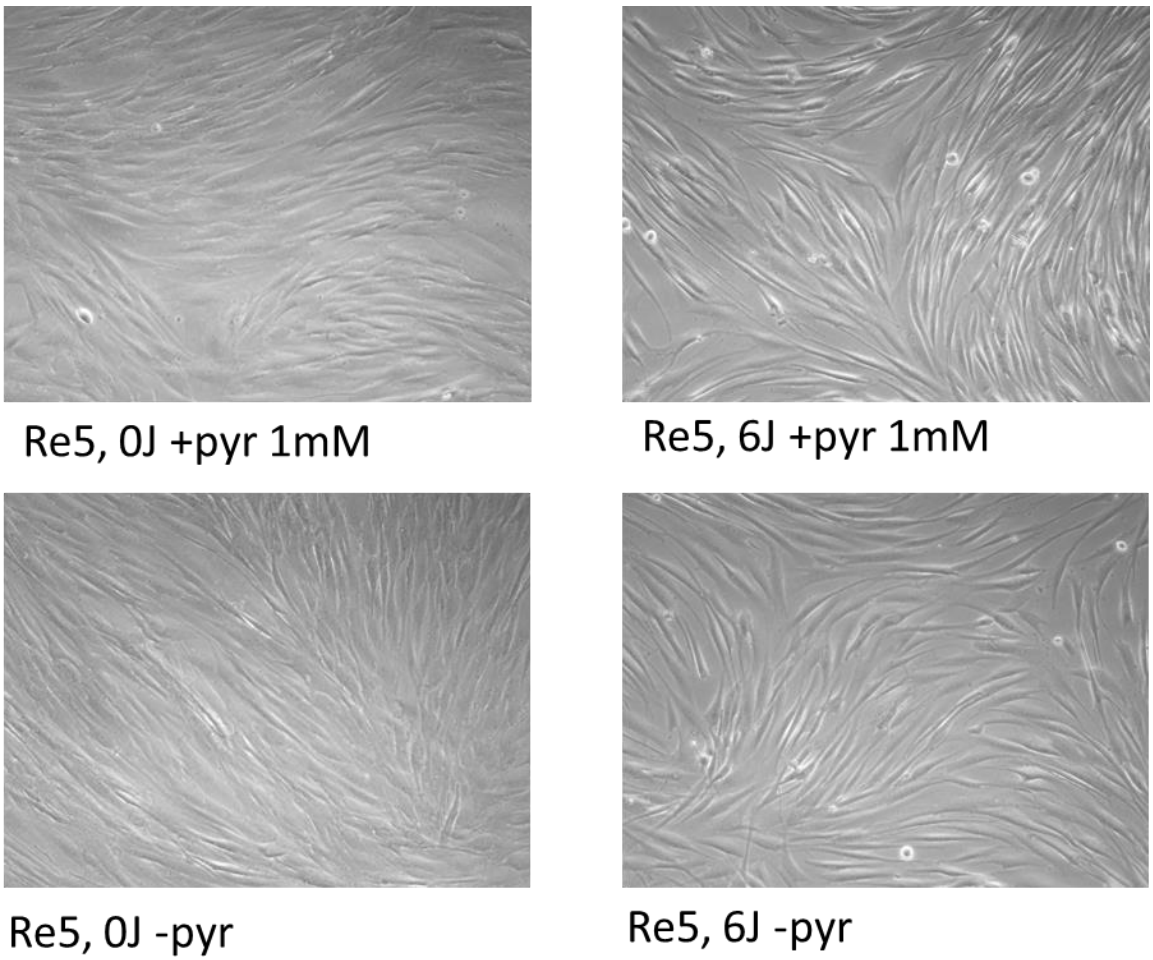

Fig. 22: Cell morphology of human fibroblasts Re5 after 4d irradiation with and without pyruvate in the culturing medium.

In regards to the cell viability, as seen in Fig. 23, pyruvate had again no influence on the cells independent of irradiation status.

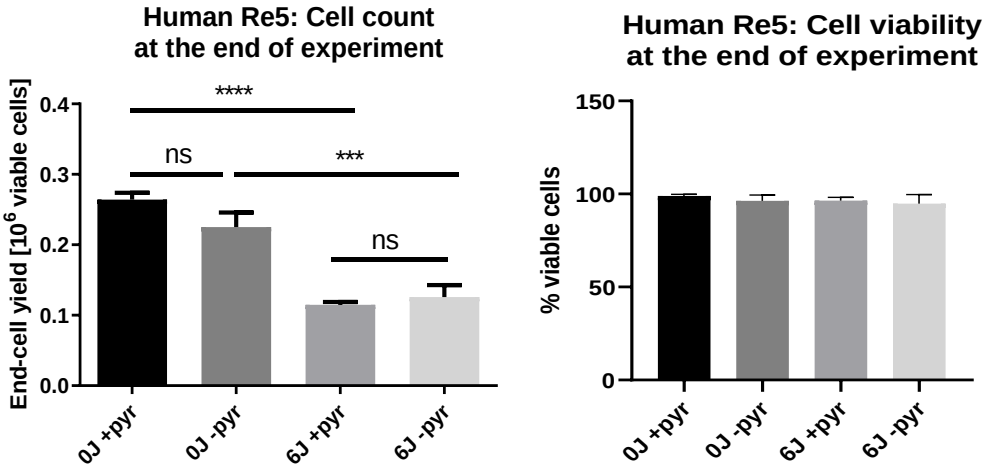

Fig. 23: Number of viable cells at the end of 4d UVA irradiation – comparison of cells cultured in DMEM containing 1mM or 0mM pyruvate. There are clear differences in the number of viable cells at the end of the experiment between irradiated and un-irradiated samples. There are no significant differences in the end number of cells or viability between different pyruvate treatments that have been similarly irradiated.

Table 13 shows the doubling times for Re5 fibroblasts treated with and without pyruvate. In general, the lack of pyruvate tends to slightly increase the doubling times of both irradiated and un-irradiated cells compared to cells cultured with the supplement. However, the doubling ratio remains the same with and without pyruvate when comparing 0J and 6J samples.

Table 13: Doubling times (in hours) and doubling time ratios of irradiated and un-irradiated Re5 fibroblasts in the presence of pyruvate

Cells	Doubling time [h] 0J	Doubling time [h] 6J	6J/0J ratio
Re5	50, +/- 4	102, +/- 14	2
Re5 -pyr	58, +/- 9	114, +/- 51	2

3.3. ^{13}C- Glucose and ^{13}C-Pyruvate labelling show lactate, acetate, and alanine as major components of pyruvate and glucose metabolism secreted after UVA-irradiation

As seen in 3.2, the absence of pyruvate from the medium had no effect on fibroblast morphology, vitality or proliferation. However, this does not imply that there are no changes occurring on a metabolic level. This is especially true since pyruvate can be used by the cell as an additional carbon source besides glucose.

The data presented in Fig. 21 (section 3.1.3) show that UVA results in increased glucose consumption and lactate production in human Re5 and WT01 fibroblasts. These changes occur in culture medium containing 1mM pyruvate. This pyruvate concentration is much higher than the physiological levels in human blood. Therefore, in order to elaborate the influence on this medium additive on glucose metabolism, a ^{13}C-labelling experiment was performed on Re5 fibroblasts. Three different labelling media were used for the experiment – 1) DMEM containing ^{13}C-labelled glucose (5.5mM) and no pyruvate; 2) DMEM containing ^{13}C-labelled glucose (5.5mM) and 1mM un-labelled pyruvate; 3) DMEM containing ^{13}C-labeled pyruvate and 5.5mM un-labelled glucose. The exact labelling procedure is described in detail in 2.3.9.

In brief, Re5 fibroblasts were seeded at density 5x10^4 cells per well on a 6-well plate in DMEM (1g/L glucose without pyruvate). Cells were cultured overnight (ON). The next day a complete medium exchange (5ml medium/well with 1mM ^{13}C-pyruvate was performed and the standard 4d irradiation protocol was implemented (see 2.3.5.). For the glucose labelling, the cells were divided in two groups – cells cultured with 0mM or 1mM pyruvate. A 4d irradiation was performed as per 2.3.5. Afterward, the supernatant was collected and NMR analysis was performed (1D and 2D-HSQC). All samples were filtered before the measurement to remove proteins. To compare with the labelling, samples with 1mM pyruvate (unlabelled) were also filtered and assayed. The labelled/unlabelled ratio was determined by comparing peak volumes of labelled and unlabelled samples determined in 2D-HSQC.

Both glucose and pyruvate labelling resulted in labelled lactate. As seen in Fig. 24 B, in the case of ^{13}C-glucose cells cultured in the absence of pyruvate secrete labelled lactate in the same amount as the lactate detected in the corresponding unlabelled samples. For the cells cultured with 1mM pyruvate and ^{13}C-glucose, the labelled lactate constituted roughly two-thirds of the total unlabelled lactate detected after irradiation. The remaining one-third of the lactate for these samples was derived from pyruvate, as seen from the ^{13}C-pyruvate labelling data presented in Fig. 24 B.

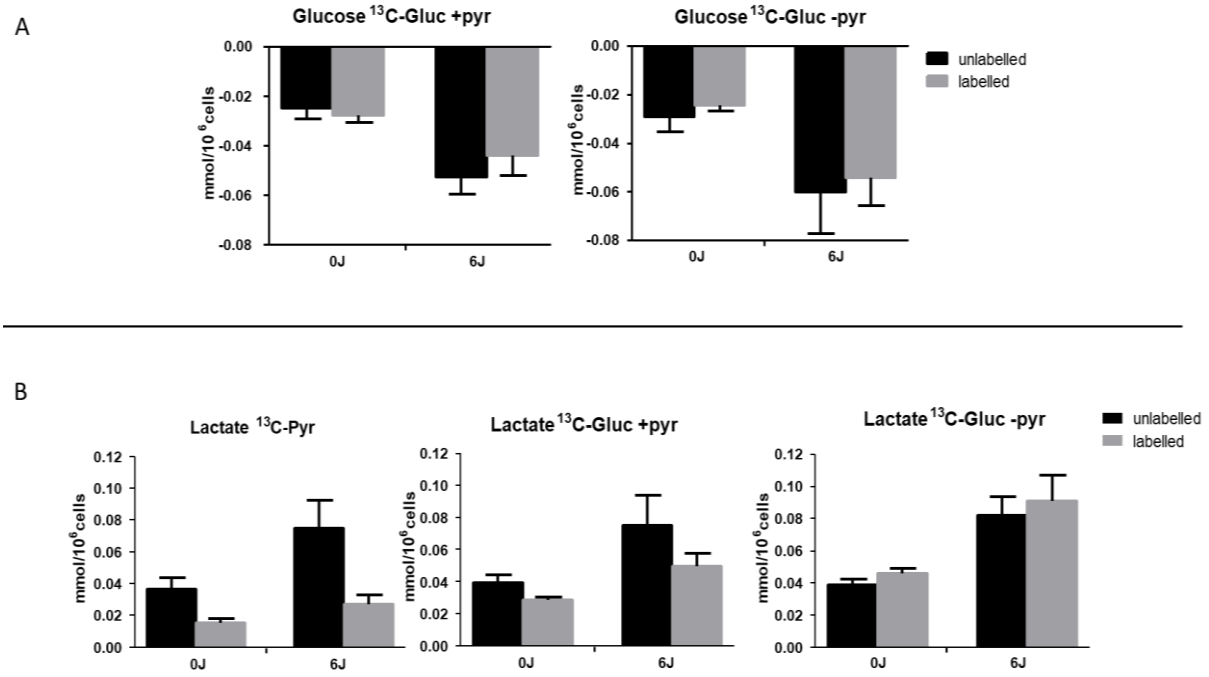

Fig. 24: (A) Glucose consumption and (B) lactate production after ^{13}C-labelling in human epidermal fibroblasts Re5 after 4d of UVA-treatment (3x per day, 6J/cm2 per treatment). Cells labelled with ^{13}C-glucose (1g/L (5.5mM)) were cultured with 1mM pyruvate or without pyruvate. Cells labelled with ^{13}C-pyruvate (1mM) were cultured in medium containing 1g/L (5.5mM) glucose. Cells culture in the absence of pyruvate derive their labelled lactate entirely from glucose. Cells kept in medium containing 1mM pyruvate had both glucose and pyruvate as sources for labelled lactate in a 2:1 ratio (glucose : pyruvate). (n=3)

Besides lactate, the ^{13}C-glucose treatment showed labelling in pyruvate, acetate, and alanine, indicating these three metabolites, together with lactate, as the main products of glycolysis. ^{13}C-pyruvate also resulted in labelled acetate and alanine but not in labelled glucose, which is indicative of absent gluconeogenesis. The data for acetate and alanine presented in Fig. 25 A and B respectively, show that, unlike alanine, acetate does not come exclusively from glucose and pyruvate metabolism. The amount of labelled acetate secreted from cells cultured with ^{13}C-glucose and 1 mM pyruvate after irradiation is only a third of the total released acetate in the unlabelled medium after UVA-treatment. On the other hand, the amount of labelled acetate derived from pyruvate is a third of the total released acetate in the unlabelled medium after irradiation (see Fig. 25). This is indicative of alternative pathways involved in the acetate generation. Another important point worth mentioning is that UVA treatment resulted in increased metabolic activity compared to untreated cells. Both the consumption of glucose and the release of lactate, acetate, and alanine was higher in irradiated samples than in unirradiated counterparts.

With the exceptions of the abovementioned metabolites and the labelling agents themselves, no other labelled compounds were detected, meaning that from the

secreted metabolites in the supernatant of human fibroblasts Re5 only acetate, alanine and lactate are derived from pyruvate.

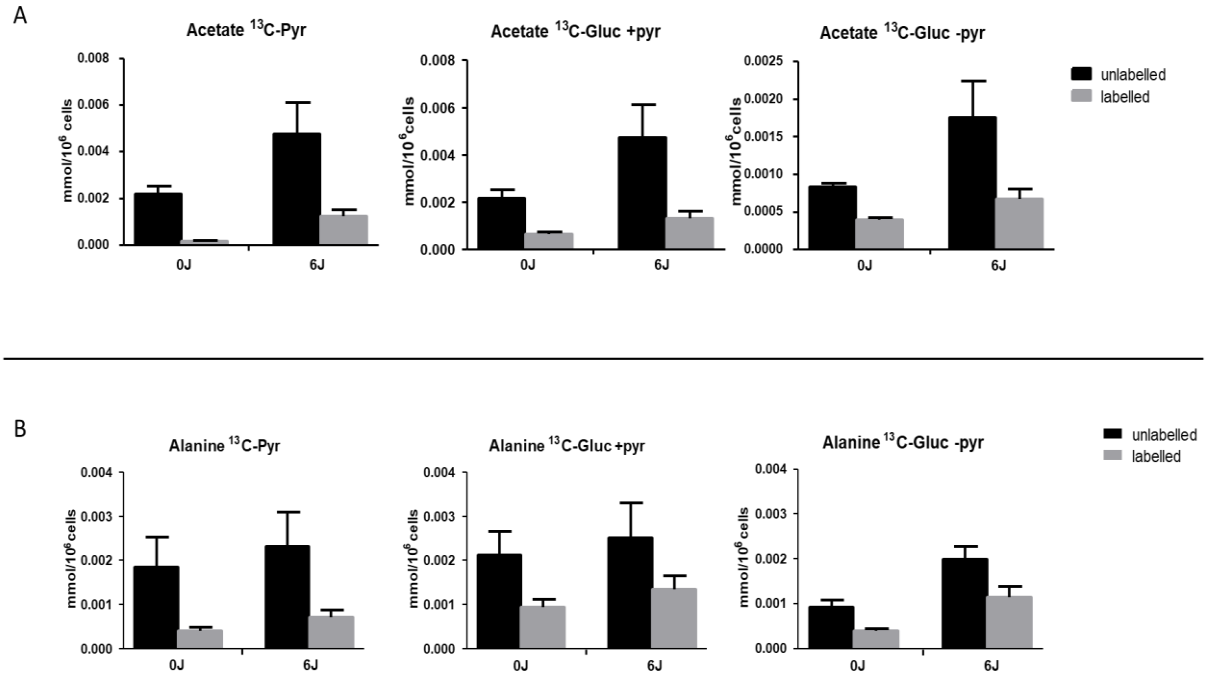

Fig. 25: (A) Acetate and (B) alanine production as detected by ^{13}C-labeling in human epidermal fibroblasts Re5 after 4d of UVA-treatment (3x per day, 6J/cm^2 per treatment). Cells labelled with ^{13}C-glucose (1g/L (5.5mM)) were cultured with 1mM pyruvate or without pyruvate. Cells labelled with ^{13}C-pyruvate (1mM) were cultured in medium containing 1g/L (5.5mM). The total amount of labelled acetate from derived from ^{13}C-glucose and ^{13}C-pyruvate is ca. 30% less than the total amount of unlabelled pyruvate after irradiation. Alanine secreted in the medium is derived completely from glucose and pyruvate. (n=3)

The metabolisation of pyruvate is presented in Fig. 26. The ^{13}C-pyruvate labelling showed higher pyruvate consumption in the labelled samples compared to the unlabelled controls. As for the results from ^{13}C-glucose labelling, the cells cultured in DMEM containing 1mM pyruvate had very high levels of pyruvate production, compared with pyruvate consumption in the unlabelled samples. Lastly, fibroblasts irradiated in ^{13}C-glucose medium without pyruvate released labelled pyruvate in the supernatant. Its amount was approximately a tenth from the labelled pyruvate released by cells cultured in DMEM with ^{13}C-glucose and 1mM pyruvate.

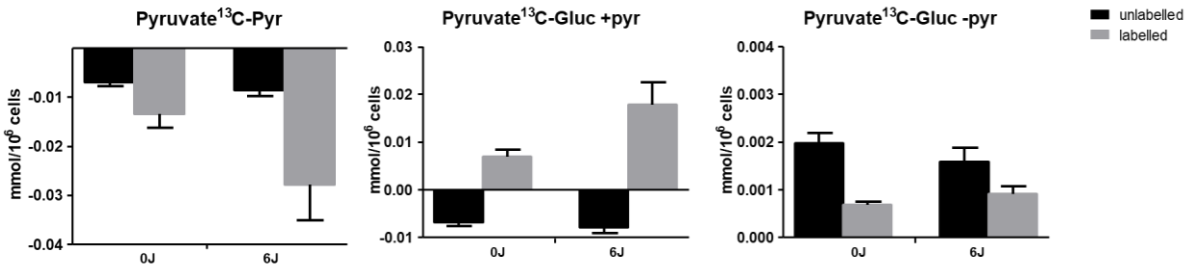

Fig. 26: Data of pyruvate metabolism as detected by labelling Re5 fibroblasts with ^{13}C-Pyruvate and ^{13}C-Glucose after 4d of UVA-treatment (3x per day, 6J/cm^2 per treatment). (n=3). Cells labelled with ^{13}C-glucose (1g/L (5.5mM)) were cultured with 1mM pyruvate or without pyruvate. Cells labelled with ^{13}C-pyruvate (1mM) were cultured in medium containing 1g/L (5.5mM). The cells show a dynamic metabolism described by pyruvate consumption and release with glucose being the main source for pyruvate synthesis (as seen from the data collected from cells cultured with ^{13}C-Glucose in the absence of external pyruvate source). (n=3)

3.4. UVA-induced metabolic changes in Re5 human fibroblasts are not limited to an increase in glucose consumption and lactate production

As shown in 3.1. irradiating non-malignant skin cells with repeated doses of UVA leads to clear changes in their glucose metabolism. Much like the results presented by Kamenisch and associates (53), irradiation resulted in increased glucose consumption and lactate production. In Re5 human fibroblasts, the glucose metabolization to lactate was similar to the Warburg-like effect observed in cancer cells (53) with glucose to lactate conversion of almost 1:2 (lactate-to-glucose ratio of about 1.7) (see Table 12).

To clarify whether the irradiation results in other metabolic changes, supernatants from Re5 fibroblasts were measured with an NMR-spectrometer. In addition to the irradiation, the cells were cultured in the presence of 1mM pyruvate (standard DMEM) and in medium containing no pyruvate, which is closer to the physiological pyruvate levels detected in blood. Like that, the influence of the medium-contained pyruvate on the cell metabolism in comparison to the natural, almost pyruvate-free skin milieu could be further studied.

The NMR analysis was performed using the CPMG-protocol without filtering the samples in accordance with the method described in 2.3.8. The formic acid peak was used as a reference to determine the absolute concentration of the measured metabolites instead of TSP. This was necessary due to the un-filtered proteins from

the medium intercalating with TSP and resulting in a broader peak unsuitable as quantification reference.

The results shown in Fig. 27 and Fig. 28. represent the metabolites that could be detected in both samples cultured with and without pyruvate, and showed significant differences between bot UVA and pyruvate treatments.

Significant changes in the cell metabolism after UVA-irradiation could be seen in samples cultured without pyruvate compared to the pyruvate-cultured ones (1mM pyruvate in the culturing medium). After UVA-treatment, there is an increase in glucose consumption and increase in the production of glutamate and pyroglutamate in cells cultured without pyruvate, compared to irradiated cells cultured with pyruvate (Fig. 27). Lactate also shows a significant increase in samples without pyruvate. Cells cultured without pyruvate tend to metabolize glucose, lactate, glutamine, glutamate, and pyroglutamate to a higher amount compared to the corresponding controls. Even cells that have not been UVA irradiated show these tendencies of increased metabolic activity in the absence of pyruvate, although mostly not statistically significant (see Fig. 27).

Despite the observed overall increase in glucose consumption and lactate production after removing pyruvate from the culturing medium, the lactate-to-glucose ratios did not change significantly between the different pyruvate culturing conditions. UVA had again no influence on the lactate-to-glucose ratios (Fig. 27).

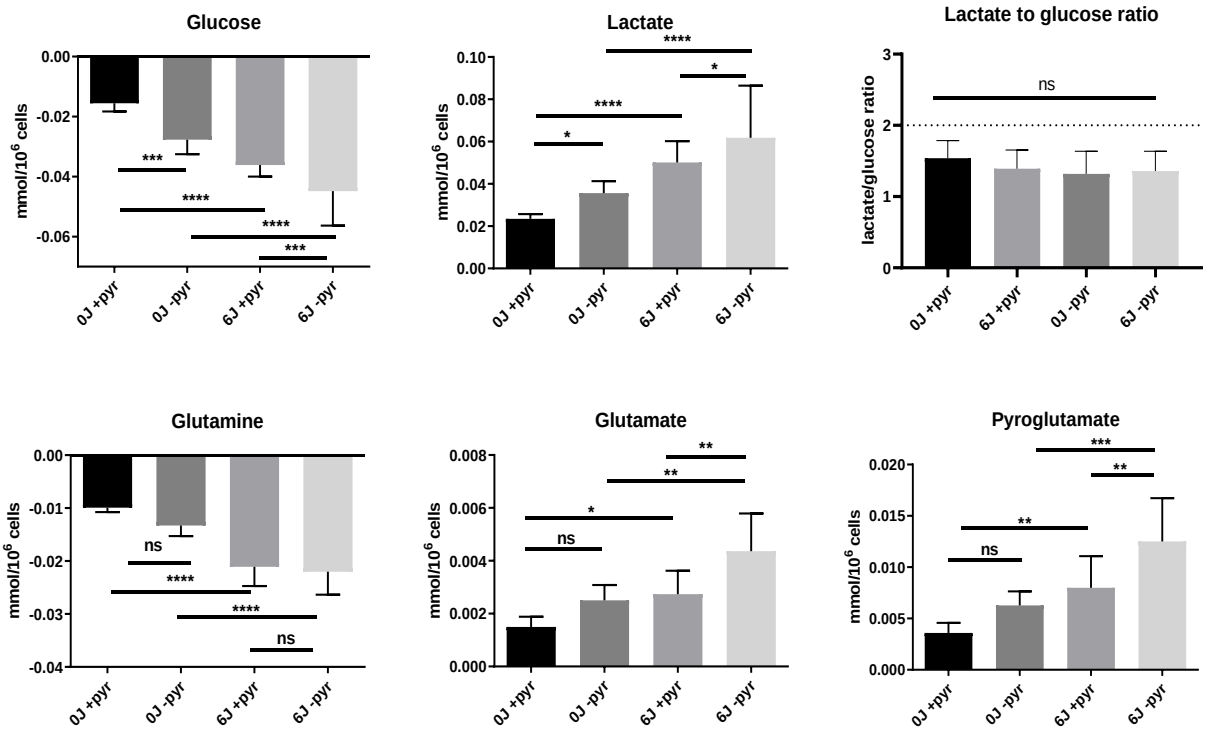

Fig. 27: *NMR-measured metabolic changes in the supernatant of Re5 after 4d irradiation with and without pyruvate in the culturing medium. For these metabolites, the absence of pyruvate in the cell culture medium tends to increase metabolic activity, leading to increase of consumption or production of the respective metabolite. The dash-line represents an ideal glucose to lactate conversion of 1 to 2, associated with aerobic glycolysis. ((n=3), Statistical analysis Two-way ANOVA with Bonferroni's multiple comparison test. For significances: (ns) P > 0.05; (*) P < 0.05; (**) P < 0.005; (***) P < 0.0005; (****) P < 0.0001).*

Contrary to that, acetate and alanine production, as well as cystine consumption significantly decreased in irradiated cells cultured without pyruvate, compared to cells cultured in a pyruvate-containing medium during irradiation. Pyruvate metabolism itself also unsurprisingly changes depending on the medium used. Cells cultured in 1mM pyruvate consumed pyruvate from the medium in contrast to the pyruvate secretion observed in cells cultured in DMEM without pyruvate. Comparing irradiated and un-irradiated cells, samples that received 1mM pyruvate in combination with UVA treatment consume larger amounts of pyruvate than their un-irradiated counterparts. What is also interesting is that cells cultured without pyruvate tend to secrete less pyruvate in the medium after irradiation compared to their corresponding un-irradiated controls, which is similar to acetate, alanine, and cystine.

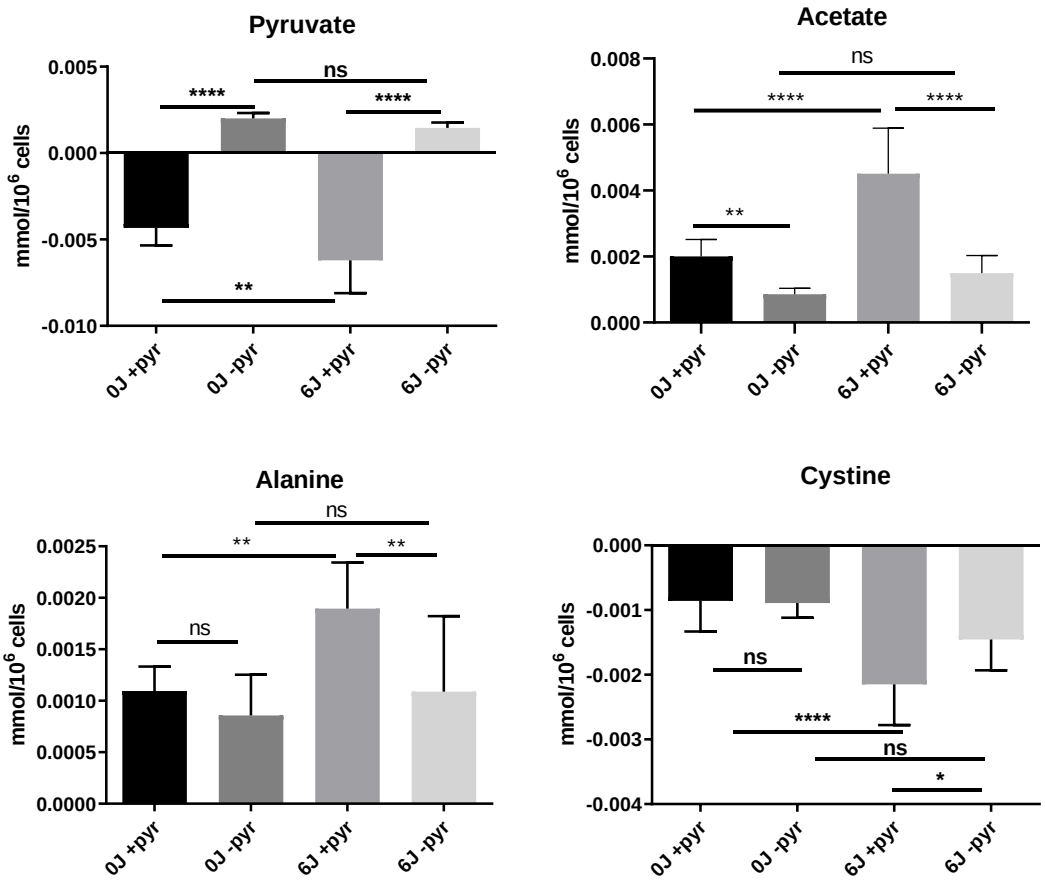

Fig. 28: NMR-measured metabolic changes in supernatant of Re5 after 4d irradiation with and without pyruvate in the culturing medium. For these metabolites the absence of pyruvate in the cell culture medium tends to decrease metabolic activity. (Statistical analysis: Two-way ANOVA with Bonferroni's multiple comparison test. For significances: (ns) P > 0.05; (*) P < 0.05; (**) P < 0.005; (***) P < 0.0005; (****) P < 0.0001). (n=3)

The NMR-measured supernatants yielded an interesting metabolic fingerprint for cells cultured with and without pyruvate. Besides the metabolites that could be stably detected in both treatments, some compounds were present only in cells treated with 1mM pyruvate or cultured in the complete absence thereof.

The data shown in Fig. 29 represent metabolites stably detected only in supernatants of cells cultured in the presence of pyruvate. UVA irradiation resulted in increased metabolic activity of the cells. There was increased consumption of isoleucine, histidine, lysine, serine, sarcosine and valine, compared to un-irradiated samples. These metabolites could not be stably detected in samples without pyruvate, with some samples having metabolite consumption and some release between three biological replicates.

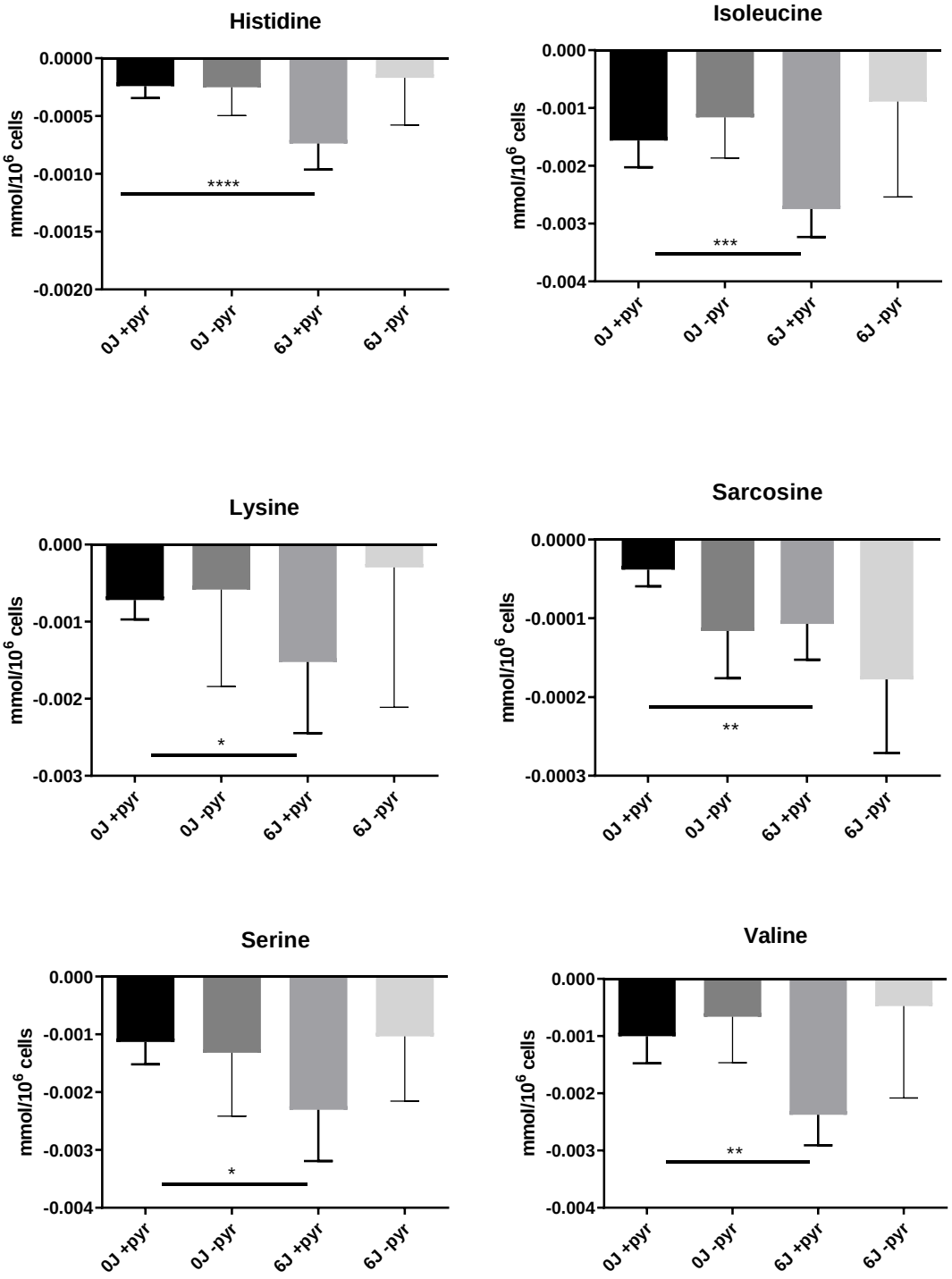

Fig. 29: NMR-measured metabolic changes in the supernatant of Re5 after 4d UVA treatment. The metabolic changes were stably detected only in samples cultured with 1mM pyruvate. *(Statistical analysis: Two-way ANOVA with Bonferroni's multiple comparison test. For significances: (ns) P > 0.05; (*) P < 0.05; (**) P < 0.005; (***) P < 0.0005; (****) P < 0.0001). (n=3)*.

In the samples from cells cultured without pyruvate only proline and asparagine levels were significantly changed after irradiation (Fig. 30). There is an increase in the secretion of these two amino acids in the culture medium.

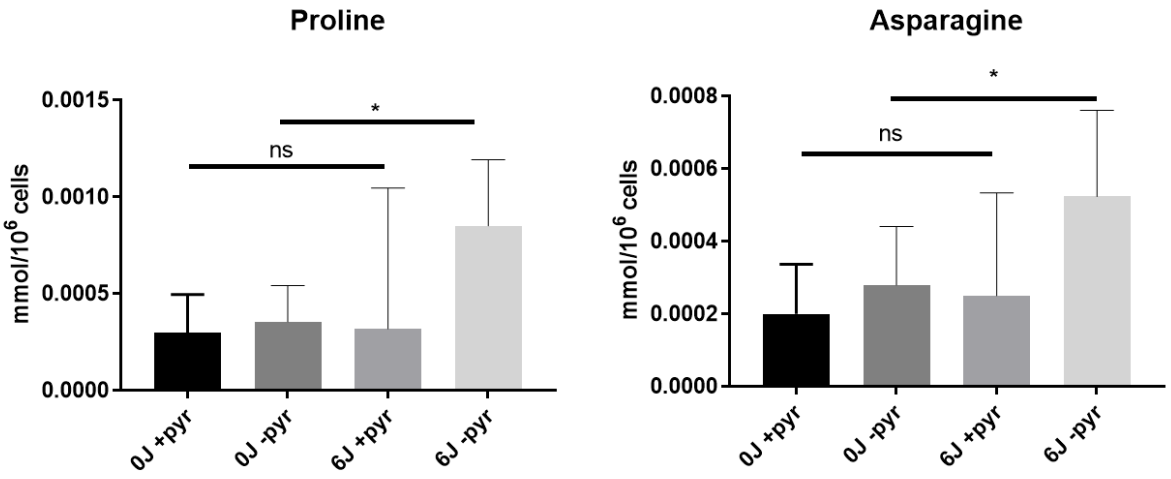

Fig. 30: *NMR-measured metabolic changes in supernatant of Re5 after 4d UVA treatment. The metabolic changes were stably detected only in samples cultured without pyruvate. ((n=3), Statistical analysis: Two-way ANOVA with Bonferroni's multiple comparison test. For significances: (*) P < 0.05).*

Some previous studies have considered pyruvate to be a potent antioxidant. There have been publications of its enzymatic decarboxylation to acetate as a way to detoxify ROS (87). Although there have been publications about the anti-oxidative capacity of pyruvate in the presence of H_2O_2 and as an anti-oxidant in UVB-treated guinea pigs (see I.1.), there have been no extensive studies of the influence of pyruvate its influence on cell metabolism during UVA-irradiation.

To see whether pyruvate exerts its antioxidant properties in UVA irradiated cells, firstly the amount of pyruvate and acetate was compared in the different samples (see Fig. 31). In cells cultured with pyruvate, the latter was consumed from the medium with the consumption increasing after UVA treatment. At the same time, acetate was released in the supernatant and its secretion was also increased after irradiation. For cells cultured without pyruvate, both pyruvate and acetate were secreted into the culture medium. UVA irradiation decreased pyruvate production but increased the secretion of acetate resulting in pyruvate to acetate ratio of 1:1.

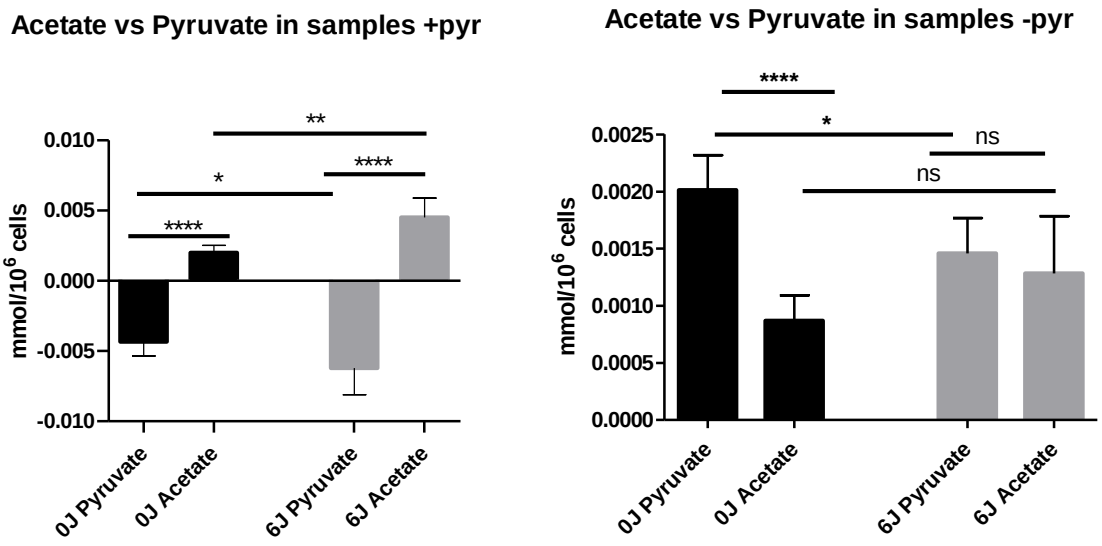

Fig. 31: Comparing the ratio of pyruvate to acetate in samples with/without pyruvate (0mM/1mM) after treatment with 0J or 6J/cm^2 UVA. The levels of secreted pyruvate decrease compared to increased acetate secretion. (*(n=3),* Statistical analysis: *Two-way* ANOVA with Bonferroni's multiple comparison test. For significances: (ns) P > 0.05; (*) P < 0.05; (**) P < 0.005; (***) P < 0.0005; (****) P < 0.0001).

3.5. UVA induces metabolic changes in the medium of *ex vivo* cultured murine skin

As shown above, human fibroblasts showed significant metabolic changes after UVA irradiation, coupled with pyruvate-dependent changes in gene expression and ROS production. However, the skin is a much more complex system than a simple monocellular culture. Therefore, metabolic analysis of *ex vivo* cultured mouse skin was the next-closest experimental setup to a human *in vivo* skin model. Since there was the possibility of necrosis of the skin-explant due to prolonged cultivation *ex vivo* the irradiation protocol was reduced from 4d to 2d irradiation.

The skin was harvested from 129 Sv/Ev WT mice as described in 2.3.4. The irradiation was started immediately after skin isolation as described in 2.3.5.2. After the irradiation, the culture medium (containing 5.5mM glucose and 1mM pyruvate) was collected and metabolic changes were measured via NMR (1D-CPMG). Control medium samples (medium treated with 0J/6J UVA without skin) were subtracted from each skin-supernatant sample. The results of the metabolic analysis are shown in the graph below. A Student-t-test, followed by a 10% and 1% FDR-analysis was

performed. No normalization to volume or sample weight was performed since all samples were of identical size.

The NMR analysis yielded a complex metabolic profile for the skin supernatant depicted in Fig. 32 and Fig. 33. The metabolites shown in Fig. 32 correspond to the ones observed in Re5 fibroblast's supernatant from Fig. 27 and Fig. 28.

Contrary to expectation, there was no detectable change in glucose consumption or lactate production between irradiated and non-irradiated samples. This contradicts with the *in vitro* data from the skin cell culture shown in 4.2. and 4.3. Similar to the data obtained from cultured fibroblasts, an increase in acetate production could be seen in the irradiated skin samples. The glutamate and cystine metabolism remained similar between fibroblasts and skin samples. Pyruvate consumption, however, showed differences between the skin punches and the cultured fibroblasts – in fibroblasts UVA irradiation results in increase consumption, compared to untreated control. In the *ex vivo* skin setup, the irradiated samples showed lower pyruvate consumption compared to untreated controls. Alanine metabolism also showed differences between cells and whole skin. In the irradiated fibroblasts there was an increase in alanine production after irradiation but in skin alanine production decreased after UVA treatment. Glutamine, present in cell supernatants, could be detected in the ex vivo mouse skin, but compared to an increase in glutamine consumption of irradiated fibroblasts there was no significant difference between irradiated and un-irradiated samples (see Fig. 36 A). Pyroglutamate also showed different behaviour between skin and fibroblasts samples. Irradiated fibroblasts had increased release of pyroglutamate in the supernatant but the skin punches consumed it from the medium with irradiated skin consuming less pyroglutamate compared to un-irradiated control.

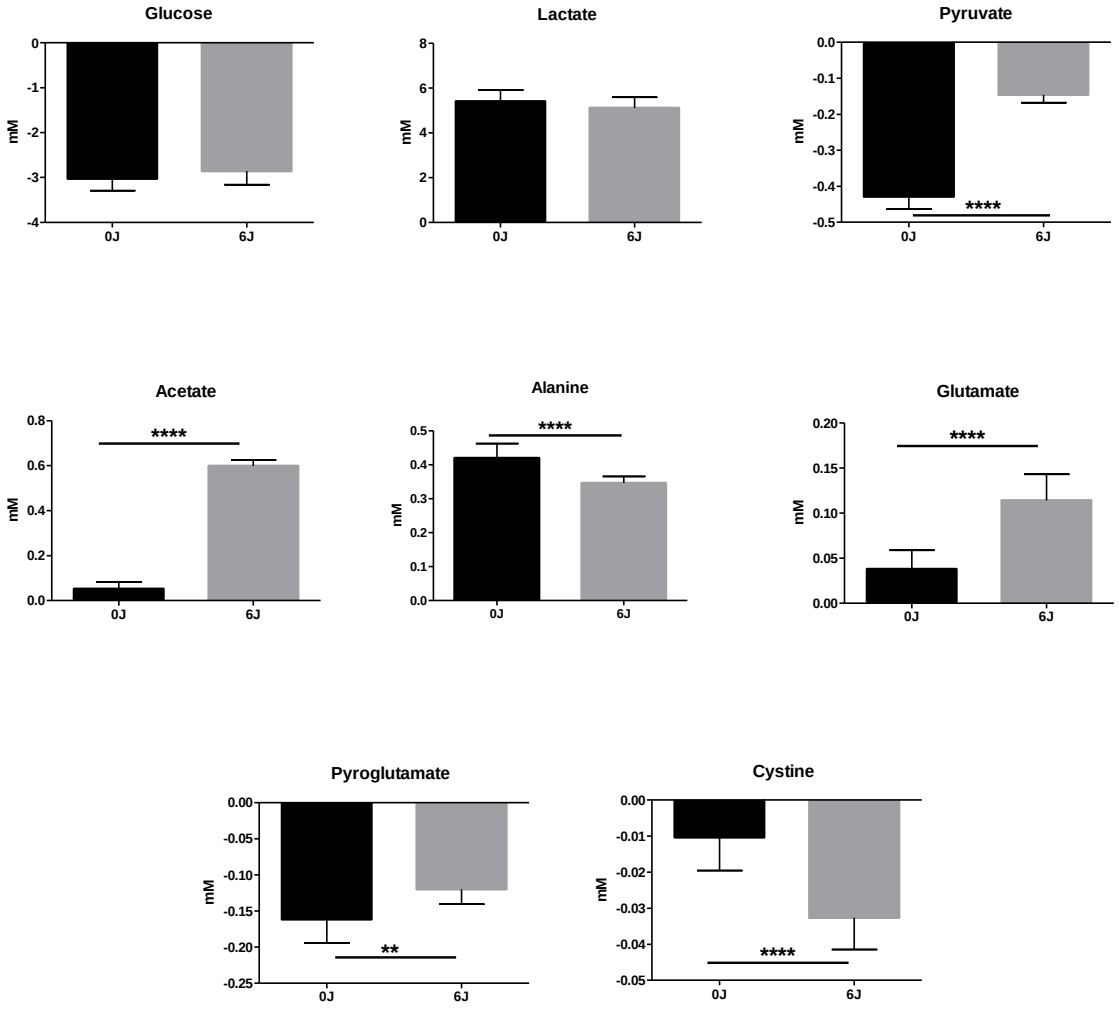

Fig. 32: Metabolic changes in the supernatant of ex-vivo cultured mouse skin after 2d of UVA irradiation (3x treatment per day, 6 J/cm² per treatment). The skin samples were cultured in DMEM 1 g/L (5.5mM) glucose and 1mM pyruvate. (n=7)

Not all metabolites detected in the skin explant culture could also be stably detected in all cell culture samples. For example, histidine, which was detected only in cells cultured with 1mM pyruvate, could also be detected in the skin samples (Fig. 33). In this case, the consumption of histidine increased with irradiation in fibroblasts but decreased in the skin supernatant.

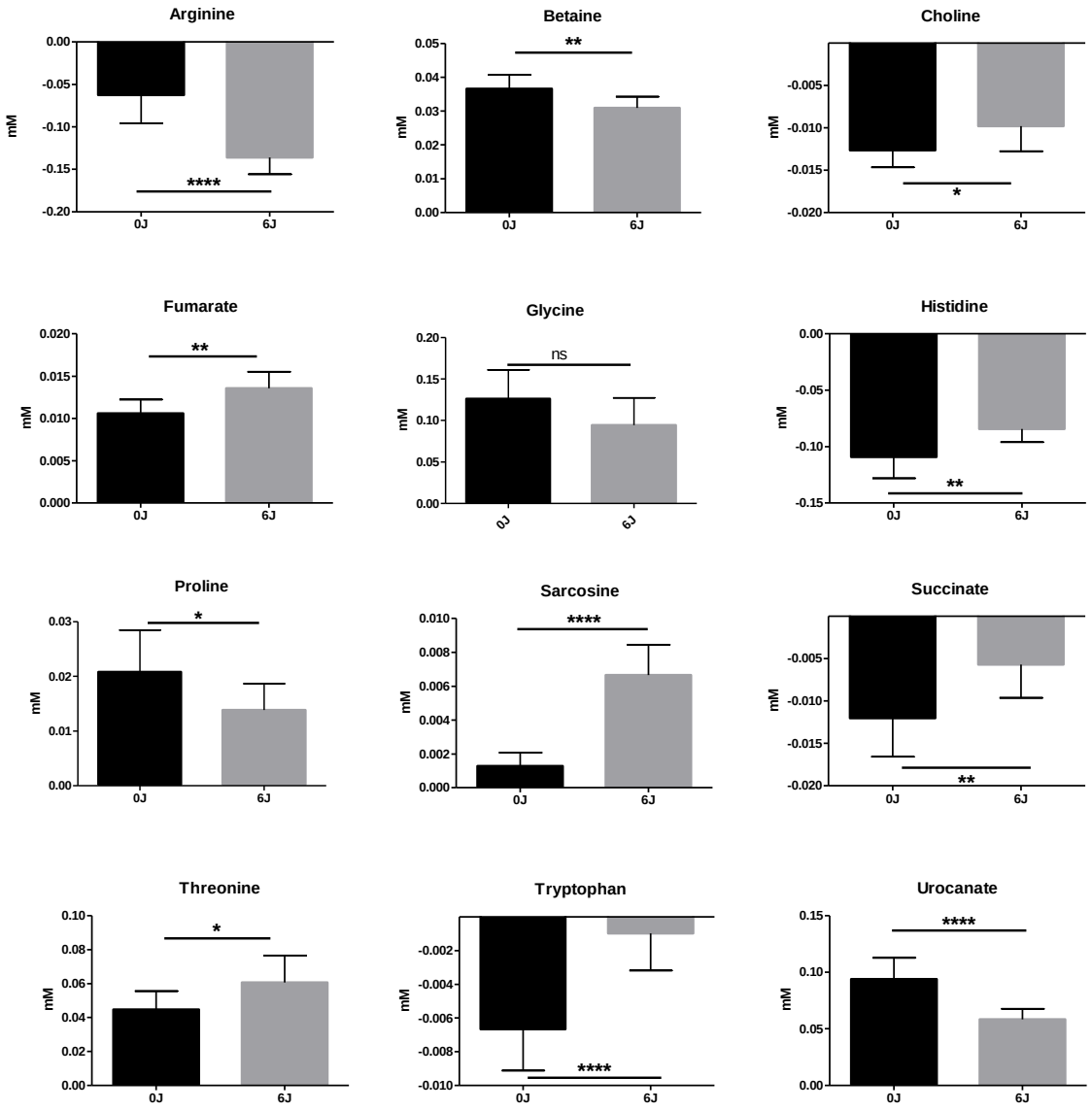

Fig. 33: Metabolites detected mainly in the supernatant of of ex-vivo cultured mouse skin after 2d of UVA irradiation (3x treatment per day, 6 J/cm^2 per treatment) but not present in cell culture or only detectable in cell culture under some conditions. The skin samples were cultured in DMEM 1 g/L (5.5mM) glucose and 1mM pyruvate. (n=7)

Arginine, betaine, choline, fumarate, proline, succinate, tryptophan, threonine, and urocanate could be detected only in skin samples (Fig. 33) but not in fibroblasts. From them, arginine consumption and fumarate, sarcosine, and threonine release in the medium increased with irradiation. On the contrary, betaine, proline and urocanate production and choline, histidine, succinate, and tryptophan consumption decreased after UVA treatment (Fig. 33).

Isoleucine, lysine, serine, and valine could not be detected in the skin supernatant, despite being present in fibroblast samples.

The detected metabolites and their behaviour in the presence of UVA make up a metabolic profile different than the one described for Re5 fibroblasts. A false discovery rate test (FDR) was performed for all discovered metabolites using GraphPad Prism. For FDR 10 %, which would allow for only 10 % of false-positive results, all changes were designated as “true discovery”. If FDR was set to tolerate only 1% of false discoveries, changes in choline, proline, and threonine, fall out (see Table 14a and b).

Table 14a: Calculating 10 % FDR for ex vivo cultured mouse skin (1D-CPMG-NMR samples)

Metabolite	Discovery?	P value	q value
Acetate	Yes	0,0001	0,0002
Alanine	Yes	0,0001	0,0002
Arginine	Yes	0,0001	0,0002
Betaine	Yes	0,0034	0,0044
Choline	Yes	0,0211	0,0237
Cystine	Yes	0,0001	0,0002
Fumarate	Yes	0,0017	0,0028
Glutamate	Yes	0,0001	0,0002
Histidine	Yes	0,0023	0,0035
Proline	Yes	0,0312	0,0312
Pyroglutamate	Yes	0,0031	0,0043
Pyruvate	Yes	0,0001	0,0002
Sarcosine	Yes	0,0001	0,0002
Succinate	Yes	0,0048	0,0058
Threonine	Yes	0,0303	0,0312
Tryptophan	Yes	0,0001	0,0002
Urocanate	Yes	0,0001	0,0002

Table 14b: Calculating 1 % FDR for ex vivo cultured mouse skin (1D-CPMG-NMR samples)

Metabolite	Discovery?	P value	q value
Acetate	Yes	0,0001	0,0002
Alanine	Yes	0,0001	0,0002
Arginine	Yes	0,0001	0,0002
Betaine	Yes	0,0034	0,0044
Choline	No	0,0211	0,0237
Cystine	Yes	0,0001	0,0002
Fumarate	Yes	0,0017	0,0028
Glutamate	Yes	0,0001	0,0002
Histidine	Yes	0,0023	0,0035
Proline	No	0,0312	0,0312
Pyroglutamate	Yes	0,0031	0,0043
Pyruvate	Yes	0,0001	0,0002
Sarcosine	Yes	0,0001	0,0002
Succinate	Yes	0,0048	0,0058
Threonine	No	0,0303	0,0312
Tryptophan	Yes	0,0001	0,0002
Urocanate	Yes	0,0001	0,0002

Since the amount of 1mM pyruvate standardly used in the cell culture is far from the physiological levels, a variation of the mouse skin experiment was performed with adjusted pyruvate values. Optimization of the culturing protocol for murine skin was also performed. The skin was pre-incubated in DEMEM for 1d to saturate it with glucose due to the lack of glucose metabolism change observed in the previous experimental setup. The culturing medium was similar to the one used in the previous experiment with the exception of the pyruvate concentration – 200 µM pyruvate, corresponding to the values found in murine blood (120, 121) instead of 1mM contained in the standard DMEM formulation. An additional condition of skin punches cultured in increased glucose concentration (2 g/L (11mM) instead of the usual 1 g/L (5.5mM)) was also added to ensure glucose saturation of the samples.

After the pre-incubation, the skin punches were irradiated as described in 2.3.5.2. and the supernatant was collected for NMR-analysis.

Due to the prolonged *ex vivo* cultivation, an NBTC-(nitroblue tetrazolium chloride)-vitality-test was performed on frozen samples to determine the amount of necrotic tissue (see Fig. 34). The samples tested were from the middle section of an 8mm skin punch, where the highest levels of necrosis were expected due to nutrient

deficiency. The staining itself was performed as described in 2.3.15. With this assay, necrotic cells should not show any colour compared to stained vital tissue. As seen in the four representative slides in Fig. 34, no necrosis was detected in any sample at the end of the experiment, showing that the tissue was vital during the performed treatments. Colourless areas in the dermis are due to the fact that NBTC does not stain collagen.

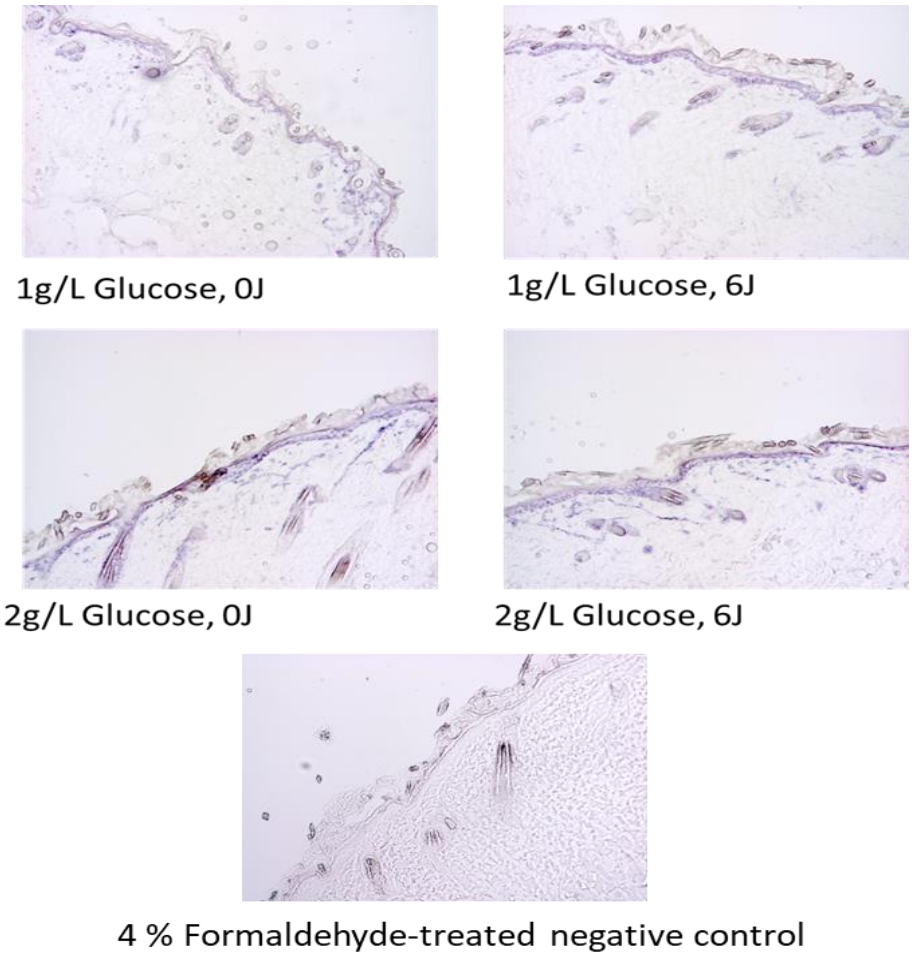

Fig. 34: NBTC viability staining of ex-vivo cultured mouse skin after UVA irradiation (3x 6J/cm^2 for 2 days) of tissues cultured with 1-2 g/L glucose and 200µM pyruvate. No necrotic areas were detected under these culturing conditions. As a control for necrosis, a skin section was treated 15 min with 4% formaldehyde solution in order to produce non-viable tissue.

Similar to the previous *ex vivo* experiment, 1D-CPMG-NMR was performed in order to determine the metabolic changes in the supernatant. Control medium samples (medium treated with 0J/6J UVA without skin) were subtracted from each skin-supernatant sample. The results of the metabolic analysis are shown in Fig. 35. No statistical analysis was performed due to the fact that only 2 mice were used in the experiment, yielding an insufficient sample number.

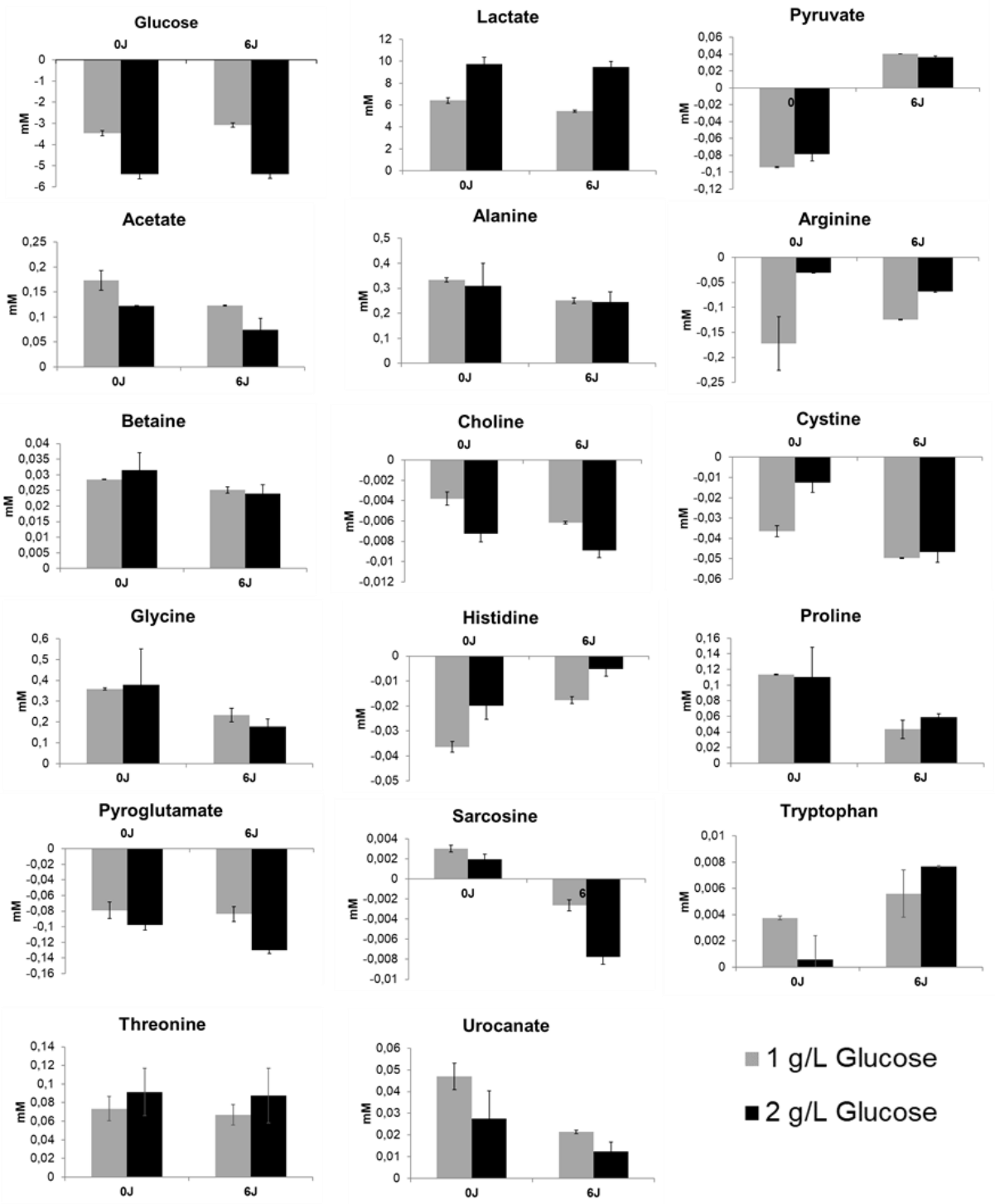

Fig. 35: Metabolic changes in supernatant of ex-vivo cultured mouse skin after UVA irradiation (3x 6J/cm² for 2 days). The issues were cultured with 1-2 g/L glucose and 200µM pyruvate and pre-incubated for 1 day in the corresponding media before the start of irradiation. Changing the culturing conditions of the skin punches showed distinctive changes in the metabolic profile compared to the ones cultured in 1mM pyruvate and 1g/L (5.5 mM) glucose (see Fig. 33).

Despite pre-incubation, neither glucose and nor lactate showed any changes before and after irradiation. Pyruvate had a very distinct profile, different from the previous skin experiment (1mM pyruvate). Irradiated samples showed production, but

un-irradiated ones consume pyruvate from the medium. This process, however, did not seem to be glucose-dependent, since different glucose concentrations did not change the overall behaviour of this metabolite. Acetate production decreased in a glucose-dependent manner in irradiated samples. Compared to that, there was an increase in acetate release by UVA-treated skin in the previous experiment (1mM pyruvate). This behaviour is also contrary to the one exhibited by fibroblasts in cell culture (see Fig. 28) who experienced an increase in acetate production after irradiation.

The metabolic profile of alanine, histidine, cystine, proline, betaine, and urocanate remained similar, independent of different pyruvate concentrations in the two skin experiments (200µM/1mM pyruvate) (Fig. 35 and Fig. 32), but urocanate and histidine showed a glucose-dependent decrease in production and consumption respectively after UVA irradiation. For these metabolites, higher glucose levels in the medium lowered their overall values independent of irradiation. Choline and pyroglutamate, on the other hand, showed higher levels in the presence of 2 g/L glucose. Compared to the previous skin experiment (1mM pyruvate), UVA-irradiation increased pyroglutamate consumption instead of decreasing it. As for choline, it too exhibited a reversed metabolic behaviour after irradiation in this experimental setup compared to the previous one. Mouse skin, cultured in 200µM pyruvate had increased choline consumption after irradiation compared to decrease in consumption in the corresponding samples cultured in 1mM pyruvate.

Threonine und tryptophan could be detected in both 1mM and 200µM pyruvate cultured samples. Threonine was released into the medium but UVA had no major influence on its secretion in the 200µM-pyruvate samples. Tryptophan, however, showed completely different behaviour under lower pyruvate conditions compared to the 1mM samples. The metabolite was consumed from the medium when 1mM pyruvate was present but released when the pyruvate concentration was reduced to 200µM. This secretion was also UVA dependant.

As seen in Fig. 35, arginine consumption shows significant glucose dependency. Skin samples irradiated with 1 g/L (5.5mM)glucose and 200µM pyruvate in the medium have overall higher histidine consumption than the ones cultured under the same pyruvate conditions but in a high-glucose medium. There is a tendency that the samples cultured with 1 g/L (5.5mM) glucose and 200µM pyruvate consume more

arginine without irradiation. This is contrary to the behaviour of the irradiated skin in the first experiment (as shown in Fig. 33) who were cultured in 1 g/L (5.5mM) glucose and 1µM pyruvate. Interestingly, despite lowering the overall consumption, keeping the skin explants in DMEM with 2 g/L (11 mM) glucose and 200µM pyruvate showed similar irradiation behaviour as in the first skin setup, with increased consumption after UVA treatment.

Glutamate and glutamine, present in both cell culture and in the high-pyruvate (1mM) skin experiment, could also be detected here (see Fig. 36**Fehler! Verweisquelle konnte nicht gefunden werden.** B). glutamine showed only slightly increased consumption in samples cultured with 1 g/L glucose after irradiation, but not in 2 g/L (11mM) glucose. Glutamate, on the other hand, did not show any UVA-dependant metabolic changes.

Glycine could only be detected in the samples cultured in 200µM pyruvate. The irradiated cells showed a decrease in glycine secretion in the medium compared to un-irradiated controls. Glucose levels did not seem to influence this process much.

Sarcosine too showed a completely different profile compared to the first skin experiment (Fig. 33**Fehler! Verweisquelle konnte nicht gefunden werden.**). Un-irradiated samples released sarcosine in the supernatant, irradiated ones consumed it from the medium. Glucose also influences the production to consumption ratio of control to irradiated skin. When cultured in 1 g/L (5.5mM) glucose un-irradiated samples produced roughly the same amount of sarcosine as the irradiated skin released in the medium. Increasing the glucose levels of the medium resulted in shifting the balance and having drastically more sarcosine being consumed after UVA-treatment compared to the production in the corresponding untreated skin.

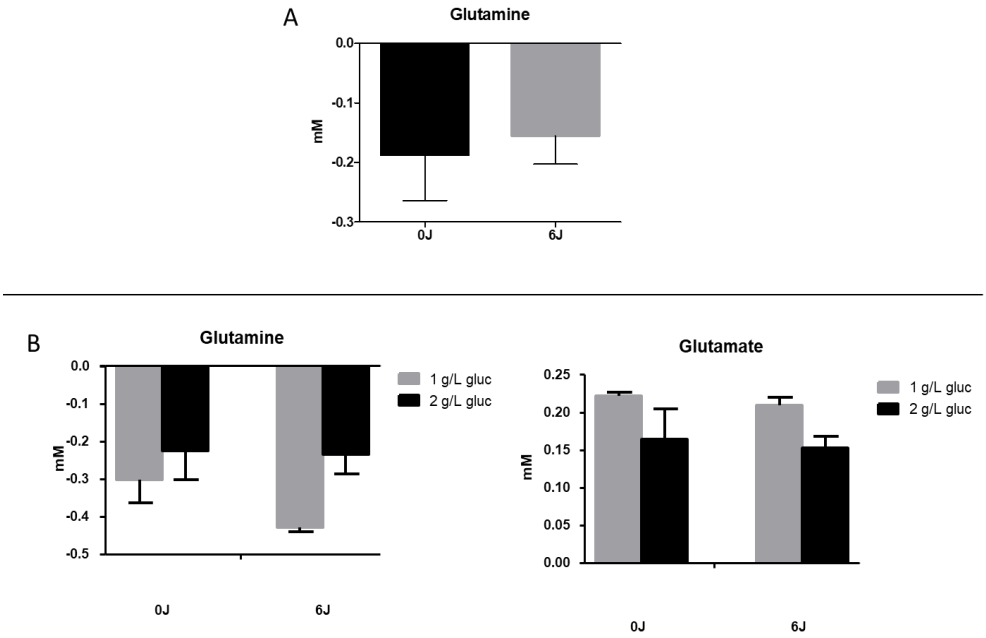

Fig. 36: (A) glutamine consumption, detected in the medium of ex vivo cultured murine skin (DMEM, 1mM pyruvate, 1g/L glucose). (B) Glutamine consumption and glutamate secretion, detected in the medium of ex vivo cultured murine skin (DMEM, 200 µM pyruvate, 1 – 2 g/L glucose).

A summary of all metabolic changes detected in fibroblast culture and *ex vivo* mouse skin is shown in Table 15. From all detected metabolites, cysteine is the only one which consumption is upregulated in both cell culture and skin explants after UVA treatment. Other metabolites that have at least partial overlaps between fibroblast monoculture and skin samples are glutamine, glutamate and acetate. The rest of the metabolites show clearly differential profile between cell culture and *ex vivo culture*.

Table 15: Comparison of metabolic profiles between supernatants of human fibroblasts (Re5) and mouse skin explants cultured in DMEM with 1 g/L glucose and 1mM/200µM/0mM pyruvate

Metabolite	**Re5 cells 1 mM pyr, 1 g/L (5.5mM) glucose 6vs0J (n=3)**	**Re5 cells 0 mM pyr, 1 g/L (5.5mM) glucose 6vs0J (n=3)**	**Mouse skin 1 mM pyr, 1 g/L (5.5mM) glucose 6vs0J (n=7)**	**Mouse skin 200 µM pyr, 1 g/L (5.5mM) glucose 6vs0J (n=2)**
Glucose	C+	C+	C=	C=
Lactate	P+	P+	P=	P=
Pyruvate	C+	P-	C-	P+ (0J C/6J P)
Glutamine	C+	C+	C=	C+
Glutamate	P+	P+	P+	P- (ns)
Pyroglutamate	P+	P+	C-	C=
Cystine	C+	C+	C+	C+
Sarcosine	C+	C+	P+	C+ (0J P/6J C)
Alanine	P+	P+ (ns)	P-	P-
Serine	C+	nd	C- (ns)	C=
Isoleucine	C+	nd	C= (ns)	C+ (0J P/6J C)
Valine	C+	nd	C=	nd
Histidine	C+	nd	C-	C-
Lysine	C+	nd	P=	nd
Proline	nd	P+	P-	P-
Asparpgine	nd	P+	P=	P-
Acetate	P+	P+	P+	P-
Arginine	nd	nd	C+	C-
Betaine	nd	nd	P-	P-
Choline	nd	nd	C-	C+
Fumarate	nd	nd	P+	nd
Succinate	nd	nd	C-	nd
Threonine	nd	nd	P+	P+ (ns)
Tryptophan	nd	nd	C-	P+
Urocanate	nd	nd	P-	P-
Glycine	nd	nd	P- (ns)	P-

Table legend	
	Overlap between at least one skin experiment and cell culture
	Overlap between skin only
	Overlap between cell culture only
P+	Production increases after irradiation
P-	Production decreases after irradiation
P=	Production remains unchanged after irradiation
C+	Consumption increases after irradiation
C-	Consumption decreases after irradiation
C=	Consumption remains unchanged after irradiation
nd	No data (no consistent behavior between replicates or simply not detected
ns	Not significant (there is visible difference between treatments, but no statistical significance

3.6. UVA induces reactive oxygen species (ROS) and DNA-damage in human fibroblasts

As seen in sections 3.1, 3.3, and 3.4, UVA irradiation induces changes in the metabolism of various non-malignant cells obtained from both human and mice. It is possible that such metabolic changes are in response to damages inflicted on the cells, since glucose is needed as an energy source to facilitate damage repair.

UVA is known to be an important source of ROS (33). To test whether the low doses of 6J/cm^2 UVA used in the experiments described above are sufficient to generate significant increase in ROS levels, human fibroblasts Re5 were treated with a single dose of 6J/cm^2 UVA and ROS formation was detected via DCFDA staining. Since the most reactive oxygen species have a very short half-life, ranging from 10^{-3} to 10^{-9} sec (122), the UVA-induced ROS was not expected to accumulate during a prolonged period of irradiation. Therefore, the cells were stained with DCFDA 30 min before irradiation, and the measurement of the generated ROS was performed no longer than 30 min after the irradiation, giving enough time for the samples to reach maximum fluorescence.

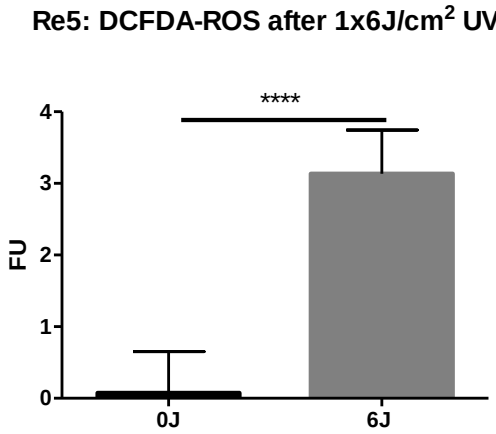

Fig. 37: A single irradiation with 6J/cm2 UVA is sufficient to induce ROS in significantly higher amounts compared to untreated controls. (n=3, Statistical analysis Student's t-test. For significances: (****) P < 0.0001).

As seen in Fig. 37, even a single irradiation dose is sufficient to induce high amounts of reactive oxygen species compared to un-irradiated controls. In the following step, it was important to see whether the produced ROS was able to damage DNA, and especially result in 8-OHdG modifications which are typically found in UVA irradiated cells (123). Since the levels of 8-OHdG are low compared to the overall dG

amount in a nucleated cell (124), it was deemed reasonable to perform the 8-OHdG detection not after a single irradiation but at two later time points – after 2d irradiation (equal to 6x6J/cm^2 applied) and 4d irradiation (equal to 12x6J/cm^2 applied). Like that, base modifications could accumulate and be more easily and accurately detected.

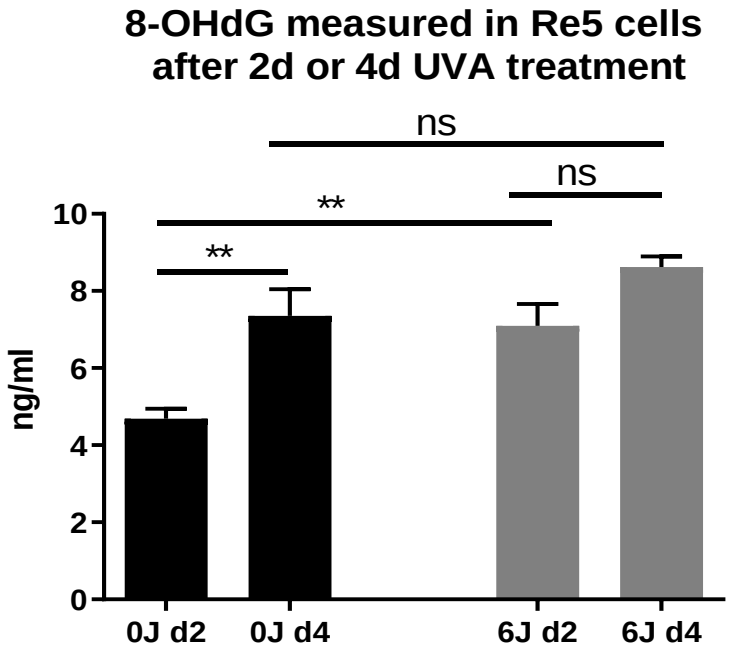

Fig. 38: Levels of 8-OHdG measured after 2d and 4d UVA irradiation. After 2d, there is a significant increase in 8-OHdG levels in the irradiated samples compared to the controls. After 4d of irradiation, the tendency remains that irradiated cells have more 8-OHdG, but the difference between irradiated and un-irradiated samples is no longer statistically significant. (n=3; Statistical analysis: Two-way ANOVA with Bonferroni's multiple comparison test. For significances: (ns) p > 0.05; (**) p < 0.005).

As observed in Fig. 38, there is a significant increase in 8-OHdG levels after 2d in the irradiated samples compared to the controls. After 4d of irradiation, the tendency remains that irradiated cells have more 8-OHdG, but the difference between irradiated and un-irradiated samples is no longer statistically significant. However, there is still significant increase observed between the un-irradiated samples of d2 and d4. There is also a tendency that irradiated cells at d4 have slightly higher, albeit not significant, 8-OHdG levels than their counterparts on d2.

3.7. The additional role of pyruvate as antioxidant in cell culture medium

The data presented in sections 3.3. and 3.4. show that UVA irradiation induces changes in the metabolism of human fibroblasts. It increases the consumption of metabolites involved in antioxidative defence mechanisms like cystine and serine

(participating in the glutathione metabolism) (125, 126), but also promotes the release of compounds that promote ROS-detoxication into the medium like alanine (127).

Probably one of the most important compounds showing UVA-induced regulation is pyruvate (Fig. 26 and Fig. 31). Pyruvate is an important additive in cell culture and part of many commonly used culturing mediums. Its main purpose is as an additional source of carbon for the cells together with glucose but studies have shown that it can also function as a quencher for reactive oxygen species. It has been published that pyruvate can be non-enzymatically decarboxylated to acetate in the presence of ROS. In 1987 O'Donnell-Tormey and associates have shown that equimolar amounts of pyruvate and hydrogen peroxide (H_2O_2) neutralized each other (85). The end product of this reaction is acetate (87).

This process was confirmed in the experiment depicted in Fig. 39. A For the experiment, 100µM sodium pyruvate was mixed with 100µM of H_2O_2 in water. The concentration of 100µM pyruvate was chosen for several reasons. First, according to laboratory data, the range of blood pyruvate in humans can vary between approximately 50µM and120 µM depending on the glucose uptake and body-type (118). In order to replicate the experiment of O'Donnell-Tormey et al. equimolar amounts of pyruvate and H_2O_2 had to be used. The production of acetate was then detected by 1D-NMR (see Fig. 39. A). In untreated samples, there is almost no acetate detectable. With the addition of H_2O_2, the acetate content of the samples rises and the pyruvate amount decreases, leading to 1:1 pyruvate to acetate ratio.

To test whether this enzymatic decarboxylation can be also applied in UVA irradiated samples, 100µM sodium pyruvate in water were irradiated 6 x 6 J/cm^2. The results are shown in Fig. 39. B. Two days of UVA irradiation leads to degradation of pyruvate and the release of acetate. Initially before treatment, almost no acetate could be detected, similar to the data seen in Fig. 39. A. After irradiation, the ratio of pyruvate to acetate is approximately 2:1, which deviates from the 1:1 ratio observed in the H_2O_2 treatment.

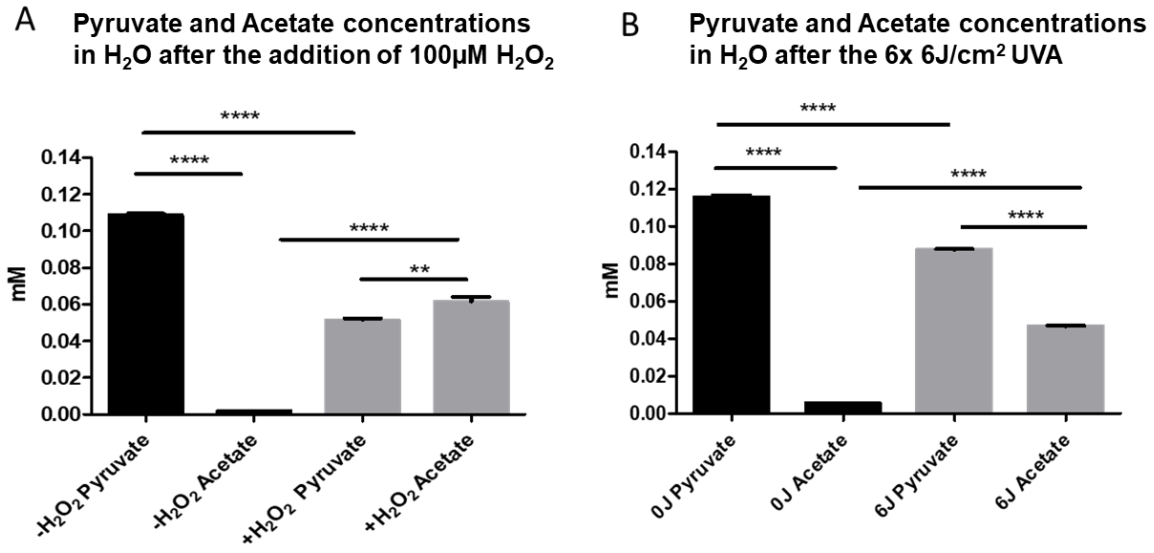

Fig. 39: Non-enzymatic decarboxylation of pyruvate (100µM initial concentration) to acetate in the presence of ROS. (A) NMR-data of water samples containing equimolar amounts of pyruvate and H_2O_2 (100µM each). After the addition of H_2O_2, the pyruvate concentration dropped down by 50% and an increase in acetate concentration is observed. The increase in acetate roughly matches the pyruvate decrease. (B) NMR-data of water samples after 2d of UVA irradiation. Similar to the H_2O_2 treated samples, irradiation results in decrease of pyruvate levels (initial concentration 100µM) and increase of acetate concentration compared to untreated controls. ((n=3), Statistical analysis: Two-way ANOVA with Bonferroni's multiple comparison test. For significances: (****) P < 0.0001).

The experiment shown above elaborates on the potential of UVA to non-enzymatically decarboxylate pyruvate to acetate. This could potentially have an influence on different cellular processes, including metabolism, since the presence of pyruvate in the cell culture medium could potentially influence the cells' reaction to irradiation. Since the *in vitro* experiments described further below were performed in the complex environment of a cell culture medium, it was of interest to see the behaviour of pyruvate and acetate in regular DMEM (1mM pyruvate and 10 % inactivated FCS).

The complete DMEM medium was irradiated without cells for two days (6 x 6 J/cm^2). The samples were then collected and measured 1D-NMR-CPMG without filtering the serum proteins beforehand. As seen in Fig. 40, **Fehler! Verweisquelle konnte nicht gefunden werden.**the amount of measured acetate almost doubles compared to the untreated samples. The levels of pyruvate also drop down to half of their initial value after receiving UVA treatment. What is interesting is that, compared to the data in Fig. 39, the amount of acetate at the end of irradiation is significantly more than the pyruvate remaining.

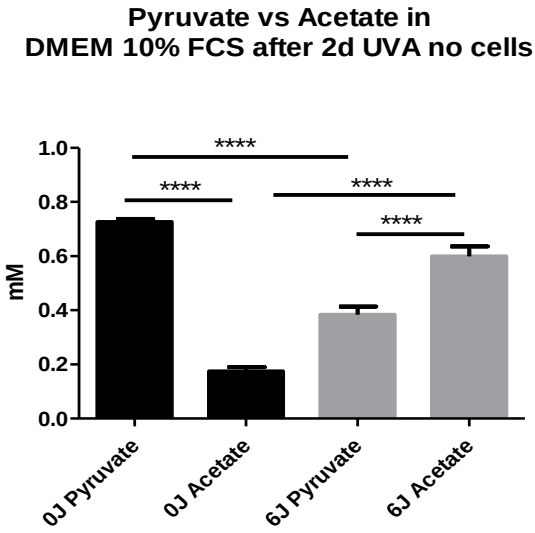

Fig. 40: NMR-data of medium samples containing 1mM Na-Pyruvate after UVA treatment. Shown are data for the concentrations of pyruvate and acetate in the tested medium samples before irradiation (0J) and after 2d of UVA irradiation (6J). Acetate levels increase after irradiation compared to a decrease in pyruvate. ((n=3), Statistical analysis: Two-way ANOVA with Bonferroni's multiple comparison test. For significances: (***) P < 0.0005; (****) P < 0.0001).

All the data above strongly imply that the pyruvate contained in cell culture medium can react with ROS. Since it is known that UVA can induce ROS and there are publications showing that pyruvate has the qualities of an antioxidant, it would be crucial to determine its influence on cell metabolism during irradiation. This is above all important, since many cell culture media contain high amounts of pyruvate (for example DMEM contains 1mM pyruvate) which is a deviation of the natural abundance of pyruvate in blood which is between 50µM and 120µM (118).

The following experiments aim to determine what the influence of pyruvate in the cell culture is compared to an experimental setup closer to the natural abundance of pyruvate in the human skin. Since the skin and blood levels of pyruvate overlap (128) and cells in culture are able to reach pyruvate equilibrium close to measured blood values (85), all following experiments were performed with either 1mM or 0mM pyruvate. This was supposed to establish whether the lower amounts of pyruvate in the skin compared to cell culture result in more severe cellular damage and disruption of diverse metabolic pathways, including but not limited to glucose metabolism.

3.8. Pyruvate as an antioxidant in UVA-irradiated cells

The data presented inn 3.7 prove that pyruvate is able to be converted nonenzymatically to acetate in the presence of ROS (H_2O_2) or a ROS-inducer such as

UVA. However, to definitely prove the role of pyruvate as a ROS-quencher in the presence of UVA, the ability of this metabolite to directly scavenge ROS during cell irradiation was tested by implementing a DCFDA-ROS-detection assay. Furthermore, an assay for the UVA-induced base modification 8-hydroxydeoxyguanosine (8-OHdG) was performed in order to test the ability of pyruvate to prevent UVA-mediated DNA damage. The acquired data were then compared to the results shown in Fig. 37 and Fig. 38 and presented in Fig. 41 and Fig. 42 respectively.

3.8.1. Pyruvate acts as UVA-induced ROS-quencher in fibroblasts

To determine whether Pyruvate can act as ROS quencher in the cell culture, Re5 fibroblasts were pre-incubated for 2 days in medium containing 0mM or 1mM sodium pyruvate and subsequently stained with DCFDA in accordance with 2.3.12.

Presented in Fig. 41 are the results from the ROS-measurements. Even in the absence of irradiation, the amount of ROS in the samples without pyruvate is significantly higher than the corresponding controls with pyruvate. The ROS levels again rise with irradiation compared to un-irradiated samples. The ROS in the irradiated samples without pyruvate is almost double the one in samples with 1 mM pyruvate.

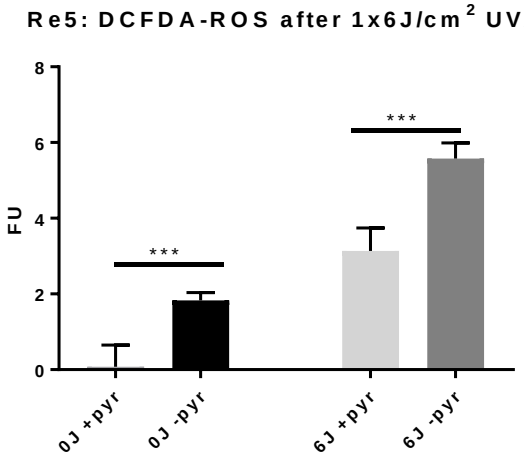

Fig. 41: Influence of pyruvate on ROS-production in cells irradiated with UVA measured by DCFDA-ROS-detection assay. The staining was performed directly before the start of UVA-application and the ROS detection was conducted one hour after irradiation (n=3, Statistical analysis: Two-way ANOVA with Bonferroni's multiple comparison test. (***) P < 0.0005).

3.8.2. Pyruvate and its influence on 8-OHdG formation

Since it was proven that pyruvate reduces ROS levels in the presence of UVA (Fig. 41), it was important to see whether it has direct protective effects on the cells. It is known from published data that UVA irradiation can cause DNA mutations through modifying guanosine to 8-hydroxydeoxyguanosine (8-OHdG). Using the method described in 2.3.14., cells cultured with and without pyruvate were irradiated for 2d and 4d and the generation of 8-OHdG in these samples was measured.

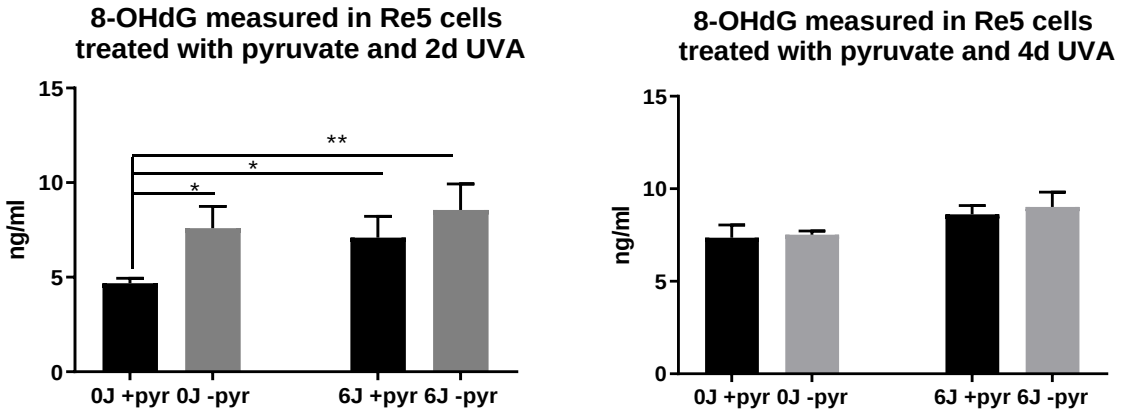

Fig. 42: Influence of pyruvate on DNA-damage in cells irradiated with UVA. The presence of pyruvate tends to reduce the amount of ROS in the 2d treatment but has no significant effects during long-term irradiation (4d). (n=4, Statistical analysis: Two-way ANOVA with Bonferroni's multiple comparison test. For significances: (ns) P > 0.05; (*) P < 0.05; (**) P < 0.005).

As shown in Fig. 42, the absence of pyruvate results in significantly increased 8-OHdG levels in 0J samples after 2d of treatment. Two days of UVA irradiation also show increase in DNA damage in 6J samples without pyruvate compared to the ones containing 1mM pyruvate. Interestingly, the 0J –pyr samples showed an almost equal amount of 8-OHdG as the 6J –pyr samples after 2d of treatment.

As for the data obtained after 4d of UVA irradiation, it seems that the 8-OHdG levels have reached a plateau. There was no difference between cells treated with and without pyruvate but irradiated cells still retain the tendency to have more DNA-damage than their un-irradiated counterparts.

3.9. Treating fibroblasts with UVA and pyruvate influences not only ROS production cell metabolism, but also the expression of key matrix metalloproteinases

The results from the preceding experiments have shown that UVA has adverse effects on human cells, generating reactive oxygen species that can lead to damaging DNA modifications such as 8-OHdG. In addition to that, UVA changes the metabolism of irradiated human fibroblasts. The presence of pyruvate in the culture medium at levels 10-times higher than physiological reduces the detrimental effects of UVA irradiation. Following up from this, it was interesting to see whether the presence of pyruvate in the cell culture changes another crucial parameter influenced by UVA – MMP expression.

MMPs are amongst the crucial players involved in both photoaging and tumor progression (15, 129). To test whether pyruvate can modulate MMP expression in the context of UVA irradiation, human fibroblasts Re5 were treated using standard irradiation protocol (see 2.3.5.). Following that, the cells were trypsinized, counted, and collected for RNA isolation as described in 2.3.10. The amount of total RNA extracted was measured by Nanodrop and 500 ng per sample were used for reverse transcription (see 2.3.11.). Afterward, a qPCR with a ROCHE Sybr-Green system was performed in accordance with 2.3.11. to determine the changes occurring in MMP expression after treatment. The expression of the genes of interest (MMPs and TIMP1) was normalized to the expression of the housekeeper b-Actin and the data is presented below as ratio to the housekeeper.

Fig. 43 shows that not only UVA irradiation, but also pyruvate treatment, can modulate the mRNA expression of MMP1 and MMP3. No significant difference was observed between pyruvate-treated and untreated cells without UVA for both MMP1 and MMP3. Contrary to already published data (60, 130, 131) MMP1 and MMP3 did not show a significant increase after UVA irradiation if the samples were treated with 1 mM pyruvate. The absence of pyruvate in the medium significantly increased their mRNA expression by at least two-fold compared to the corresponding UVA-samples with pyruvate.

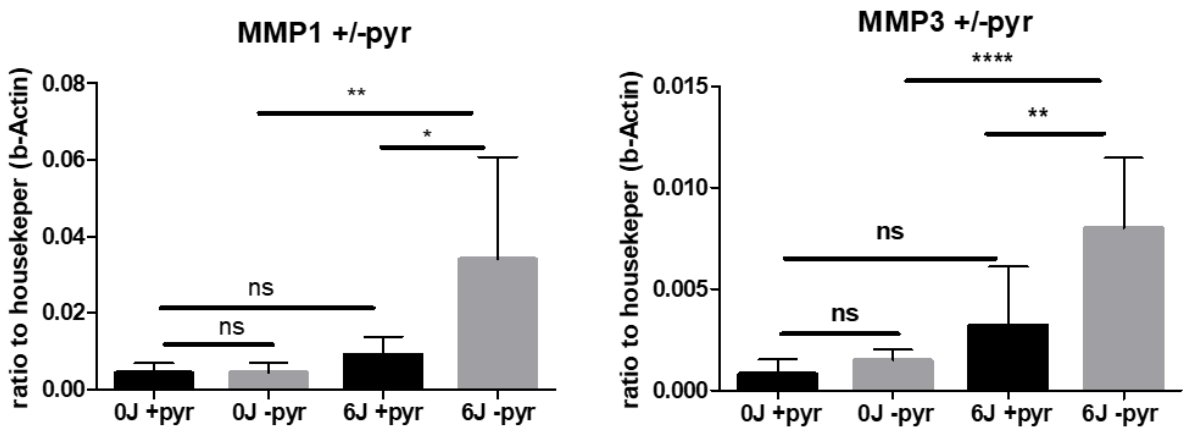

Fig. 43: Changes in MMP1 and MMP3 expression after 4d UVA-irradiation in cells cultured wit 1 mM or 0 mM pyruvate. Increase in gene expression was observed for both genes in 0 mM Pyruvate samples after irradiation. ((n=3), Statistical analysis: Two-way ANOVA with Bonferroni's multiple comparison test. For significances: (ns) P > 0.05; (*) P < 0.05; (**) P < 0.005; (***) P < 0.0005; (****) P < 0.0001).

From the other MMPs tested, none showed pyruvate-dependant expression changes. There was no difference between treatments in the expression of MMP9 and MMP13 (as shown in Fig. 45). After the UVA-irradiation MMP2 and MMP15, as depicted in Fig. 44, had significantly elevated mRNA levels compared to un-irradiated controls. There were no differences in expression between cells cultured with pyruvate and the ones without, independent of the irradiation received. Still, there was a tendency for increased mRNA levels in irradiated samples not treated with pyruvate.

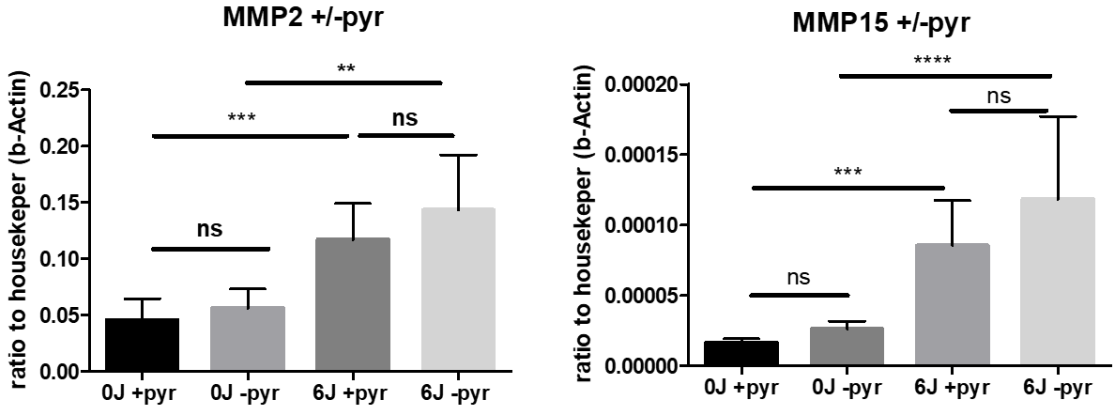

Fig. 44: Changes in MMP2 and MMP15 expression after 4d UVA-irradiation in cells cultured wit 1 mM/0 mM pyruvate. Despite there being a tendency that 0 mM pyruvate enhances gene expression the changes in the mRNA levels were not significantly influenced by the presence of pyruvate in the medium. ((n=3), Statistical analysis: Two-way ANOVA with Bonferroni's multiple comparison test. For significances: (ns) P > 0.05; (*) P < 0.05; (**) P < 0.005; (***) P < 0.0005; (****) P < 0.0001).

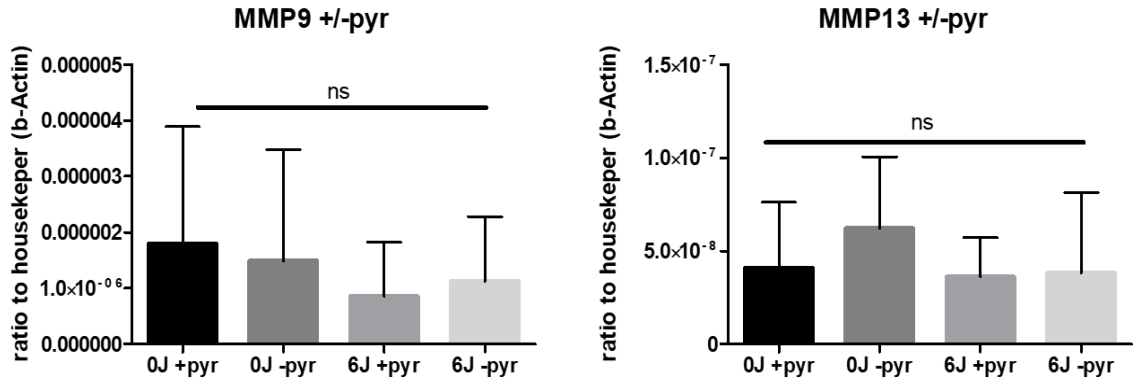

Fig. 45: Changes in mRNA expression of MMP9 and MMP13 after irradiation in cells cultured with 1 mM/0 mM pyruvate. No significant changes were observed after irradiation and pyruvate treatment. The mRNA levels detected were extremely low. (Statistical analysis Two-way ANOVA with Bonferroni's multiple comparison test. For significances: (ns) P > 0.05).

Besides the MMP-expression the changes in TIMP1, a metalloproteinase inhibitor, were also tested. According to previously published data by Hantke et al. (132) TIMP1 expression should decrease with an increase in MMP expression. However, as seen in Fig. 46, Re5 fibroblasts repeatedly irradiated with 6J/cm^2 UVA showed an increase in TIMP1 compared to un-irradiated controls. Despite pyruvate having no significant influence on the TIMP1 expression, there was a tendency for higher mRNA levels in samples cultured without pyruvate.

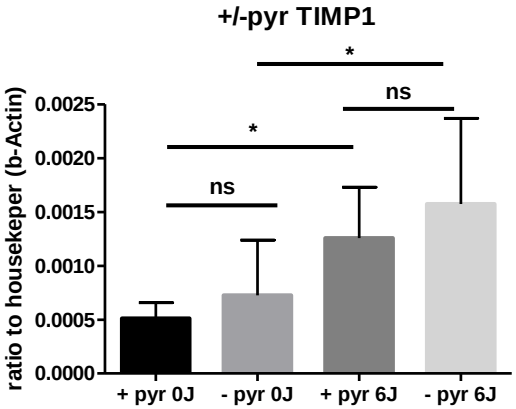

Fig. 46: Changes in TIMP1 expression after 4d UVA-irradiation in cells cultured wit 1 mM pyruvate or without pyruvate. ((n=3), Statistical analysis: Two-way ANOVA with Bonferroni's multiple comparison test. For significances: (ns) P > 0.05; (*) P < 0.05).

4. Discussion

The aim of this work was to investigate the influences of UVA irradiation on the metabolism of non-malignant skin cells, with emphasis on fibroblast metabolism. It provides new evidence for the importance of pyruvate, a compound widely present in different types of cell culture medium and a known antioxidant, in modulating not only cell metabolism during UVA irradiation, but also in eliciting changes in MMP expression. Table 16 summarizes the effects of UVA and pyruvate in human fibroblasts observed in this work. Furthermore, this work provides a metabolic comparison between cell culture (monolayer) and skin cultured *ex vivo* (complex, multi-layered structure), which is crucial in order to establish the potential for data transferability between the two systems.

Table 16: UVA and pyruvate influence on different cellular processes.

Process	**-Pyruvate**	**UVA**	**UVA -Pyruvate** (compared to UVA)
Cell viability	**No**	**No**	**No**
Cell proliferation	**No**	**Yes**; ↓	**Yes**; (same as UVA)
Cell morphology	**No**	**Yes**	**Yes** (same as UVA)
Glucose/ Lactate metabolism	**Yes**; glucose consumption ↑, lactate – not significant	**Yes**; glucose consumption/lactate production ↑	**Yes**; glucose consumption ↑, lactate - not significant
Other metabolic changes	Glutamate/ pyroglutamate (not significant)	Glutamate/ pyroglutamate ↑	Glutamate/ pyroglutamate ↑↑
	Acetate ↓, alanine (not significant)	Acetate/alanine ↑	Acetate/alanine ↓
	Cystine (not significant)	Cystine ↑	Cystine ↓
ROS	**Yes**; ↑	**Yes**; ↑	**Yes**; ↑↑
DNA damage (8-OHdG)	**Yes**; ↑	**Yes**; ↑	**No**; tendency of increase (not significant)
MMP expression	**No**	MMP2/15 ↑	MMP1/3 ↑
TIMP 1 expression	**No**; tendency of increase (not significant)	**Yes**; ↑	**No**; tendency of increase (not significant)

4.1. Changes in morphology and proliferation of human skin cells after UVA irradiation treatment

Repeated irradiation of non-malignant cells with repetitive sub-erythemal doses of UVA (109) resulted in morphologic changes in the irradiated population compared to the untreated control in both human and murine fibroblasts. These usually spindle-like cells became rounded (NIH 3T3; Fig. 17) or slightly elongated (Re5 and to a lesser extend WT01; Fig. 19). There have been publications on the capability of UVA to regulate the expression of cytoskeletal proteins (115, 133), which is most likely the cause of this phenomenon.

The morphologic changes of human fibroblasts seen in 3.1.3. are in accordance with the observations made by Yamaba and associates in 2016 (115), where they show that UVA-irradiated fibroblasts have changes in morphology due to disturbance of actin elongation and polymerization. On the other hand, human keratinocytes HEKa were slightly more rounded after irradiation compared to their untreated counterparts. The cells seemed to increase in size, probably due to cytoskeletal changes similar to the ones reported in fibroblasts. Since there is a strong connection between cell shape and function (134, 135), changes in cell morphology are likely to result in functional disturbances, such as impaired collagen production, and result, on a macroscopic level, in ECM-modifications and photoaging (115).

The most likely reason for the cytoskeletal re-modelling occurring after UVA irradiation was connected to the production of ROS. The data collected from human fibroblasts Re5 showed that even a single dose of UVA (6J/cm^2) is enough to generate four times more ROS than in un-irradiated controls (Fig. 37). ROS is known to influence the actin component of the cytoskeleton (136) so it was logical to assume that this is also the case in these experiments. However, the data obtained from cells cultured without pyruvate contradict this theory. The presence of pyruvate in the cell culture medium has been shown to have ROS-scavenging properties not only in published literature (85), but also in the experiments performed for this work (Fig. 39, Fig. 40, and Fig. 41). The absence of pyruvate from the cell culture medium lead to increase in ROS production in both UVA irradiated and un-irradiated cells (Fig. 41). Subsequently, it was expected that this would result in even greater morphological changes. However, the morphology of the cells did not change drastically from the absence of pyruvate in the medium (Fig. 22). This leads to two possible conclusions. Either pyruvate alone is

not enough to protect the cytoskeletal structures from ROS, or UVA exerts direct effects on the cytoskeleton without the involvement of ROS. Considering the later possibility, there is data indicating that cellular proteins are capable of absorbing UVA directly, thus supporting the theory of an UVA-mediated ROS-independent cytoskeletal deformation (137, 138).

To be able to further elaborate on the observed morphologic discrepancies between different cell types, as well as the role of UVA and pyruvate on cytoskeletal modifications, the expression of cytoskeletal proteins such as actin and tubulin, but also of actin-modulating proteins like cofilin or formin (139) with and without UVA irradiation and different anti-oxidant treatments should be performed.

In addition to changes in morphology, the treatment of cells with UVA resulted mostly in proliferation retardation but not in a decrease of cell-viability (Table 11). This proliferation retardation was probably due to UVA inflicting DNA and other cellular damage. It has been well studied that cells stop their proliferation to repair damaged DNA in order to prevent passing down mutations to the daughter cells (140). Seeing as the cells continue their proliferation, albeit slower, it is evident that the inflicted damage is enough to elicit a proliferation delay but not complete cycle arrest.

The absence of pyruvate from the medium did seem to slightly increase the overall doubling times of human fibroblasts Re5 but the doubling time ratio of 6J to 0J treatments remained unchanged (Table 13). This overall retardation in proliferation can be explained with the intended application of pyruvate as an additive to the cell culture. In the context of medium composition, the main role of pyruvate is as an additional source of carbon for the cell's energy metabolism (119). It is to be expected that after removing pyruvate from the medium formulation, the cells would experience proliferation retardation due to being presented with one less source of energy.

It seems that pyruvate, although having antioxidant capabilities, is unable to rescue irradiated fibroblasts neither on morphological nor on proliferative level.

4.2. Changes in glucose metabolism of healthy skin cells and skin explants after UVA irradiation

Despite having on influence on cell viability, the data presented in 3.1 show clearly that UVA influences the glucose metabolism of fibroblasts, keratinocytes, and

melanocytes of both human and murine origin. Irradiation of the cells leads to an increase in glucose consumption and lactate production, compared to untreated controls. This finding is important since there has been no comprehensive study of the metabolic reactions of non-malignant skin cells to irradiation. In 2014 Marionnet et al. published an article showing an increase of glucose-metabolism-related genes in UVA1 irradiated keratinocytes but, contrary to the findings of this work, saw no changes in glucose metabolism relevant genes in fibroblasts (80). Furthermore, the UVA doses used in this publication were considerably higher than the chronic low UVA-exposure used in experimental setups of the current work (single irradiation dose of 20-40J/cm^2 (80) compared to 6J/cm^2 per irradiation and a maximum of 18J/cm^2 per day for the current experiments). Also, the single doses used by Marionnet et al. were almost equal or even greater than the pathologic minimal erythema dose measured for UVA (109) compared to sub-erythema doses used in this work. It could be argued that results obtained under pathologic conditions can be hardly representative of the typical metabolic profile after moderate sun exposure.

4.2.1. UVA influences glucose metabolism independent of cell type and donor species

The behaviour of non-malignant cells after UVA application observed in this work closely correlates to the one described by Kamenish et al. in 2016 for malignant cells (53). Initially, it was expected that the UVA-induced changes in glucose metabolism are specific only for skin tumor cells, but the findings described in this work provide better understanding on cellular behaviour after irradiation.

A molar conversion of glucose to lactate of 1:2 is typical for tumor cells and is the result of aerobic glycolysis. The process was first described by Otto Warburg in 1927, gaining the name Warburg Effect (72). It was interesting to see whether non-malignant cells that have shown increase in glucose metabolism post-irradiation, tend to exhibit Warburg-like glucose-to-lactate conversion after UVA treatment. From all tested cells, the human fibroblasts Re5 had a ratio closest to the expected glucose to lactate conversion of 1:2 (lactate-to-glucose ratio of 1.7), followed by the human keratinocytes HEKa (ratio of 1.5) (see Table 12). The rest of the tested cells had lactate-to-glucose ratio of 1 or below. It seems that cells that show Warburg-like lactate-to-glucose ratios (Re5, HEKa) are predisposed to such type of metabolism even without irradiation and the application of UVA results only in more pronounced metabolic effects without

shifting the glucose to lactate balance. This is in line with the observation that the Warburg effect is often associated with high proliferation in tumor cells and in UVA irradiated non-malignant cells, the proliferation rate was decreased. Therefore, it is likely that the increased glucose metabolism in non-malignant cells occurs for different reasons than proliferation. The observed increase of glucose consumption and lactate production can thus be connected to increased metabolism as means to prevent and/or repair occurring cellular damage rather than being indicative of proliferation. This theory is in accordance with the observations of Lemons et al. showing that quiescent fibroblasts have similar metabolic rates to fast proliferating ones (141). The explanation for such behavior is that the quiescent cells maintain an active PPP to produce NADPH but do not require nucleic acid synthesis (142). Instead, the NADPH is implemented in the redox defense or fatty acid synthesis (141). Indeed, the uniform reaction to UVA radiation shown by different types of skin cells from different species, coupled with the fact that lactate alongside pyruvate has been suggested as an antioxidant (84), strongly indicates that the observed metabolic changes are connected to combating UVA-induced oxidative damages.

Seeing that UVA induces changes in the lactate metabolism, a logical question would be why such metabolic change occurs and what could its benefits or adverse effects be. The results listed in 3.6 show that UVA treatment of Human fibroblasts Re5 resulted in the generation of ROS. The increase of harmful reactive molecules could explain the elevated lactate concentration post irradiation observed in the colorimetric metabolic profile and the labelling experiments, as lactate is suggested to possess antioxidant properties (82, 83).

In addition to its antioxidant capabilities, this glycolysis product has been known to fulfil other roles in the skin. On one side, lactate, or rather lactic acid, improves the barrier function (143) and the turnover of the skin (144), and has antibacterial properties by decreasing skin pH (145). On the other side, lactate has another function, namely immunosuppression (78, 146, 147). In the context of tumor cells, lactic acid has been shown to attenuate T-cell responses via hindering their lactate transport and thus resulting, amongst other things, in disturbance of T-cell metabolism and function (77, 78, 148). As such, increased lactate secretion in non-malignant cells can be seen as evidence for the importance of the skin-tumor microenvironment as a co-player in the tumor-mediated immune evasion. However, speaking of the tumor

microenvironment, it should be noted that the cells inhabiting it are not the same as regular cells from the surrounding tissue. There have been many studies on the topic of fibroblast-modification by the tumor, turning them into cancer-associated fibroblasts (149, 150). So logically, a change of glucose metabolism similar to cancer in cells residing in the tumor stroma should not be that surprising. However, none of the cells in this study were derived from tumor stroma. It could be argued that NIH 3T3, being an immortalized cell line (151), have characteristics closer to cancer cells. Although true in this particular case, all other cells used were primary cells, and in the case of mKera even freshly isolated specifically for the irradiation experiment.

Nevertheless, the immune attenuation provided by lactate is not always a negative thing. In healthy skin, suppressing the immune system could be beneficial in order to prevent unwanted immune responses like skin photosensitivity observed in patients with auto-immune diseases (152). Indeed, it has been shown that UV radiation, especially UVB, can induce systemic immunosuppression (153, 154), which is in accordance with such a hypothesis. In addition to this, in 1999 Iwao and associates showed that the immune response attenuation after UV-irradiation is, at least, partially due to the generation of ROS (58). This might seem contradictory since it was mentioned earlier that lactate can act as an antioxidant itself (82), so increased lactate secretion should reduce ROS levels. However, there are some critical points when considering lactate as a viable antioxidant option for the cells as it is able to generate ROS itself and activate ECM degradation (91-93, 146). In their publication, Bassenge and associates show that increased lactate levels in guinea pig hearts lead to increased ROS levels (91). Another more recent work from Tauffenberger et al. also shows linear correlation between increasing lactate concentrations and increasing ROS levels (92).

When discussing glucose and lactate metabolism in the context of UVA, ROS-generation, and antioxidant defence, the role of pyruvate as a medium additive must be considered, since it too possesses antioxidant properties (85, 89, 91). Despite not influencing cell viability, morphology, or proliferation when absent from the medium, pyruvate, as an intermediary product of aerobic glycolysis (155), could influence the metabolic profile of irradiated cells. In this work, it was observed that the absence of pyruvate from the culture medium increases glucose consumption with and without UVA. As for lactate release, there was a statistically significant increase after removing

pyruvate from the medium for both irradiated and un-irradiated samples, with the largest difference being detected in the un-irradiated pair (+/-pyruvate). It is possible that lactate, as mentioned before, plays some role as an antioxidant. However, it is also possible that the cells expel excess lactate in order to reduce the amount of ROS-generating molecules in the cytoplasm (91).

4.2.2. No changes in glucose and lactate metabolism detected in murine skin after irradiation

Since lactate plays such an important role in the skin during UV-irradiation, it was expected that metabolic changes would also be detected in the medium of irradiated skin samples.

Compared to a cell monolayer, the metabolic data for the skin explants shown in Fig. 32 and Fig. 35 present a different picture with regard to glucose consumption and lactate production, mainly, glucose and lactate levels did not change between irradiated and un-irradiated states. There are two possible explanations for this occurrence.

Firstly, it is possible that two days of irradiation were not enough to induce any changes in the glucose consumption of the skin samples. The second explanation is that the skin explants are attempting to modulate the lactate concentration in the medium to reach typical blood values and thus regulate also their glucose metabolism. As shown in previously published data, mice have high blood lactate values of 4.5-4.6mM (156). This amount closely correlates with the amount of lactate released in the medium by skin explants (Fig. 32 and Fig. 35). From these figures, it is also evident that almost all of the consumed glucose is converted to lactate. Therefore, it is possible that in skin explants the establishment of a blood-like extracellular lactate levels takes precedent before any UVA-related metabolic rearrangements. Still, since there are differences between plasma/medium concentrations of lactate and interstitial fluid levels (157-159), the lactate amount in the skin itself with and without UVA irradiation needs to be examined.

4.2.3. ^{13}C-labelling in human fibroblasts shows that only alanine, acetate, and lactate are derived from glucose/pyruvate

Considering the importance of glucose and lactate not only for the cell energy metabolism but also for the skin homeostasis and barrier function (143, 144), it was interesting to see the metabolic data from the ^{13}C-labelling experiment with glucose. Furthermore, pyruvate as a cell culture additive and intermediary product of glycolysis (155), as well as an antioxidant (85, 89, 91), was also labelled in order to detect its derivate metabolites.

It should be noted here that the absolute values for glucose and lactate detected during the labelling experiments, and later during the NMR-profiling of unlabelled samples, deviated from the ones obtained in the colorimetric measurements. The colorimetric data presented in section 3.1.3 show glucose uptake and lactate release for Re5 fibroblasts at levels almost two times higher than the ones observed in the NMR-measurements. This occurrence is due to the presence of proteins in the culturing medium in the form of FCS. Metabolites like glucose and lactate are known to bind to serum proteins (160, 161). Protein-bound metabolites are hard to detect by NMR and therefore the total yield for glucose and lactate differs between the colorimetric detection (where proteins contain in the medium play no role) and NMR. Since glucose and lactate also have different binding affinities to proteins (160, 161), it also explains why the lactate-to-glucose ratios for Re5 differ between the colorimetric and the NMR measurements (ratios of 1.7 and 1.4 respectively, see Fig. 21 and Fig. 28).

The data from the labelling experiments showed that acetate, alanine, and lactate are derived from pyruvate. As for the glucose treatment, it resulted in labelled acetate, alanine, lactate, and pyruvate. This is in accordance with the available data for compounds involved in the glycolytic pathway of glucose metabolization (126). The distribution of labelled glucose explains the observation that, in the absence of pyruvate the, cells release insignificantly higher amounts of lactate after irradiation compared to irradiated samples with pyruvate even under increased glucose consumption – the glucose derived pyruvate is not metabolized solely to lactate but also contributes to alanine and acetate synthesis.

An important point to note is that there were no labelled metabolites detected who were part of the Pentose Phosphate Pathway (PPP) or Citrate cycle (126). This leads to the conclusion that the glucose resources, and pyruvate as an additional source of carbon, when present in the medium, are not utilized in respiration (162) or DNA-synthesis/repair (163, 164).

Another interesting finding from the labelling experiments is the consumption-secretion dynamic of pyruvate. Cells cultured with pyruvate consumed it from the medium. At the same time, they released some glucose-derived pyruvate in the extracellular milieu, which is in accordance with the findings of O'Donnell-Tormey (85). Combining this with the data from the metabolic profiling of the Re5 cells (see Fig. 28) shows that cells cultured in the presence of pyruvate have both higher consumption and release rates of the metabolite after irradiation. The observed higher pyruvate production than detected consumption is most likely an artefact, especially when compared with the secretion data obtained from the ^{13}C-glucose labelling without pyruvate. The detected secretion in the presence of pyruvate is almost ten times higher than the one observed in medium without pyruvate. However, it is likely that the high amounts of unlabelled compound contained in the standard DMEM formulation (1mM) enhance the labelling readout and give falsely increased secretion levels.

As for the fact that cells treated with 1mM ^{13}C-pyruvate have higher uptake of the compound compared to ones cultured in 1mM unlabelled pyruvate. This could be a combination of a measurement and calculation artefact, since the difference in the HSQC signals for unlabelled pyruvate in the medium and cell supernatant (which were used for calculating the concentration of labelled samples), was very small. The low natural abundance of ^{13}C atoms could lead to reduced sensitivity of the HSQC measurement for unlabelled pyruvate (95), and subsequently result in inaccuracy while calculating the labelled pyruvate concentration. However, there are also some indications that some isotopic ions and molecules with higher molecular mass have faster diffusion rates than their lighter counterparts (165). This, coupled with the high extracellular concentration of the metabolite might have resulted in an increase in uptake (166).

It should be noted that the levels of pyruvate present in the cell culture medium (1mM) are much higher than the ones usually detected in blood (between 50µM and 120µM) (118). However, UV radiation is capable of increasing blood flow into the skin

(167), leading in turn to a local increase in pyruvate concentration (168). Therefore, it is possible that skin pyruvate levels have a drastic local increase and reach levels much higher than the ones usually detected in the blood and not so far from the 1mM medium additive used in the cell and skin experiments.

As for the fibroblasts kept in the absence of pyruvate, only about a half to a third of the detected pyruvate production came from glucose (see Fig. 26). This is indicative of alternative sources for pyruvate synthesis, such as glutamine, and more exactly its derivative PEP (126).

The observed pyruvate dynamic in cell culture can be explained with its suggested role in the skin. Pyruvate was shown to have antioxidant properties by being able to non-enzymatically decarboxylase to acetate (85, 89), a reaction also supported by findings in this work (Fig. 31, Fig. 39, and Fig. 40).

When observing murine skin punches cultured in medium containing un-physiological concentrations of 1mM pyruvate or 200µM , which is closer to the blood values detected in murine blood (120, 121), the detected metabolic profile of pyruvate was very different from the one seen in cell culture (Table 15). In the case of samples cultured in DMEM with 1mM pyruvate, the uptake of pyruvate by the skin explants significantly decreased after irradiation. If the phenomenon was connected to a blockage of the monocarboxylate transporter (MCT) due to the strong medium acidification by the high extracellular lactate release (169) there should not have been a difference between irradiated and un-irradiated samples, since lactate levels remained unchanged in skin explants before and after irradiation. However, it is possible that the net pyruvate consumption is influenced by the pyruvate release from the skin sample. As seen in Fig. 35, skin explants, much like cell culture fibroblasts, are capable of releasing pyruvate into the medium. Since changes in the glucose consumption ratios have not been detected in the medium, it is likely that the glucose used for pyruvate production comes from reserves in the interstitium (170).

Acetate is another important metabolite, a product of the non-enzymatic decarboxylation of pyruvate in the presence of ROS (87). It shows labelling from both glucose and pyruvate. When adding up the labelled values it is evident that the two aforementioned metabolites are not the only sources of acetate. An alternative source could be newly-synthesized alanine that is being converted to pyruvate and afterward,

to acetate via alanine transaminase (171) or serine-derived pyruvate via serine dehydratase (146).

What remains the same between cell culture and skin explants (1mM pyruvate) is that irradiation induces an increase in acetate release (Table 15) which can be seen as an indicator of ROS detoxification. Contrary to that, the release of acetate by skin reconstructs cultured in 200µM pyruvate-medium decreased after irradiation. There are two possible explanations for this observation. Firstly, it is possible that not all of the pyruvate is used for non-enzymatic decarboxylation and subsequent acetate production. Pyruvate can also be used for the synthesis of alanine – another possible antioxidant (126, 127). However, alanine release also decreases after irradiation (Fig. 35). Off course, it is possible that alanine is retained in the skin to facilitate antioxidant defense there and remain trapped in the interstitium instead of being released in the medium. Secondly, it is also possible that acetate is being retained in the skin or even re-absorbed in the tissue to serve as a source of Acetyl-CoA (172) in order to fuel the tissue energy metabolism and subsequent initiation of other ROS-detoxification pathways.

As mentioned, alanine is another metabolite that was detected during the labelling experiments. It also seems to be completely derived from glucose and pyruvate in medium containing 1mM pyruvate as evident from the labelling experiments. In the absence of pyruvate, glucose does not seem to be the sole source of alanine. It is possible that alanine has been synthesized via other pathways, for example via tryptophan (126).

Alanine metabolism also showed pyruvate-dependant changes when cells containing 1mM or 0mM pyruvate are subjected to UVA-irradiation. Alanine production significantly decreases in cells irradiated in the absence of pyruvate. Comparing cell culture with *ex vivo skin*, the skin samples showed decrease of alanine release after irradiation independent of pyruvate concentrations. It is possible that the metabolite remains trapped in the interstitium or the cells themselves. There have been suggestions that alanine itself can function as an antioxidant by stimulating the expression of antioxidant defence proteins like oxygenase-1 and ferritin (127), which could explain its retention into the cell when not enough pyruvate is present in the medium.

4.3. Other metabolites showing UVA and pyruvate dependant regulation in cell culture and mouse skin

Besides the glycolytic metabolites described in the labelling experiments, other compounds involved in energy metabolism and ROS-detoxification were also detected to be regulated by irradiation and variations of pyruvate concentration. The whole spectrum of detected compounds and their interactions are shown in Fig. 47.

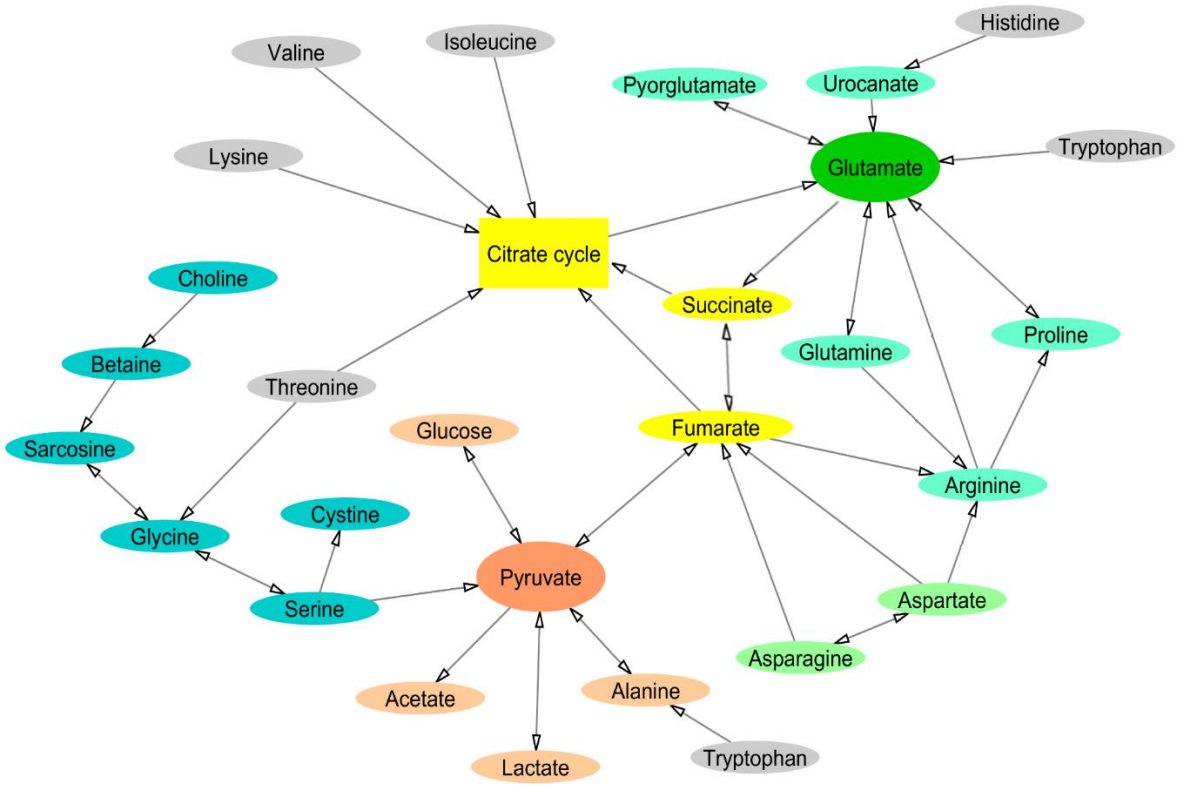

Fig. 47.: Interaction map of the detected metabolites made according to publicly available data in the Human Metabolome Database and KEGG (126, 171). Marked gray are essential amino acids that come from the culture medium. The choline-cystine pathway (marked blue), represents metabolites involved in the glutathione synthesis. Marked orange are metabolites participating in glycolysis or derived from pyruvate. Yellow metabolites are crucial players in the citrate cycle. Marked blue-green are metabolites involved in glutamate metabolism.

4.3.1. Glutathione metabolites – cystine, glutamine, glutamate, pyroglutamate

From all metabolites, cystine, a dimer of the amino acid cysteine, was uniformly regulated between cell culture and skin samples with UVA treatment increasing its

consumption. The lack of pyruvate, at least in cell culture, seems to negatively influence the metabolite consumption from the medium.

Cystine, together with glutamate, is metabolized to γ-glutamylcysteine, which in turn interacts with glycine and the enzyme glutathione synthetase to form glutathione (126, 171, 173). Glutathione is an important component of the cellular antioxidant defence (35). From the cell culture data on cysteine consumption, as well as the release of glutamate and pyroglutamate, it is evident that cells cultured without pyruvate tend to release metabolites relevant to glutathione synthesis and ROS detoxification in the medium to a higher degree compared to cells cultured in high levels of pyruvate (1mM). Retaining crucial metabolites for the glutathione synthesis instead of releasing them, coupled with the increase of cystine consumption, indicates that the cells cultured with pyruvate most likely have an increased ROS detoxification. Since glutamine can be used in the neo-synthesis of glutamate and pyroglutamate via glutaminase 2 (126), higher synthesis rates of those two amino acids could explain their increased release. A problem with this theory is the lack of difference in the glutamine consumption between cells with and without pyruvate.

Another possibility would be that the observed metabolic release, especially of pyroglutamate, is the cell culture equivalent of “septic shock” where the drastic increase of ROS results in glutathione depletion and insufficient neo-synthesis (174). However, glutamate release was not decreased in response to increasing pyroglutamate as observed by Gamarra et al (174). There are two possible explanations for this. The increased levels of glutamate release after irradiation observed in the current work could point to an increased function of the cystine/glutamate antiporter xCT (125). This could be the case in cell culture and skin explants cultured in high pyruvate levels (1mM) but not in cells cultured without pyruvate, since cystine consumption decreases despite their higher glutamate release. Another possibility is the function of glutamate in an autocrine signalling loop. It has been shown that there is an increase in glutamate release when the skin barrier function is disrupted (175). In addition to that, a 2007 study by Namkoong et al. suggests that glutamate signalling is crucial for melanoma proliferation (176). UVA is known to disrupt the barrier function of the stratum corneum to some extent (177) which makes glutamate release in order to restore barrier properties highly possible, especially in the context of *ex vivo* cultured skin. As shown by Namkoong (176) et al,

glutamate could also function as an enhancer of tumor cell proliferation. Although a decrease in proliferation was observed in all cell culture experiments in the current work, it is possible that the release of glutamate in the medium prevents the cells from complete proliferation arrest in the presence of stressors such as UVA.

In skin explants cultured in low-pyruvate conditions (200μM), glutamate was not UVA dependent. This might be an indication of reduced activity of the cystine/glutamate antiporter (125), which, however, is contradicted by the increase in cystine consumption. Another possibility is that the lack of difference between irradiated and un-irradiated samples indicates a reduced role of glutamate in autocrine signaling. On the other hand, glutamine consumption shows similar increase to the one observed in cell culture (unlike the lack of UVA-dependent consumption in high pyruvate skin samples), especially in skin samples cultured with 1 g/L glucose. Medium glutamine is one of the major sources of glutamate (126, 171) indicating possible glutamate neo-synthesis that can potentially mask UVA dependent changes in the glutamate release even with active cystine/glutamate antiporter.

As for the role of pyroglutamate in glutamate metabolism, compared to the *in vitro* experiments, the mouse skin explants consumed pyroglutamate from the medium instead of releasing it, and the consumption increased after UVA-irradiation. Pyroglutamate is a degradation product of the glutamine additive in the medium (178), therefore its availability in the fresh medium (without skin) is not unexpected. The consumed pyroglutamate might be used for the re-synthesis of glutamate via 5-oxoprolinase (173) and subsequent glutathione generation.

4.3.2. Metabolites in the glutamate synthesis – histidine and proline

Histidine is another important player in the glutamate synthesis together with glutamine (126, 171). In cell culture experiments, histidine consumption from the medium by human fibroblasts cultured in 1mM pyruvate increased with irradiation. However, there was no stable consumption pattern in the absence of pyruvate. It is likely that the role of glutamate source is taken by glutamine in this case. Histidine consumption decreased with irradiation in both low- and high-pyruvate skin samples. In the low pyruvate samples this decrease also correlated with decrease in asparagine release, indicating possibly reduced activity of asparagine-amino acid exchange factor (179). The decrease in histidine consumption after skin sample irradiation suggests

that alternative sources for glutamate are used – glutamine in low-pyruvate samples and arginine with ornithine and L-glutamate-5-semialdehyde as intermediary products (126, 171) for the samples cultured in 1mM pyruvate. Another possible source of glutamate, urocatate (126), also gets retained in the skin after irradiation.

It is also possible that the skin explants prefer an alternative strategy to increased precursor consumption in order to replenish their glutamate reserves – retention of metabolites used for the synthesis process. The decrease in proline release with irradiation supports this theory (126).

Proline can be used in glutamate synthesis, either with L-glutamate-5-semialdehyde or 1-pyrroline-5-carboxylate as intermediary products (126, 171). A retention of the metabolite was observed to a greater extend in skin samples after irradiation in both high and low pyruvate conditions which is indicative of possible glutamate re-synthesis and subsequent glutathione generation. Compared to that, cultured cells in medium without pyruvate had increased proline secretion after irradiation. There have been reports of proline acting as a free radical scavenger (180, 181). However, there is direct evidence of proline being able to reduce UVA-related cellular damage (182) and, at least in plant models, it is able to stabilize redox enzymes such as catalase (183) and superoxide dismutase (184) providing further oxidative stress protection. Under such conditions, it is possible that proline release is an indication of insufficient ROS detoxification, similar to pyroglutamate (174).

4.3.3. Metabolites in the cystine synthesis – choline, betaine, and sarcosine

The metabolites choline, betaine, and sarcosine are involved in the synthesis of cystine and therefore can also influence the glutathione pathway (126). From the three, only sarcosine was detected in both cell culture and skin supernatants. Sarcosine is a frequently used biomarker for increased tumor metastasis in prostate cancer (185). Its function is modulating gene expression of cell-cycle-relevant proteins, promoting proliferation (186). Given its importance, it was unexpected that mouse skin cultured in high pyruvate conditions (1mM) would be increasingly releasing sarcosine in the medium after irradiation. It is possible that under high pyruvate conditions in the skin, sarcosine plays a role in preventing cell cycle arrest in irradiated cells and tissue via autocrine signaling (186).

Coupled with increased sarcosine consumption in skin under low-pyruvate conditions, the metabolites glycine and betaine show reduced secretion after irradiation. Considering their role in cysteine synthesis and subsequent glutathione metabolism, the retention of these compounds in the skin is likely an indication of active ROS-detoxification (126, 171, 173).

4.3.4. Citrate cycle metabolites

Only cells cultured in 1mM pyruvate show UVA-dependant differences in isoleucine, valine, and lysine – essential amino acids important for the citrate cycle (126). Increased consumption of isoleucine after irradiation could also be detected after irradiation in low-pyruvate skin supernatants. This could be an indication of increased respiration (75).

On the other hand asparagine, which can be used for fumarate synthesis and thus is also involved in the citrate cycle, is released after irradiation by the cells cultured without pyruvate (126, 171). This could be an indication of some problems with the cellular respiration.

4.3.5. Threonine and tryptophan

Threonine and tryptophan were detected only in skin samples but not in cell culture. Threonine was released in the supernatant and UVA-irradiation reduced its secretion in high-pyruvate samples. Some published data indicates threonine as a cell cycle regulator and proliferation enhancer in mouse embryonic stem cells (187). It is possible that threonine acts as an autocrine signal for the cells. Another interpretation would be that, if the cells expel threonine, which is a regulator of mTORC1 (187), this might have an inhibitory function on proliferation, giving the cells time to repair UVA-induced DNA damages. However, in the context of tumor and tumor stroma, the release of threonine from the surrounding tissue might benefit cancer progression and dissemination via mTORC1 activation (188).

To validate or negate any of these hypotheses, a thorough gene expression analysis of proliferation-related genes (especially related to the PI3K/Akt and mTOR pathways or CDKs), coupled with Western Blot analysis should be performed. A comparison between extra and intracellular levels of threonine should also be made.

As for tryptophan, it behaved differently between high- and low-pyruvate conditions. Skin cultured in 1mM pyruvate consumed tryptophan and the consumption decreased with irradiation. Since tryptophan is a precursor in the glutamate synthesis (126), its decreased uptake might signify problems with glutathione metabolism (189). On the other hand, skin samples cultured in low-pyruvate conditions release tryptophan in the medium, and UVA-irradiation enhances the secretion. It has been suggested that tryptophan on its own can act as a radical scavenger (190), therefore its release in the medium under these experimental conditions might fulfill similar role. Contrary to that, there is data showing that tryptophan can be primed by UV irradiation to generate superoxide anion (191). In that case, releasing tryptophan might be a way for the skin to minimize the amount of potential ROS inducer under low-pyruvate medium conditions.

4.4. Influences of UVA and pyruvate on oxidative stress and DNA-damage in human fibroblasts

As evident from the experiments described thus far, the repeated irradiation of human fibroblasts with UVA results in metabolic changes indicative of ROS-detoxification. Besides them, the release and uptake of pyruvate was also influenced by irradiation. These findings are interesting because up until now there has been, as far as published literature is concerned, no other study presenting the connection between UVA and pyruvate, and their effects on glucose metabolism. Known works have studied either only pyruvate as antioxidants against chemically induced ROS or against UVB (85, 89, 90, 192, 193), but not with UVA as their main focus. It should also be noted that most of the studies, with the exception of the one by O'Donnell-Tormey (85), use much higher pyruvate concentrations than the ones in this work (2.5 to 25 times higher) (89, 90, 192, 193).

Indeed, the presence of high amounts of pyruvate in the cell culture medium led to a reduction of ROS levels after UVA treatment (Fig. 41) confirming its role as an antioxidant (85, 87, 89, 91).

However, the antioxidant effects of pyruvate were not that strong when considering its role in DNA-damage prevention. The data presented in this work show an increase of 8-OHdG, a guanosine modification used as a reliable marker for oxidative damage (123, 194), after 2 days of irradiation compared to untreated

samples. The absence of pyruvate in the medium even significantly increased the endogenous damage level in samples without UVA treatment (Fig. 42). However, despite showing a tendency of increased 8-OHdG after irradiation, the absence of pyruvate from the medium did not significantly influence the DNA-damage after irradiation. What is more, prolonged irradiation (4 days treatment) resulted in further equilibration of 8-OHdG levels between cells with and without pyruvate and even abolished the difference between irradiated and un-irradiated samples. The fact that the values for the most aggressive treatment (-pyr UVA-irradiated) in the 2d and 4d experiments were virtually the same indicates damage saturation. It seems that pyruvate alone, at least not in the used concentrations of 1mM, is insufficient to prevent DNA damage in a long-term UVA exposure, although the data presented in this work and other publications (85, 87, 89, 91) show that it can effectively quench ROS. As shown in Fig. 41, 1mM pyruvate addition to the medium does not bring ROS to base untreated levels. These remaining reactive species could lead to DNA-damage accumulation that can no longer be influenced by the presence of pyruvate. This phenomenon, however, could be a good *in vitro* confirmation of the observation that 8-OHdG is higher in aged tissues that have received more oxidative damage (194). This conclusion comes from the observation that the “older” 4d samples had a higher amount of damage, compared to their “younger” 2d counterparts.

From these data, one could conclude that pyruvate has limited antioxidant capacity during long-term treatments. It is possible that pyruvate is a readily-available first-line defense for the cells, giving them enough time to kick-start other, more potent antioxidant mechanisms like the glutathione system. Still, to be able to confirm this theory the levels of 8-OHdG should also be measured after 1d of UVA treatment and also the levels of intra and extracellular pyruvate, as well as glutathione, should be determined. To further elaborate on the protective function of pyruvate, higher concentrations should also be tested.

4.5. Pyruvate regulation of MMP1 and MMP3, and UVA-dependant MMP15 regulation in human fibroblasts

From all the findings in this work, it is evident that UVA irradiation effects the metabolic profile of human cells and in particular fibroblasts. The presence of pyruvate during the irradiation process modulates this response and is even able to ameliorate damaging effects on DNA to some extent. Therefore, it was of interest to see what

effects pyruvate would have on another important process dysregulated by UVA – the expression of MMPs. What this work was able to show is that presence of pyruvate during irradiation has the effect of decreasing the expression of key MMPs such as MMP1 and MMP3. This is a completely new finding since no publications on the topic could be found and of great importance since these two metalloproteinases play important roles in skin tumor progression and photoaging (15).

From all tested MMPs (see. Fig. 43 to Fig. 45), pyruvate regulated the expression of MMP1 and MMP3. The fact that UVA increases MMP expression has been already shown (53, 129, 132, 195, 196). The findings for MMP1 and MMP3 correlate closely to the ones shown by Jeon and associates (195). The increase of MMP2 and MMP15 expression after irradiation was similar to the one observed by Kamenisch et al. (53). However, both MMP2 and MMP15 showed only a tendency of pyruvate dependence and its influence on gene regulation was not significant. Still, the fact that MMP15 shows an UVA-dependant expression in fibroblasts is a crucial new finding, since up to now, UV-dependant modulation was observed only in corneal keratinocytes (15, 197).

MMP9 and MMP13 were not influenced by UVA contrary to the findings in the aforementioned publication (53). Kamenisch and associates used malignant melanoma cells compared to the non-malignant fibroblasts used in this study (53), suggesting that changes in the UVA-dependence of MMP9 and MMP13 expression could be due to the general differences between cancer cells and healthy skin cells. Nevertheless, it is interesting to see that non-malignant fibroblasts exhibit somewhat similar tendencies to malignant cells. In the context of the tumor microenvironment, this supports the role of non-malignant cells as additional modulators of tumor progression and metastasis (198).

The fact that UVA increases the transcriptional activity of MMPs is also an important factor in skin photoaging (15). Keeping that in mind, the finding that the presence of pyruvate modulates the response of fibroblasts to UVA-irradiation by reducing MMP expression is important in regard to pyruvate's potential implementation as topical antioxidant (90). However, it must be noted that pyruvate has the ability to negatively regulate melanin production (199). Further studies *ex vivo* and *in vivo* are needed to validate pyruvate's potential and safety as an antioxidant in skin care applications directed against wrinkle formation and photoaging.

Another finding was that UVA irradiation significantly increased TIMP1 expression, with samples cultured without pyruvate tending to have even higher, albeit not significant, expression compared to cells irradiated in the presence of pyruvate (Fig. 46). There have been controversial publications on the topic with TIMP1 being up- or down-regulated, or even showing no UVA-induced modulations depending on the cell type observed (53, 132, 197). As an inhibitor of metalloproteinase activity, it was expected for TIMP1 to be down-regulated in the presence of UVA since several MMPs were significantly increased after irradiation. This discrepancy between the expected and observed mRNA levels could be due to several reasons.

Since the observed cells (Re5) are healthy primary fibroblasts, it is natural for them to react to the increased MMP-expression by counteracting it in an attempt to preserve the “tissue homeostasis”, despite the cells being cultured *in vitro* (200). Therefore, when fibroblasts up-regulate MMP gene transcription due to UVA irradiation, metalloproteinase antagonists should also be highly transcribed.

Another possibility for the simultaneous increase of MMPs and TIMP1 is that the measurements were performed at an “overlapping” time point. There is a temporal regulation of the gene expression with TIMP1 being down-regulated during and directly after irradiation to allow an increase of MMP-mRNA (201). Since the collection of the mRNA samples was performed 12 hours after UVA irradiation, it is possible that the TIMP1 transcription was on the rise compared to declining MMPs, and the acquired time point showed a transitional state of gene expression. Therefore, a time-resolved mRNA analysis should be performed on irradiated and un-irradiated cells in the presence/absence of pyruvate to validate this theory. Furthermore, increased mRNA levels do not automatically equal increased protein production or even MMP activation. As a step further in analysing the combined regulatory function of UVA and pyruvate on the MMPs and TIMP1 a Western Blot analysis coupled with a zymography should be performed.

5. Conclusions and outlook

This work shed light on the metabolic behaviour of different non-malignant cells and a complex skin system after the application of repetitive, sub-erythemal doses of UVA-radiation. It also discussed the influence of pyruvate on said metabolic profile and on the stress-reaction of human fibroblasts and skin after irradiation. It showed that in cell culture UVA increases glucose and lactate metabolism independent of cell type or donor species. Furthermore, it showed that cells irradiated in the absence of pyruvate show indications of less efficient glutathione synthesis and unstable consumption of citrate cycle relevant metabolites. The work also showed that the capacity of pyruvate as a potential antioxidant for ROS-detoxification in fibroblasts. This thesis also highlighted the role of pyruvate, in combination with UVA, as a modulator of MMP expression, especially in the case of MMP1 and MMP3, and also reported for the first time UVA-dependant modulation of MMP15. All these findings are depicted in Fig. 48.

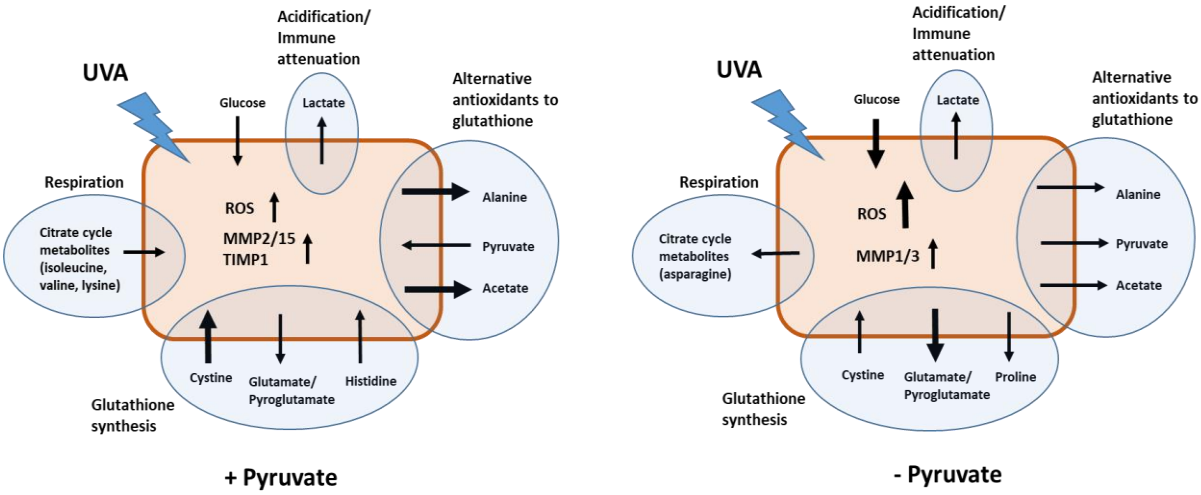

Fig. 48.: Graphic representation of the metabolic and functional changes in human fibroblasts after UVA and pyruvate treatment. Thicker arrows indicate process enhancement compared to corresponding pyruvate treatment (comparison UVA+pyruvate and UVA-pyruvate).

Still, further tests are needed in order to better understand the interplay between pyruvate and UVA in the context of the skin. These additional tests can be divided in three major groups – *in vitro, ex vivo,* and *in vivo.*

Supplementary *in vitro* experiments would cover the detection of intracellular metabolites in the presence of UVA and pyruvate and comparing them to the metabolite data acquired from the fibroblast supernatant described in the current work. This would be the next logical step in order to clarify the complex metabolic

modulations occurring after UVA and pyruvate treatment. Another interesting angle to look at the effects that UVA and pyruvate exert on the cells would be to perform PCR and Western Blot analysis on transporter proteins, receptors for para- and autocrine signals and proteins, involved in respiration and cell cycle. These experiments should be performed first on fibroblasts in order to match with the data obtained from this work. In a second step, keratinocytes should also be tested in order to compare their reaction to irradiation and pyruvate treatment. Both cell types, fibroblasts and keratinocytes, would provide differential metabolic data for the upper skin layers (keratinocytes) and the deeper layers of the dermis (fibroblasts).

Another optimization point could be the source and type of UV-radiation applied. Considering that natural sunlight consist of both UVA and UVB, it would be beneficial for both future *in vitro* and *in vivo* studies to be performed with a solar simulator providing the full sunlight spectrum rather than focusing on a single type of UVR. Thus, more natural and biologically relevant experimental conditions could be achieved, in order to gather data as close as possible to real-life sun exposure.

To better mimic the real-life sun exposure, the *in vitro* experiments could be repeated *ex vivo* on skin explants from human donors or on skin reconstructs, which would increase the clinical relevance of the studies, as well as the data transferability from the experimental setting to a macroscopic system such as intact human skin.

A crucial point in any further study would be to collect *in vivo* data about the skin metabolic flux during irradiation in real time after UVR-treatment. Since skin reddening (erythema) can be observed after prolonged sun exposure, it is likely to expect higher than normal levels of pyruvate and other antioxidant metabolites on the treatment site due to an increased blood flow. This theory needs to be tested in order to determine the exact pyruvate concentration that should be implemented in future cell culture or *ex vivo* experiments. It will also provide better understanding of the metabolic changes in the human skin during sun exposure, which is a crucial step for developing new treatments and protection strategies. Another important point to be tested *in vivo* would be what influences pyruvate has on the immune-response during UVR-treatment. As previously mentioned, lactate attenuates the immune response and can induce the expression of MMPs. The current work has shown that pyruvate can reduce the expression levels of some MMPs. Therefore, elaborating on pyruvate's effects

concerning immune response is crucial for its potential clinical and cosmetic applications.

6. Literature

1. Lee SH, Jeong SK, Ahn SK. An update of the defensive barrier function of skin. Yonsei Med J. 2006;47(3):293-306.

2. Wickert RR, Visscher MO. Structure and function of the epidermal barrier. Am J Infect Control. 2006;34(10):S98-S110.

3. Monteiro-Riviere NA. Toxicology of the Skin. A. Wallace Hayes JAT, and Donald E. Gardner, editor: Informa Healthcare USA, Inc.; 2010. 425 p.

4. Yousef H, Alhajj M, Sharma S. Anatomy, Skin (Integument), Epidermis. StatPearls. Treasure Island (FL)2019.

5. Wong DJ, Chang HY. Skin tissue engineering. StemBook. Cambridge (MA)2008.

6. Gould J. Superpowered skin. Nature. 2018;563(7732):S84-S5.

7. Baroni A, Buommino E, De Gregorio V, Ruocco E, Ruocco V, Wolf R. Structure and function of the epidermis related to barrier properties. Clin Dermatol. 2012;30(3):257-62.

8. Braun-Falco O, Plewig G, Wolff HH, Winkelmann RK. Dermatology: Springer Berlin Heidelberg; 2013.

9. Quevedo WC, JR. Epidermal Melanin Units Melanocyte-Keratinocyte Interactions. American Zoologist. 2015;12(1):35-41.

10. Cichorek M, Wachulska M, Stasiewicz A, Tyminska A. Skin melanocytes: biology and development. Postepy Dermatol Alergol. 2013;30(1):30-41.

11. Kaidbey KH, Agin PP, Sayre RM, Kligman AM. Photoprotection by melanin--a comparison of black and Caucasian skin. J Am Acad Dermatol. 1979;1(3):249-60.

12. Jayadev R, Sherwood DR. Basement membranes. Current Biology. 2017;27(6):R207-R11.

13. Williams IR. Fibroblasts. In: Delves PJ, editor. Encyclopedia of Immunology (Second Edition). Oxford: Elsevier; 1998. p. 905-9.

14. Frantz C, Stewart KM, Weaver VM. The extracellular matrix at a glance. Journal of Cell Science. 2010;123(24):4195-200.

15. Pittayapruek P, Meephansan J, Prapapan O, Komine M, Ohtsuki M. Role of Matrix Metalloproteinases in Photoaging and Photocarcinogenesis. Int J Mol Sci. 2016;17(6).

16. Ushiki T. Collagen Fibers, Reticular Fibers and Elastic Fibers. A Comprehensive Understanding from a Morphological Viewpoint. Archives of Histology and Cytology. 2002;65(2):109-26.

17. Thomson J, Singh M, Eckersley A, Cain SA, Sherratt MJ, Baldock C. Fibrillin microfibrils and elastic fibre proteins: Functional interactions and extracellular regulation of growth factors. Seminars in Cell & Developmental Biology. 2019;89:109-17.

18. Rigel DS, Weiss RA, Lim HW, Dover JS. Photoaging: CRC Press; 2004.

19. Hamill KJ, Hopkinson SB, Hoover P, Todorović V, Green KJ, Jones JCR. Fibronectin expression determines skin cell motile behavior. J Invest Dermatol. 2012;132(2):448-57.

20. Wong R, Geyer S, Weninger W, Guimberteau J-C, Wong JK. The dynamic anatomy and patterning of skin. Exp Dermatol. 2016;25(2):92-8.

21. Marov MY, Kuznetsov VD. Solar Flares and Impact on Earth. In: Allahdadi F, Pelton JN, editors. Handbook of Cosmic Hazards and Planetary Defense. Cham: Springer International Publishing; 2021. p. 1-26.

22. Modenese A, Korpinen L, Gobba F. Solar Radiation Exposure and Outdoor Work: An Underestimated Occupational Risk. Int J Environ Res Public Health. 2018;15(10):2063.

23. Armstrong B, Baverstock K, Brenner D, Cardis E, Green A, Guilmette R, et al. IARC Monographs on the Evaluation of Carcinogenic Risks to Humans. Volume 100. A Review of Human Carcinogens. Part D: Radiation2012.

24. Tanaka A, Makino A. Photosynthetic research in plant science. Plant Cell Physiol. 2009;50(4):681-3.

25. Holick M, MacLaughlin J, Clark M, Holick S, Potts J, Anderson R, et al. Photosynthesis of previtamin D3 in human skin and the physiologic consequences. Science. 1980;210(4466):203-5.

26. Ruban AV. Evolution under the sun: optimizing light harvesting in photosynthesis. Journal of Experimental Botany. 2014;66(1):7-23.

27. Meinhardt M, Krebs R, Anders A, Heinrich U, Tronnier H. Wavelength-dependent penetration depths of ultraviolet radiation in human skin. J Biomed Opt. 2008;13(4):044030.

28. Parisi AV, Wong JCF. Erythemal irradiances of filtered ultraviolet radiation. Physics in Medicine and Biology. 1997;42(7):1263-75.

29. Kimlin MG, Parisi AV. Ultraviolet radiation penetrating vehicle glass: a field based comparative study. Physics in Medicine and Biology. 1999;44(4):917-26.

30. Rochette PJ, Therrien JP, Drouin R, Perdiz D, Bastien N, Drobetsky EA, et al. UVA-induced cyclobutane pyrimidine dimers form predominantly at thymine-thymine dipyrimidines and correlate with the mutation spectrum in rodent cells. Nucleic Acids Res. 2003;31(11):2786-94.

31. Schuch AP, Moreno NC, Schuch NJ, Menck CFM, Garcia CCM. Sunlight damage to cellular DNA: Focus on oxidatively generated lesions. Free Radical Biology and Medicine. 2017;107:110-24.

32. Jiang Y, Rabbi M, Kim M, Ke C, Lee W, Clark RL, et al. UVA Generates Pyrimidine Dimers in DNA Directly. Biophysical Journal. 2009;96(3):1151-8.

33. Jaszewska E, Soin M, Filipek A, Naruszewicz M. UVA-induced ROS generation inhibition by Oenothera paradoxa defatted seeds extract and subsequent cell death in human dermal fibroblasts. Journal of Photochemistry and Photobiology B: Biology. 2013;126:42-6.

34. Ichihashi M, Ueda M, Budiyanto A, Bito T, Oka M, Fukunaga M, et al. UV-induced skin damage. Toxicology. 2003;189(1):21-39.

35. Kerksick C, Willoughby D. The antioxidant role of glutathione and N-acetyl-cysteine supplements and exercise-induced oxidative stress. J Int Soc Sports Nutr. 2005;2(2):38-44.

36. Greinert R, Volkmer B, Henning S, Breitbart EW, Greulich KO, Cardoso MC, et al. UVA-induced DNA double-strand breaks result from the repair of clustered oxidative DNA damages. Nucleic Acids Res. 2012;40(20):10263-73.

37. Costa V, Quintanilha A, Moradas-Ferreira P. Protein oxidation, repair mechanisms and proteolysis in Saccharomyces cerevisiae. IUBMB Life. 2007;59(4-5):293-8.

38. Morliere P, Moysan A, Santus R, Huppe G, Maziere JC, Dubertret L. UVA-induced lipid peroxidation in cultured human fibroblasts. Biochim Biophys Acta. 1991;1084(3):261-8.

39. Tyrrell RM. Ultraviolet radiation and free radical damage to skin. Biochem Soc Symp. 1995;61:47-53.

40. Gaschler MM, Stockwell BR. Lipid peroxidation in cell death. Biochem Biophys Res Commun. 2017;482(3):419-25.

41. Knott A, Denckhan A, Reuschlein K, Lucius R, Döring O, Böttger M, et al. Decreased fibroblast contractile activity and reduced fibronectin expression are involved in skin photoaging. Journal of Dermatological Science. 2010;58(1):75-7.

42. Heng JK, Aw DCW, Tan KB. Solar elastosis in its papular form: uncommon, mistakable. Case Rep Dermatol. 2014;6(1):124-8.

43. Kligman AM. Early Destructive Effect of Sunlight on Human Skin. JAMA. 1969;210(13):2377-80.

44. Bernerd F, Asselineau D. UVA exposure of human skin reconstructed in vitro induces apoptosis of dermal fibroblasts: subsequent connective tissue repair and implications in photoaging. Cell Death & Differentiation. 1998;5(9):792-802.

45. Boyer B, Fourtanier A, Kern P, Labat-Robert J. UVA- and UVB-induced changes in collagen and fibronectin biosynthesis in the skin of hairless mice. Journal of Photochemistry and Photobiology B: Biology. 1992;14(3):247-59.

46. Agar NS, Halliday GM, Barnetson RS, Ananthaswamy HN, Wheeler M, Jones AM. The basal layer in human squamous tumors harbors more UVA than UVB fingerprint mutations: a role for UVA in human skin carcinogenesis. Proc Natl Acad Sci U S A. 2004;101(14):4954-9.

47. Drobetsky EA, Turcotte J, Châteauneuf A. A role for ultraviolet A in solar mutagenesis. Proceedings of the National Academy of Sciences. 1995;92(6):2350-4.

48. Noonan FP, Zaidi MR, Wolnicka-Glubisz A, Anver MR, Bahn J, Wielgus A, et al. Melanoma induction by ultraviolet A but not ultraviolet B radiation requires melanin pigment. Nat Commun. 2012;3:884.

49. Pudroma X, Duoji G, Grigalavicius M, Jie D, Juzeniene A. Molecular Mechanisms of UVA-Induced Melanoma. 2017;36(3):217-28.

50. Elwood JM, Gallagher RP. Body site distribution of cutaneous malignant melanoma in relationship to patterns of sun exposure. International Journal of Cancer. 1998;78(3):276-80.

51. Thomas NE, Berwick M, Cordeiro-Stone M. Could BRAF mutations in melanocytic lesions arise from DNA damage induced by ultraviolet radiation? J Invest Dermatol. 2006;126(8):1693-6.

52. Beani JC. [Ultraviolet A-induced DNA damage: role in skin cancer]. Bulletin de l'Academie nationale de medecine. 2014;198(2):273-95.

53. Kamenisch Y, Baban TS, Schuller W, von Thaler AK, Sinnberg T, Metzler G, et al. UVA-Irradiation Induces Melanoma Invasion via the Enhanced Warburg Effect. J Invest Dermatol. 2016;136(9):1866-75.

54. Kleiner DE, Stetler-Stevenson WG. Matrix metalloproteinases and metastasis. Cancer Chemotherapy and Pharmacology. 1999;43(1):S42-S51.

55. Kamenisch Y, Ivanova I, Drexler K, Berneburg M. UVA, metabolism and melanoma: UVA makes melanoma hungry for metastasis. Exp Dermatol. 2018;27(9):941-9.

56. Fisher MS, Kripke ML. Systemic alteration induced in mice by ultraviolet light irradiation and its relationship to ultraviolet carcinogenesis. 1977. Bull World Health Organ. 2002;80(11):908-12.

57. Norval M. The mechanisms and consequences of ultraviolet-induced immunosuppression. Progress in Biophysics and Molecular Biology. 2006;92(1):108-18.

58. Iwai I, Hatao M, Naganuma M, Kumano Y, Ichihashi M. UVA-Induced Immune Suppression Through an Oxidative Pathway. Journal of Investigative Dermatology. 1999;112(1):19-24.

59. Smith HL, Howland MC, Szmodis AW, Li Q, Daemen LL, Parikh AN, et al. Early stages of oxidative stress-induced membrane permeabilization: a neutron reflectometry study. Journal of the American Chemical Society. 2009;131(10):3631-8.

60. Gruss C, Reed JA, Altmeyer P, McNutt NS, Kerscher M. Induction of interstitial collagenase (MMP-1) by UVA-1 phototherapy in morphea fibroblasts. Lancet (London, England). 1997;350(9087):1295-6.

61. Gilchrest BA, Park HY, Eller MS, Yaar M. Mechanisms of ultraviolet light-induced pigmentation. Photochem Photobiol. 1996;63(1):1-10.

62. Wicks NL, Chan JW, Najera JA, Ciriello JM, Oancea E. UVA phototransduction drives early melanin synthesis in human melanocytes. Current biology : CB. 2011;21(22):1906-11.

63. Pathak MA, Riley FJ, Fitzpatrick TB, Curwen WL. Melanin formation in human skin induced by long-wave ultra-violet and visible light. Nature. 1962;193:148-50.

64. Routaboul C, Denis A, Vinche A. Immediate pigment darkening: description, kinetic and biological function. European journal of dermatology : EJD. 1999;9(2):95-9.

65. Dalmau N, Andrieu-Abadie N, Tauler R, Bedia C. Phenotypic and lipidomic characterization of primary human epidermal keratinocytes exposed to simulated solar UV radiation. J Dermatol Sci. 2018;92(1):97-105.

66. Noy N. Between death and survival: retinoic acid in regulation of apoptosis. Annual review of nutrition. 2010;30:201-17.

67. Werten PJL, Röll B, van Aalten DMF, de Jong WW. Gecko ι-crystallin: How cellular retinol-binding protein became an eye lens ultraviolet filter. Proceedings of the National Academy of Sciences. 2000;97(7):3282-7.

68. Törmä H, Vahlquist A. Vitamin A esterification in human epidermis: a relation to keratinocyte differentiation. J Invest Dermatol. 1990;94(1):132-8.

69. Tafrova JI, Pinkas-Sarafova A, Stolarzewicz E, Parker KA, Simon M. UVA/B exposure promotes the biosynthesis of dehydroretinol in cultured human keratinocytes. Molecular and Cellular Biochemistry. 2012;364(1):351-61.

70. Goswami UC, Sharma N. Efficiency of a few retinoids and carotenoids in vivo in controlling benzo[a]pyrene-induced forestomach tumour in female Swiss mice. The British journal of nutrition. 2005;94(4):540-3.

71. Gęgotek A, Rybałtowska-Kawałko P, Skrzydlewska E. Rutin as a Mediator of Lipid Metabolism and Cellular Signaling Pathways Interactions in Fibroblasts Altered by UVA and UVB Radiation. Oxidative Medicine and Cellular Longevity. 2017;2017:4721352.

72. Warburg O, Wind F, Negelein E. The Metabolism of Tumors in the Body. J Gen Physiol. 1927;8(6):519-30.

73. Naifeh J, Varacallo M. Biochemistry, Aerobic Glycolysis. StatPearls. Treasure Island (FL)2020.

74. Cooper GM. The Cell: A Molecular Approach: ASM Press; 2000.

75. Berg JM, Stryer L, Tymoczko JL. Biochemistry. 5th edition: W. H. Freeman 2002; 2002.

76. Liberti MV, Locasale JW. The Warburg Effect: How Does it Benefit Cancer Cells? Trends Biochem Sci. 2016;41(3):211-8.

77. Hirschhaeuser F, Sattler UGA, Mueller-Klieser W. Lactate: A Metabolic Key Player in Cancer. Cancer Res. 2011;71(22):6921.

78. Brand A, Singer K, Koehl GE, Kolitzus M, Schoenhammer G, Thiel A, et al. LDHA-Associated Lactic Acid Production Blunts Tumor Immunosurveillance by T and NK Cells. Cell metabolism. 2016.

79. Renner K, Singer K, Koehl GE, Geissler EK, Peter K, Siska PJ, et al. Metabolic Hallmarks of Tumor and Immune Cells in the Tumor Microenvironment. Front Immunol. 2017;8:248-.

80. Marionnet C, Pierrard C, Golebiewski C, Bernerd F. Diversity of Biological Effects Induced by Longwave UVA Rays (UVA1) in Reconstructed Skin. PLOS ONE. 2014;9(8):e105263.

81. Ghezzi P. Role of glutathione in immunity and inflammation in the lung. Int J Gen Med. 2011;4:105-13.

82. Groussard C, Morel I, Chevanne M, Monnier M, Cillard J, Delamarche A. Free radical scavenging and antioxidant effects of lactate ion: an in vitro study. Journal of Applied Physiology. 2000;89(1):169-75.

83. Sallam KI. Antimicrobial and antioxidant effects of sodium acetate, sodium lactate, and sodium citrate in refrigerated sliced salmon. Food Control. 2007;18(5):566-75.

84. European Union EC. Food Additives 2020 [Available from: https://webgate.ec.europa.eu/foods_system/main/?event=substances.search&substances.pagination=1.

85. O'Donnell-Tormey J, Nathan C, Lanks K, DeBoer C, Harpe J. Secretion of pyruvate An antioxidant defense of mammalian cell. The Journal of experimental medicine. 1987;165:500-14.

86. Mallet RT, Squires JE, Bhatia S, Sun J. Pyruvate Restores Contractile Function and Antioxidant Defenses of Hydrogen Peroxide-Challenged Myocardium. Journal of Molecular and Cellular Cardiology. 2002;34(9):1173-84.

87. Constantopoulos G, Barranger JA. Nonenzymatic decarboxylation of pyruvate. Analytical Biochemistry. 1984;139(2):353-8.

88. Lemire J, Auger C, Mailloux R, Appanna VD. Mitochondrial lactate metabolism is involved in antioxidative defense in human astrocytoma cells. Journal of Neuroscience Research. 2014;92(4):464-75.

89. Ramos-Ibeas P, Barandalla M, Colleoni S, Lazzari G. Pyruvate antioxidant roles in human fibroblasts and embryonic stem cells. Molecular and Cellular Biochemistry. 2017;429(1):137-50.

90. Gupta SK, Awor L, Rastogi S, Prakash J, Gupta YK, Varma SD, et al. Delayed manifestation of ultra violet radiation induced erythema in guinea pigs by sodium pyruvate--a free radical scavenger. Indian journal of physiology and pharmacology. 1998;42(2):315-8.

91. Bassenge E, Sommer O, Schwemmer M, Bünger R. Antioxidant pyruvate inhibits cardiac formation of reactive oxygen species through changes in redox state. American journal of physiology Heart and circulatory physiology. 2000;279(5):H2431-8.

92. Tauffenberger A, Fiumelli H, Almustafa S, Magistretti PJ. Lactate and pyruvate promote oxidative stress resistance through hormetic ROS signaling. Cell Death & Disease. 2019;10(9):653.

93. Baumann F, Leukel P, Doerfelt A, Beier CP, Dettmer K, Oefner PJ, et al. Lactate promotes glioma migration by TGF-beta2-dependent regulation of matrix metalloproteinase-2. Neuro Oncol. 2009;11(4):368-80.

94. Nareika A, He L, Game BA, Slate EH, Sanders JJ, London SD, et al. Sodium lactate increases LPS-stimulated MMP and cytokine expression in U937 histiocytes by enhancing AP-1 and NF-kappaB transcriptional activities. American journal of physiology Endocrinology and metabolism. 2005;289(4):E534-42.

95. Emwas A-H, Roy R, McKay RT, Tenori L, Saccenti E, Gowda GAN, et al. NMR Spectroscopy for Metabolomics Research. Metabolites. 2019;9(7):123.

96. Gerothanassis IP, Troganis A, Exarchou V, Barbarossou K. NUCLEAR MAGNETIC RESONANCE (NMR) SPECTROSCOPY: BASIC PRINCIPLES AND PHENOMENA, AND THEIR APPLICATIONS TO CHEMISTRY, BIOLOGY AND MEDICINE. Chemistry Education Research and Practice. 2002;3(2):229-52.

97. Yadav LDS. Organic Spectroscopy: Anamaya Publishers; 2005.

98. Canet D. Radiofrequency Field Gradients in NMR, Theory. In: Lindon JC, editor. Encyclopedia of Spectroscopy and Spectrometry. Oxford: Elsevier; 1999. p. 1937-44.

99. Ross A, Schlotterbeck G, Dieterle F, Senn H. Chapter 3 - NMR Spectroscopy Techniques for Application to Metabonomics. In: Lindon JC, Nicholson JK, Holmes E, editors. The Handbook of Metabonomics and Metabolomics. Amsterdam: Elsevier Science B.V.; 2007. p. 55-112.

100. Cavanagh J, John Cavanagh WJFAGPIIINJS, Fairbrother WJ, Academic, Palmer AG, Skelton NJ. Protein NMR Spectroscopy: Principles and Practice: Elsevier Science; 1996.

101. van den Boogaart A, Ala-Korpela M, Jokisaari J, Griffiths JR. Time and frequency domain analysis of NMR data compared: An application to 1D 1H spectra of lipoproteins. Magnetic Resonance in Medicine. 1994;31(4):347-58.

102. Trindade IB, Louro RO. Chapter 5 - Introduction to biomolecular nuclear magnetic resonance and metals. In: Crichton RR, Louro RO, editors. Practical Approaches to Biological Inorganic Chemistry (Second Edition): Elsevier; 2020. p. 155-99.

103. Van QN, Issaq HJ, Jiang Q, Li Q, Muschik GM, Waybright TJ, et al. Comparison of 1D and 2D NMR Spectroscopy for Metabolic Profiling. Journal of Proteome Research. 2008;7(2):630-9.

104. Helena UZ, Jochen H, Matthias SK, Claudia S, Peter JO, Wolfram G. Current Experimental, Bioinformatic and Statistical Methods used in NMR Based Metabolomics. Current Metabolomics. 2013;1(3):253-68.

105. Giraudeau P. Challenges and perspectives in quantitative NMR. Magnetic Resonance in Chemistry. 2017;55(1):61-9.

106. Szakács Z, Sánta Z. Chapter 7 - NMR Methodological Overview. In: Szántay C, editor. Anthropic Awareness. Boston: Elsevier; 2015. p. 257-89.

107. Knoch J. Untersuchungen in vivo und in vitro zu oxidativem Stress und Mutationen der mitochondrialen DNA im Alterungsprozess: Universitätsbibliothek Tübingen; 2013.

108. Feister U, Jäkel E, Gericke K. Parameterization of daily solar global ultraviolet irradiation. Photochem Photobiol. 2002;76(3):281-93.

109. Welti M, Ramelyte E, Dummer R, Imhof L. Evaluation of the minimal erythema dose for UVB and UVA in context of skin phototype and nature of photodermatosis. Photodermatology, Photoimmunology & Photomedicine. 2020;36(3):200-7.

110. McKenzie RC, Sauder DN. Keratinocyte Cytokines and Growth Factors: Functions in Skin Immunity and Homeostasis. Dermatologic Clinics. 1990;8(4):649-61.

111. Jung JG, Le A. Targeting Metabolic Cross Talk between Cancer Cells and Cancer-Associated Fibroblasts. In: Le A, editor. The Heterogeneity of Cancer Metabolism. Cham: Springer International Publishing; 2018. p. 167-78.

112. Crowson AN, Magro CM, Sanchez-Carpintero I, Mihm MC, editors. The Precursors of Malignant Melanoma. Cancers of the Skin; 2002 2002//; Berlin, Heidelberg: Springer Berlin Heidelberg.

113. Elder DE. Precursors to melanoma and their mimics: nevi of special sites. Modern Pathology. 2006;19(2):S4-S20.

114. Hanahan D, Weinberg Robert A. Hallmarks of Cancer: The Next Generation. Cell. 2011;144(5):646-74.

115. Yamaba H, Haba M, Kunita M, Sakaida T, Tanaka H, Yashiro Y, et al. Morphological change of skin fibroblasts induced by UV Irradiation is involved in photoaging. Exp Dermatol. 2016;25(S3):45-51.

116. Xie J, Wu H, Dai C, Pan Q, Ding Z, Hu D, et al. Beyond Warburg effect – dual metabolic nature of cancer cells. Scientific Reports. 2014;4(1):4927.

117. Giovannini S. Inhibition of histone acetylation by the antimycotic drug Voriconazole impairs DNA damage repair and increases skin cancer risk 2015.

118. Doar JWH, Wynn V, Cramp DG. Blood pyruvate and plasma glucose levels during oral and intravenous glucose tolerance tests in obese and non-obese women. Metabolism. 1968;17(8):690-701.

119. Luo X, Li R, Yan L-J. Roles of Pyruvate, NADH, and Mitochondrial Complex I in Redox Balance and Imbalance in β Cell Function and Dysfunction. Journal of diabetes research. 2015;2015:512618-.

120. Soto M, Orliaguet L, Reyzer ML, Manier ML, Caprioli RM, Kahn CR. Pyruvate induces torpor in obese mice. Proceedings of the National Academy of Sciences. 2018;115(4):810-5.

121. Wu C, Okar DA, Newgard CB, Lange AJ. Overexpression of 6-phosphofructo-2-kinase/fructose-2, 6-bisphosphatase in mouse liver lowers blood glucose by suppressing hepatic glucose production. J Clin Invest. 2001;107(1):91-8.

122. Fiedler H. Reaktive Sauerstoffspecies. In: Gressner AM, Arndt T, editors. Lexikon der Medizinischen Laboratoriumsdiagnostik. Berlin, Heidelberg: Springer Berlin Heidelberg; 2018. p. 1-3.

123. Valavanidis A, Vlachogianni T, Fiotakis C. 8-hydroxy-2' -deoxyguanosine (8-OHdG): A critical biomarker of oxidative stress and carcinogenesis. Journal of environmental science and health Part C, Environmental carcinogenesis & ecotoxicology reviews. 2009;27(2):120-39.

124. Takeuchi T, Nakajima M, Ohta Y, Mure K, Takeshita T, Morimoto K. Evaluation of 8-hydroxydeoxyguanosine, a typical oxidative DNA damage, in human leukocytes. Carcinogenesis. 1994;15(8):1519-23.

125. Lewerenz J, Hewett SJ, Huang Y, Lambros M, Gout PW, Kalivas PW, et al. The cystine/glutamate antiporter system x(c)(-) in health and disease: from molecular mechanisms to novel therapeutic opportunities. Antioxid Redox Signal. 2013;18(5):522-55.

126. Laboratories K. KEGG: Kyoto Encyclopedia of Genes and Genomes 1995-2020 [Available from: https://www.genome.jp/kegg/.

127. Grosser N, Oberle S, Berndt G, Erdmann K, Hemmerle A, Schröder H. Antioxidant action of L-alanine: heme oxygenase-1 and ferritin as possible mediators. Biochem Biophys Res Commun. 2004;314(2):351-5.

128. Krogstad AL, Jansson PA, Gisslén P, Lönnroth P. Microdialysis methodology for the measurement of dermal interstitial fluid in humans. Br J Dermatol. 1996;134(6):1005-12.

129. Buechner N, Schroeder P, Jakob S, Kunze K, Maresch T, Calles C, et al. Changes of MMP-1 and collagen type Ialpha1 by UVA, UVB and IRA are differentially regulated by Trx-1. Exp Gerontol. 2008;43(7):633-7.

130. Quan T, Qin Z, Xia W, Shao Y, Voorhees JJ, Fisher GJ. Matrix-Degrading Metalloproteinases in Photoaging. Journal of Investigative Dermatology Symposium Proceedings. 2009;14(1):20-4.

131. Scharffetter K, Wlaschek M, Hogg A, Bolsen K, Schothorst A, Goerz G, et al. UVA irradiation induces collagenase in human dermal fibroblasts in vitro and in vivo. Archives of Dermatological Research. 1991;283(8):506-11.

132. Hantke B, Lahmann C, Venzke K, Fischer T, Kocourek A, Windsor LJ, et al. Influence of flavonoids and vitamins on the MMP- and TIMP-expression of human dermal fibroblasts after UVA irradiation. Photochemical & photobiological sciences : Official journal of the European Photochemistry Association and the European Society for Photobiology. 2002;1(10):826-33.

133. Giblin FJ, Leverenz VR, Padgaonkar VA, Unakar NJ, Dang L, Lin LR, et al. UVA light in vivo reaches the nucleus of the guinea pig lens and produces deleterious, oxidative effects. Experimental eye research. 2002;75(4):445-58.

134. Paluch E, Heisenberg CP. Biology and physics of cell shape changes in development. Current biology : CB. 2009;19(17):R790-9.

135. Peyton SR, Ghajar CM, Khatiwala CB, Putnam AJ. The emergence of ECM mechanics and cytoskeletal tension as important regulators of cell function. Cell biochemistry and biophysics. 2007;47(2):300-20.

136. Xu Q, Huff LP, Fujii M, Griendling KK. Redox regulation of the actin cytoskeleton and its role in the vascular system. Free Radic Biol Med. 2017;109:84-107.

137. Girard PM, Francesconi S, Pozzebon M, Graindorge D, Rochette P, Drouin R, et al. UVA-induced damage to DNA and proteins: directversusindirect photochemical processes. Journal of Physics: Conference Series. 2011;261:012002.

138. Prasad S, Mandal I, Singh S, Paul A, Mandal B, Venkatramani R, et al. Near UV-Visible electronic absorption originating from charged amino acids in a monomeric protein. Chem Sci. 2017;8(8):5416-33.

139. Bleicher P, Sciortino A, Bausch AR. The dynamics of actin network turnover is self-organized by a growth-depletion feedback. Scientific Reports. 2020;10(1):6215.

140. Lukas J, Lukas C, Bartek J. Mammalian cell cycle checkpoints: signalling pathways and their organization in space and time. DNA Repair. 2004;3(8):997-1007.

141. Lemons JMS, Feng X-J, Bennett BD, Legesse-Miller A, Johnson EL, Raitman I, et al. Quiescent Fibroblasts Exhibit High Metabolic Activity. PLOS Biology. 2010;8(10):e1000514.

142. Vander Heiden MG, Cantley LC, Thompson CB. Understanding the Warburg effect: the metabolic requirements of cell proliferation. Science. 2009;324(5930):1029-33.

143. Rawlings AV, Davies A, Carlomusto M, Pillai S, Zhang K, Kosturko R, et al. Effect of lactic acid isomers on keratinocyte ceramide synthesis, stratum corneum lipid levels and stratum corneum barrier function. Archives of Dermatological Research. 1996;288(7):383-90.

144. Thueson DO, Chan EK, Oechsli LM, Hahn GS. The roles of pH and concentration in lactic acid-induced stimulation of epidermal turnover. Dermatologic surgery : official publication for American Society for Dermatologic Surgery [et al]. 1998;24(6):641-5.

145. Proksch E. pH in nature, humans and skin. The Journal of Dermatology. 2018;45(9):1044-52.

146. Goetze K, Walenta S, Ksiazkiewicz M, Kunz-Schughart LA, Mueller-Klieser W. Lactate enhances motility of tumor cells and inhibits monocyte migration and cytokine release. Int J Oncol. 2011;39(2):453-63.

147. de la Cruz-López KG, Castro-Muñoz LJ, Reyes-Hernández DO, García-Carrancá A, Manzo-Merino J. Lactate in the Regulation of Tumor Microenvironment and Therapeutic Approaches. Front Oncol. 2019;9:1143-.

148. Fischer K, Hoffmann P, Voelkl S, Meidenbauer N, Ammer J, Edinger M, et al. Inhibitory effect of tumor cell-derived lactic acid on human T cells. Blood. 2007;109(9):3812-9.

149. Kalluri R, Zeisberg M. Fibroblasts in cancer. Nature reviews Cancer. 2006;6(5):392-401.

150. Werb Z, Lu P. The Role of Stroma in Tumor Development. Cancer J. 2015;21(4):250-3.

151. Leibiger C, Kosyakova N, Mkrtchyan H, Glei M, Trifonov V, Liehr T. First molecular cytogenetic high resolution characterization of the NIH 3T3 cell line by murine multicolor banding. J Histochem Cytochem. 2013;61(4):306-12.

152. Shipman WD, Chyou S, Ramanathan A, Izmirly PM, Sharma S, Pannellini T, et al. A protective Langerhans cell-keratinocyte axis that is dysfunctional in photosensitivity. Science translational medicine. 2018;10(454).

153. Noonan FP, Kripke ML, Pedersen GM, Greene MI. Suppression of contact hypersensitivity in mice by ultraviolet irradiation is associated with defective antigen presentation. Immunology. 1981;43(3):527-33.

154. Morison WL, Bucana C, Kripke ML. Systemic suppression of contact hypersensitivity by UVB radiation is unrelated to the UVB-induced alterations in the morphology and number of Langerhans cells. Immunology. 1984;52(2):299-306.

155. Brand K. Aerobic glycolysis by proliferating cells: protection against oxidative stress at the expense of energy yield. J Bioenerg Biomembr. 1997;29(4):355-64.

156. Iversen NK, Malte H, Baatrup E, Wang T. The normal acid–base status of mice. Respiratory Physiology & Neurobiology. 2012;180(2):252-7.

157. Burgess EA, Sylven B. Glucose, lactate, and lactic dehydrogenase activity in normal interstitial fluid and that of solid mouse tumors. Cancer research. 1962;22:581-8.

158. Sullivan MR, Danai LV, Lewis CA, Chan SH, Gui DY, Kunchok T, et al. Quantification of microenvironmental metabolites in murine cancers reveals determinants of tumor nutrient availability. eLife. 2019;8.

159. Petersen LJ. Interstitial lactate levels in human skin at rest and during an oral glucose load: a microdialysis study. Clinical physiology (Oxford, England). 1999;19(3):246-50.

160. Wallmeier J, Samol C, Ellmann L, Zacharias HU, Vogl FC, Garcia M, et al. Quantification of Metabolites by NMR Spectroscopy in the Presence of Protein. Journal of Proteome Research. 2017;16(4):1784-96.

161. Jupin M, Michiels PJ, Girard FC, Spraul M, Wijmenga SS. NMR identification of endogenous metabolites interacting with fatted and non-fatted human serum albumin in blood plasma: Fatty acids

influence the HSA-metabolite interaction. Journal of magnetic resonance (San Diego, Calif : 1997). 2013;228:81-94.

162. Martínez-Reyes I, Chandel NS. Mitochondrial TCA cycle metabolites control physiology and disease. Nature Communications. 2020;11(1):102.

163. Zhang YM, Liu JK, Wong TY. The DNA excision repair system of the highly radioresistant bacterium Deinococcus radiodurans is facilitated by the pentose phosphate pathway. Mol Microbiol. 2003;48(5):1317-23.

164. Milanese C, Mastroberardino PG. A perspective on DNA damage-induced potentiation of the pentose phosphate shunt and reductive stress in chemoresistance. Mol Cell Oncol. 2020;7(3):1733383-.

165. Mills R, Harris KR. The effect of isotopic substitution on diffusion in liquids. Chemical Society Reviews. 1976;5(0):215-31.

166. Huckabee WE. Control of Concentration Gradients of Pyruvate and Lactate Across Cell Membranes in Blood. Journal of Applied Physiology. 1956;9(2):163-70.

167. Berry CW, Hill IN, Wolf ST, Stanhewicz AE, Kenney WL. Skin Erythema and Blood Flow Responses to Acute Ultraviolet Radiation Exposure. The FASEB Journal. 2019;33(1_supplement):541.1-.1.

168. Iredahl F, Högstedt A, Henricson J, Sjöberg F, Tesselaar E, Farnebo S. Skin glucose metabolism and microvascular blood flow during local insulin delivery and after an oral glucose load. Microcirculation (New York, NY : 1994). 2016;23(7):597-605.

169. Felmlee MA, Jones RS, Rodriguez-Cruz V, Follman KE, Morris ME. Monocarboxylate Transporters (SLC16): Function, Regulation, and Role in Health and Disease. Pharmacological Reviews. 2020;72(2):466-85.

170. Zierler K. Whole body glucose metabolism. American Journal of Physiology-Endocrinology and Metabolism. 1999;276(3):E409-E26.

171. Canadian Institutes of Health Research CFfI, and by The Metabolomics Innovation Centre (TMIC). The Human Metabolome Database 4.0 2018 [Available from: https://hmdb.ca/.

172. Comerford Sarah A, Huang Z, Du X, Wang Y, Cai L, Witkiewicz Agnes K, et al. Acetate Dependence of Tumors. Cell. 2014;159(7):1591-602.

173. Palmer BF, Alpern RJ. CHAPTER 12 - Metabolic Acidosis. In: Floege J, Johnson RJ, Feehally J, editors. Comprehensive Clinical Nephrology (Fourth Edition). Philadelphia: Mosby; 2010. p. 155-66.

174. Gamarra Y, Santiago FC, Molina-López J, Castaño J, Herrera-Quintana L, Domínguez Á, et al. Pyroglutamic acidosis by glutathione regeneration blockage in critical patients with septic shock. Critical Care. 2019;23(1):162.

175. Fuziwara S, Inoue K, Denda M. NMDA-type glutamate receptor is associated with cutaneous barrier homeostasis. J Invest Dermatol. 2003;120(6):1023-9.

176. Namkoong J, Shin SS, Lee HJ, Marín YE, Wall BA, Goydos JS, et al. Metabotropic glutamate receptor 1 and glutamate signaling in human melanoma. Cancer research. 2007;67(5):2298-305.

177. Biniek K, Levi K, Dauskardt RH. Solar UV radiation reduces the barrier function of human skin. P Natl Acad Sci USA. 2012;109(42):17111-6.

178. Tritsch GL, Moore GE. Spontaneous decomposition of glutamine in cell culture media. Experimental cell research. 1962;28:360-4.

179. Krall AS, Xu S, Graeber TG, Braas D, Christofk HR. Asparagine promotes cancer cell proliferation through use as an amino acid exchange factor. Nat Commun. 2016;7:11457.

180. Liang X, Zhang L, Natarajan SK, Becker DF. Proline mechanisms of stress survival. Antioxid Redox Signal. 2013;19(9):998-1011.

181. Kaul S, Sharma SS, Mehta IK. Free radical scavenging potential of L-proline: evidence from in vitro assays. Amino acids. 2008;34(2):315-20.

182. Wondrak GT, Jacobson MK, Jacobson EL. Identification of quenchers of photoexcited States as novel agents for skin photoprotection. The Journal of pharmacology and experimental therapeutics. 2005;312(2):482-91.

183. Chen C, Dickman MB. Proline suppresses apoptosis in the fungal pathogen Colletotrichum trifolii. Proc Natl Acad Sci U S A. 2005;102(9):3459-64.

184. Islam MM, Hoque MA, Okuma E, Banu MN, Shimoishi Y, Nakamura Y, et al. Exogenous proline and glycinebetaine increase antioxidant enzyme activities and confer tolerance to cadmium stress in cultured tobacco cells. Journal of plant physiology. 2009;166(15):1587-97.

185. Cernei N, Heger Z, Gumulec J, Zitka O, Masarik M, Babula P, et al. Sarcosine as a potential prostate cancer biomarker--a review. Int J Mol Sci. 2013;14(7):13893-908.

186. Heger Z, Merlos Rodrigo MA, Michalek P, Polanska H, Masarik M, Vit V, et al. Sarcosine Up-Regulates Expression of Genes Involved in Cell Cycle Progression of Metastatic Models of Prostate Cancer. PloS one. 2016;11(11):e0165830-e.

187. Ryu JM, Han HJ. L-threonine regulates G1/S phase transition of mouse embryonic stem cells via PI3K/Akt, MAPKs, and mTORC pathways. The Journal of biological chemistry. 2011;286(27):23667-78.

188. Kim LC, Cook RS, Chen J. mTORC1 and mTORC2 in cancer and the tumor microenvironment. Oncogene. 2017;36(16):2191-201.

189. Singh S, Khan AR, Gupta AK. Role of glutathione in cancer pathophysiology and therapeutic interventions. Journal of experimental therapeutics & oncology. 2012;9(4):303-16.

190. Nayak BN, Buttar HS. Evaluation of the antioxidant properties of tryptophan and its metabolites in in vitro assay. Journal of complementary & integrative medicine. 2016;13(2):129-36.

191. Igarashi N, Onoue S, Tsuda Y. Photoreactivity of Amino Acids: Tryptophan-induced Photochemical Events via Reactive Oxygen Species Generation. Analytical Sciences. 2007;23(8):943-8.

192. Aoki R, Aoki-Yoshida A, Suzuki C, Takayama Y. Protective Effect of Indole-3-Pyruvate against Ultraviolet B-Induced Damage to Cultured HaCaT Keratinocytes and the Skin of Hairless Mice. PLOS ONE. 2014;9(5):e96804.

193. de Groot MJM, van Helden MAB, de Jong YF, Coumans WA, van der Vusse GJ. The influence of lactate, pyruvate and glucose as exogenous substrates on free radical defense mechanisms in isolated rat hearts during ischaemia and reperfusion. Molecular and Cellular Biochemistry. 1995;146(2):147-55.

194. Kaneko T, Tahara S, Matsuo M. Non-linear accumulation of 8-hydroxy-2'-deoxyguanosine, a marker of oxidized DNA damage, during aging. Mutation Research/DNAging. 1996;316(5):277-85.

195. Jeon S, Choi M. Anti-inflammatory and anti-aging effects of hydroxytyrosol on human dermal fibroblasts (HDFs). Biomedical Dermatology. 2018;2.

196. Petersen MJ, Hansen C, Craig S. Ultraviolet A irradiation stimulates collagenase production in cultured human fibroblasts. J Invest Dermatol. 1992;99(4):440-4.

197. P. Gendron S, Rochette P. Modifications in stromal extracellular matrix of aged corneas can be induced by ultraviolet A irradiation. Aging Cell. 2015;14.

198. Hofmann UB, Eggert AA, Blass K, Bröcker EB, Becker JC. Stromal cells as the major source for matrix metalloproteinase-2 in cutaneous melanoma. Arch Dermatol Res. 2005;297(4):154-60.

199. Zhou S, Sakamoto K. Pyruvic acid/ethyl pyruvate inhibits melanogenesis in B16F10 melanoma cells through PI3K/AKT, GSK3β, and ROS-ERK signaling pathways. Genes to cells : devoted to molecular & cellular mechanisms. 2019;24(1):60-9.

200. Brew K, Dinakarpandian D, Nagase H. Tissue inhibitors of metalloproteinases: evolution, structure and function. Biochim Biophys Acta. 2000;1477(1-2):267-83.

201. Overall CM, Wrana JL, Sodek J. Transcriptional and post-transcriptional regulation of 72-kDa gelatinase/type IV collagenase by transforming growth factor-beta 1 in human fibroblasts. Comparisons with collagenase and tissue inhibitor of matrix metalloproteinase gene expression. J Biol Chem. 1991;266(21):14064-71.

7. List of Figures

8. List of Tables

9. Acknowledgements

First and foremost, I want to thank my PhD-supervisor Prof. Marina Kreutz, as well as my mentors Prof. Mark Berneburg and Prof. Wolfram Gronwald, and my lab-supervisor Dr. York Kamenisch. Thank you for your guidance, support, and invaluable lessons. Without you, this work would not have been possible.

I also want to thank all my colleagues from the Dermatology-lab: Prof. Tim Maisch, Dr. Stephanie Arndt, Petra Unger, Judith Heider, Barbara Schwertner, Susanne Wallner, and Dr. Bernadett Kurz. Thank you for the warm and welcoming environment, for all the support and teachings… and for having the patience to listen to my complaints about failed experiments and dead cells over and over again. Many thanks to Dr. Stephanie Arndt for providing the 129 SV/EV mice used in this work.

Special thanks to the AG Gronwald and especially Claudia Bogner for showing me how to prepare and evaluate NMR-samples.

Last but not least, I want to thank my friends and family for their unwavering emotional support through thick and thin.

10. Declaration

I hereby certify that I have written this work myself and have not used any sources or aids other than those indicated.

Regensburg, 17.11.2021

_____

(Irina Ivanova)